Silicon Nanocrystals: High-Temperature Reactions of Silicon and Silicon Oxides

by

Kevin M. O'Connor

A thesis submitted in partial fulfillment of the requirements for the degree of

Doctor of Philosophy

Department of Chemistry

University of Alberta

Abstract

Hydrogen silsesquioxane (HSQ) is a versatile material with a lengthy history in the synthesis of silicon nanocrystals (SiNCs). Although SiNCs are an exciting material for many optical, electronic, and biological applications, the focal point of this thesis challenges many of the preconceived notions regarding SiNC synthesis from HSQ disproportionation. The reliability of HSQ as a precursor material for silicon nanoparticles is examined and our understanding of its behavior under previously unexplored reaction conditions is expanded.

Chapter 1 introduces materials at the nanoscale with a particular focus on silicon nanocrystals. Promising applications featuring SiNCs are highlighted and the major synthesis routes to SiNCs are discussed. The introduction closes with a section on the history of HSQ and its use as a precursor material for SiNC preparation.

Chapter 2 pushes the boundaries of silicon nanoparticle (SiNP) synthesis by subjecting HSQ to previously unexplored high-temperature environments. In the course of investigating the HSQ disproportionation reaction under various temperatures and dwell times, a perplexing set of observations for a specific range of reaction conditions was discovered, resulting in the complete absence of elemental silicon. Although it has previously been assumed that the resulting Si–SiO_2 interface is unreactive, sufficiently high temperatures can promote the reduction of SiO_2 by Si to produce SiO gas. Under appropriate conditions, this somewhat unexpected reaction can complicate solid state nanomaterial syntheses by etching away the desired products. In both mixed Si/SiO_2 powders and HSQ, the crystallization of silica into cristobalite facilitated the transport of silicon atoms through silicon monoxide formation. Elevating the reaction temperature to 1700°C

effectively mitigated this undesired reaction in HSQ by softening the surrounding silica and inhibiting matrix crystallization.

Chapter 3 presents the synthesis of SiNCs in ambient air from hydrogen silsesquioxane. SiNCs were produced in lower yield in air than in inert atmosphere; SiNCs prepared in argon showed no significant improvement in photoluminescence than those prepared in forming gas (5% H_2 in Ar). The reducing atmosphere did impact particle size at 1700°C, indicating an onset of increased Si particle growth in the presence of hydrogen at high temperatures.

Many insights gained from this research have implications for other group 14 nanocrystal syntheses employing solid-state disproportionation reactions. The demonstration of photoluminescent SiNCs grown in non-inert environments offers a promising synthesis route for other air-sensitive nanomaterials. Experimental work is summarized and future projects are presented in the final chapter.

Preface

All work presented in this thesis received funding from the Natural Science and Engineering Research Council of Canada (NSERC Discovery Grant program; RGPIN-2020-04045), and the ATUMS training program supported by NSERC CREATE (CREATE-463990-2015). Additional support was provided by the University of Alberta Faculties of Science and Graduate Studies.

Chapter 2 amalgamates two publications. The first is published as O'Connor, K.; Rubletz, A.; Ni, C.; He, Y.; Butler, C.; Veinot, J. G. C. High-Temperature Anomaly in the Synthesis of Large (d > 100 nm) Silicon Nanoparticles from Hydrogen Silsesquioxane. *Chemistry of Materials*, **2023**, *35,* 7967–7973. I was responsible for concept formation, data collection, data analysis, and manuscript preparation. Abbie Rubletz assisted with data collection, data analysis, and manuscript editing. Chuyi Ni performed the transmission electron microscopy. Yingjie He performed the scanning electron microscopy and energy dispersive X-ray spectroscopy. Cole Butler collected the X-ray photoelectron spectra. Dr. Jonathan Veinot was the supervisory author and assisted with concept formation, data analysis, and manuscript preparation. The second publication included in Chapter 2 is published as O'Connor. K. M.; Rubletz, A.; Trach, J.; Butler, C.; Veinot, J. G. C. Understanding silicon monoxide gas evolution from mixed silicon and silica powders. *Nanoscale Horizons*, **2023**, *8*, 892–899. I was responsible for concept formation, data collection, data analysis, and manuscript preparation. Abbie Rubletz assisted with data collection, data analysis, and manuscript editing. Jonathan Trach performed the scanning electron microscopy and energy dispersive X-ray spectroscopy. Cole Butler collected the X-ray photoelectron spectra. Dr. Jonathan Veinot was the supervisory author and assisted with concept formation, data analysis, and manuscript preparation.

Chapter 3 is original. I was responsible for concept formation, data collection, and data analysis. Riley Hooper assisted with the collection and analysis of solid-state nuclear magnetic resonance data. I Teng Cheong collected the photoluminescence measurements and assisted with data analysis. Alyssa Fu performed the scanning electron microscopy. Abbie Rubletz assisted with powder X-ray diffraction measurements. Cole Butler collected the X-ray photoelectron spectra. Jonathan Trach performed the scanning electron microscopy and energy dispersive X-ray spectroscopy.

Chapter 4 is original. It provides a summary of the work presented in Chapters 2 and 3 and outlines direction for potential future projects. Some preliminary data is included. I was responsible for data collection and analysis.

Acknowledgments

In acknowledging the support I have received throughout my degree, I express my sincere gratitude to all those who have made this thesis possible.

Thank you, Dr. Jonathan Veinot. In the face of many challenges your endless enthusiasm inspired me to be confident in myself and my research. I enjoyed the freedom you afforded me to explore new projects and I will remember my time in the Veinot Research Group fondly.

I am grateful to have participated in the Alberta/Technical University of Munich International Graduate School for Hybrid Functional Materials (ATUMS). During both of my research exchanges I was generously hosted by Prof. Dr. Bernhard Rieger. I am thankful to Prof. Rieger and his students, Dr. Elisabeth Groß, Amelie Mühlbach, Moritz Kleybolte, and Philipp Pfändner. The ATUMS program would also not be possible without the tremendous efforts of Leah Veinot and Dr. Sergei Vagin.

My research exchanges abroad also brought me to Bordeaux, France where I was kindly hosted by Dr. Glenna Drisko. I enjoyed collaborating with the Drisko research group and I owe a special thank you to Dr. Cynthia Cibaka-Ndaya and Dr. Lucian Roiban.

I want to thank my committee members and examiners, Dr. Arthur Mar, Dr. Lingzi Sang, Dr. Al Meldrum, Dr. Rik Tykwinski, and Dr. Mark McDermott. I also wish to thank Dr. Indika Arachchige for serving as an external examiner for my thesis defence.

I wish to acknowledge the support staff in the Department of Chemistry. Thank you, Dirk Kelm, Paul Crothers, Farhat Emhemed, Ryan Lewis, and Mike Barteski.

I am grateful to my past and present coworkers in the Veinot Lab, many of whom became my closest friends. Thank you, Abbie Rubletz, Dr. Sarah Milliken, Dr. Yingjie (Jay) He, Dr. Alyxandra Thiessen, Dr. I Teng (Emily) Cheong, Riley Hooper, Chuyi (Martin) Ni, Jonathan Trach, Cole Butler, Brayden Glockzin, Madison Chevalier, Cemre Mertoglu, Suni Guo, Christina Zafeiridou, Dominic Lavergne, Mia Dolanjski, and Chantell Fernandes. A special thank you to Dr. John Washington for reviewing this thesis.

Upon moving to Edmonton, the support and comradery of my newfound friends was invaluable. Thank you, Samuel Baird, Aaron Kirkey, Dr. Jasper Woodard, Dr. Alvaro Omaña Moreno, Dr. Chrissy Braun, Dr. Ian Watson, Dr. Matthew Roy, Brandon Frenette, Nicholas Kissoon, Zachary Schroeder, and Michael Doyle.

I am especially grateful to Alyssa Fu. Your kindness, generosity, and support throughout my degree kept my days bright, even during the cold Edmonton winters. I am so grateful for the incredible adventures we shared while camping, hiking, and skiing around Alberta.

Finally, I am grateful to my loving family. They are my unwavering foundation and my source of inspiration.

Table of Contents

List of Tables

List of Figures

List of Symbols, Nomenclature and Abbreviations

a.u.	Arbitrary unit
am	Amorphous
CVD	Chemical vapour deposition
°	Degree
°C	Degree Celsius
d	Diameter
e-beam	Electron-beam
EDX	Energy dispersive X-ray spectroscopy
ETEM	Environmental transmission electron microscopy
FOx-X	Flowable-oxide
FTIR	Fourier transform infrared spectroscopy
FWHM	Full width at half maximum
HPLC	High-performance liquid chromatography
h	Hour
HSQ	Hydrogen silsesquioxane
IR	Infrared
MIBK	Methyl isobutyl ketone
µm	Micrometer
µs	Microsecond
nm	Nanometer
NMR	Nuclear magnetic resonance
PL	Photoluminescence
PL_{max}	Photoluminescence emission maximum
PLQY	Photoluminescence quantum yield
POSS	Polyhedral oligomeric silsesquioxanes
QD	Quantum dot
QY	Quantum yield
s	Second
SEM	Scanning electron microscopy
SiNC	Silicon nanocrystal

SiNP	Silicon nanoparticle
$SiNC/SiO_2$	Silicon nanocrystal embedded in a silica matrix
$SiNP/SiO_2$	Silicon nanoparticles embedded in a silica matrix
SRO	Silicon-rich oxide
TOAB	Tetraoctylammonium bromide
TEM	Transmission electron microscopy
cm^{-1}	Wavenumber
wt.%	Weight percent
UV	Ultraviolet
XP	X-ray photoelectron
XPS	X-ray photoelectron spectroscopy
XRD	X-ray diffraction

Chapter 1

Introduction

1.1 Silicon and the Nanoscale

Silicon-based materials are ubiquitous in 21st century technology. With little exaggeration, it can be said that we are now living in the silicon age.[1] Semiconductor devices utilizing silicon (Si) have formed the foundation from which information era technology has emerged. From solar panels to integrated circuits, silicon-based materials are common, unseen parts of our daily lives. The search for new silicon-based materials continues; among these innovations is the field of nanotechnology and the fabrication of semiconductors at the "nanoscale".

The "nanoscale" occupies the size regime found between bulk solids and the individual atoms that compose them. At this scale, unique size-dependent characteristics emerge that are unlike those of single molecules or bulk materials. These properties arise as a result of quantum confinement which describes the phenomena associated with restricting the movement of charge carriers (i.e., electrons and holes) within a solid as the dimensions of the solid particle approach the nanoscale. In semiconductors, decreasing dimensions to the nanoscale widens the band gap by forcing excitons (excited electron-hole pairs) into a state of higher energy than what is normally observed in the bulk material.[2] This effect is size dependent, and allows the band gap to be tuned

by defining the particle size. These small particles are termed nanoparticles, and semiconductor nanoparticles that exhibit quantum confinement properties are often termed quantum dots (QDs).[2]

The first observation of quantum confinement in silicon involved a material called porous silicon. Porous silicon forms when bulk crystalline silicon wafers are subject to aqueous hydrofluoric acid (HF) etching under anodic bias.[3] This process produces pores within the crystal that preferentially propagate along the <100> plane. If the pore walls are thin enough, room temperature quantum confinement in silicon can be achieved.[4] This phenomenon manifests itself as orange photoluminescence when the porous silicon is illuminated with ultraviolet (UV) light. The high-energy UV photons promote valence band electrons in the nanoscale silicon to the conduction band. When the electrons relax from this excited state, they release visible light photons. This emission arises from a higher energy state than that which produces the infrared emission observed from bulk silicon and effectively illustrates the differences that can occur between the properties of bulk and nanoscale materials (Figure 1-1).

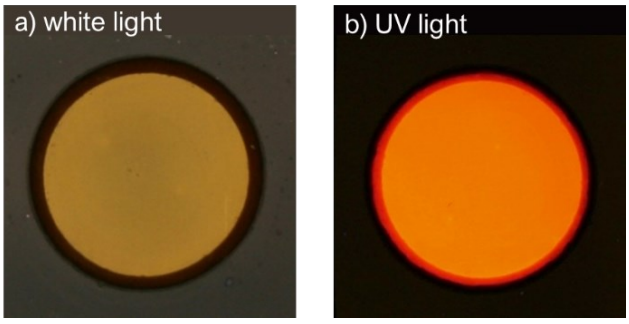

Figure 1-1. Photographs of porous silicon etched on a silicon wafer illuminated by (a) white light, and (b) UV light. The visible orange photoluminescence arises from quantum confinement in the silicon. Adapted from *Porous Silicon in Practice*, 2011 (Ref. 5).

The discovery of photoluminescent porous silicon initiated an extensive and widespread research endeavor centered on silicon nanomaterial preparation. Scientists were intrigued about

the origins of nano-silicon's bright photoluminescence and were eager to use the material for a variety of applications. Moreover, silicon is an attractive element for end use in applications and materials. By mass, silicon composes 27% of the Earth's continental crust and, following oxygen, Si atoms are the second most abundant on our planet's surface.[6] Silicon is also biologically benign. In the body, silicon oxidizes and hydrolyzes to form nontoxic silicic acids that are readily processed and excreted through the renal organs (i.e., kidneys, bladder).[7] The biocompatibility of silicon is a significant benefit because it allows the nanomaterial to be used in biological systems for cellular imaging or drug transport.[8,9] Silicon-based materials are also environmentally inert and present little or no concerns related to material life cycles. In these regards, silicon nanomaterials present a significant advantage over cadmium- or indium-based quantum dots that are toxic or rely upon non-abundant elements.[10]

The synthesis of silicon quantum dots and, more generally, silicon nanoparticles (SiNPs) of any size, has yet to receive the commercial attention afforded to the microchip industry. Only recently have some commercial applications for SiNPs become economically successful; others remain on the horizon. As such, despite substantial advances, the fabrication of high quality, freestanding silicon nanoparticles is yet to become a mature, optimized technology.

The following section highlights some of the most prominent and promising applications of SiNPs. In each case, the properties of the SiNPs vary depending upon the target application. This includes nanoparticle size, shape, crystallinity, porosity, polydispersity, surface functionality, and yield. Understanding the demands of each application is critical when considering the SiNP synthesis method. The remainder of the introduction provides an overview of the synthesis methods used to produce SiNPs and discusses how the resulting materials may meet the requirements of the applications.

1.2 Applications of Silicon Nanoparticles

The number of potential applications relevant to SiNPs exceeds those presented here. In the interest of brevity, the following examples showcase the applications that have received the greatest amount of academic and commercial attention.

1.2.1 Photoluminescence

There are a variety of ways in which SiNP photoluminescence (PL) can be utilized. Examples include biological imaging,[11] electronic displays,[12] photovoltaics,[13] and sensing.[14] Some aspects of SiNPs, such as surface functional groups, will differ between these applications, but each require quantum dots that luminesce brightly at predictable wavelengths with high quantum yield. Quantum yield (QY) is given by the equation:[15]

$$QY(\%) = \frac{no.\ photons\ emitted}{no.\ photons\ absorbed} \times 100\%$$

Quantum yield quantifies how effectively a luminophore converts absorbed energy into emitted light. To maximize SiNP photoluminescent QY several criteria must be fulfilled.

Both the size and size distribution of the nanoparticles are critical because the size-dependent nature of quantum confinement creates a relationship between particle size and photon emission. Varying the size allows for tuning of the PL of SiNPs across the visible spectrum.[16,17] As discussed above, quantum confinement is only possible when the physical size constraint of the particle pushes the exciton into a higher energy state. For silicon, this phenomenon emerges when particles possess diameters smaller than *ca*. 9 nm.[18,19] Larger SiNPs will possess the photoluminescent properties of bulk silicon with a correspondingly lower QY.[20] Similarly, SiNPs approaching very small sizes (< 3 nm) exhibit a lower QY due to an increase in nonradiative

recombinations as excitons experience a greater frequency of interactions with surface defects or capping ligands.[21] For these reasons, the size distribution of SiNPs targeting PL applications must be controlled. This limits the number of nanoparticles that are either too large or too small to efficiently emit photons and maximizes the expected photoluminescence. Additionally, SiNP samples with a wide size distribution will emit light across a broader range of frequencies which is often undesirable for photoluminescence applications.[12]

Nanoparticle crystallinity also influences SiQD QY. The disordered nature of amorphous SiNPs results in a higher likelihood of nonradiative relaxation processes, lowering the photoluminescence QY.[22] The conventional notion of crystallinity breaks down at the nanoscale where the small number of unit cells present in each nanocrystal hardly constitute 'long-range order'.[23] The structural strain of the nanoparticle surface has an increasing influence as NP size decreases and disorder is observed in crystalline SiNPs under 6 nm in diameter. This effect creates a crystallinity gradient in 6–9 nm SiNPs from the ordered particle core to its disordered surface.[23] Thiessen *et al.* explored this gradient through an analysis of SiNP photoluminescence, finding that the size of the crystalline nanoparticle core was a better predictor for QD emission than the physical size of the particle.[24]

Finally, SiNPs must possess tailorable surface chemistry. Not only is this essential for interfacing SiNPs with biological systems, but the surface ligands can also drastically alter the particle emission. Rather than radiating through a bandgap transition, the nanoparticle surface chemistry can induce charge transfer to surface states where exciton relaxation is relatively faster.[25] For example, the creation of Si–N bonds using dodecylamine yields blue-emitting surface states whereas the formation of Si–C bonds using alkenes does not interfere with the intrinsic bandgap emission and orange-red emission is observed.[26,27] Surface oxidation can also act as a defect site

by trapping excited electrons before recombination and effectively blue-shifts the PL emission.[27] These phenomena are complex but overall they allow SiNP PL to be tuned across the visible spectrum (Figure 1-2).[25, 26]

Given these many factors, it is clear that the PLQY of a colloidal SiNP sample depends strongly on the preparation method. For example, typical PLQY values for alkyl-terminated SiNPs fall in the range of 10–30%, and record-high values have reached 70%.[25] The PLQY of SiNPs terminated in hydride groups is normally below 5%.[25]

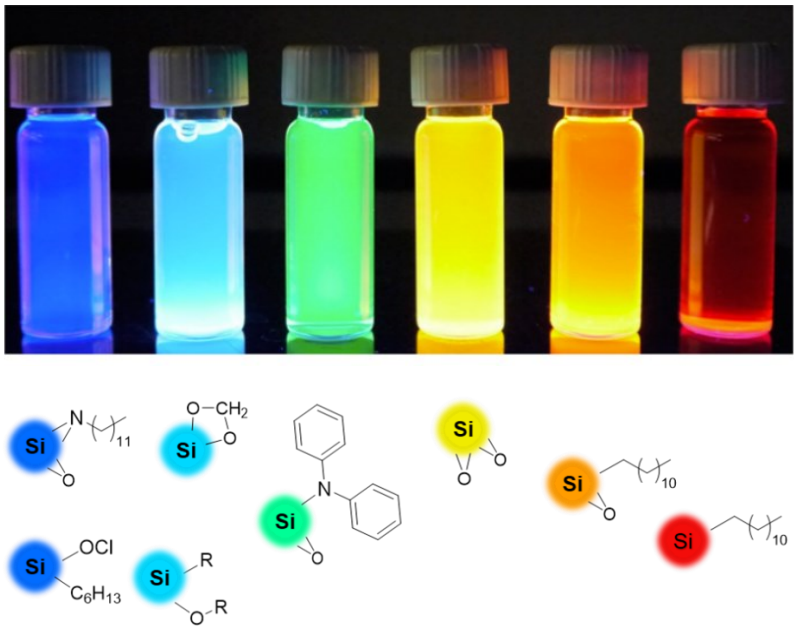

Figure 1-2. Silicon nanoparticles functionalized with various surface groups dispersed in toluene, under UV illumination. Adapted with permission from *ACS Nano* **2014**, *8*, 9636–9648 (Ref. 26).

1.2.2 Lithium-Ion Batteries

The working principle of a lithium-ion battery is the controlled exchange of Li^+ ions between two electrodes. During operation, the battery discharges as lithium ions travel via an electrolyte from the anode to the cathode. This process produces an electric potential across a closed circuit caused

by the reduction–oxidation reactions at the anode and cathode during Li^+ intercalation and deintercalation.[28]

For a given volume, the total energy stored in a Li^+ battery is a function of the energy density of its electrodes. Increasing the number of Li^+ ions stored by the electrodes provides a greater amount of power during battery discharge. For this reason, the materials used for the battery electrodes are critical and a large body of research concerning Li^+ battery anode and cathode materials is available in the literature.[29] Some of the most promising materials are based on silicon.

Currently, the anode of a conventional lithium-ion battery is constructed using graphite because it possesses high electrical conductivity while retaining structural stability and charge carrier capacity.[30] When fully lithiated (LiC_6), graphite has a modest specific capacity of 372 mA h g^{-1}. [31] The idea to implement silicon-based materials as anode materials was inspired by the greater capacity of silicon for lithium ions. The fully lithiated silicon-lithium inorganic compound ($Li_{15}Si_4$ at room temperature) has a specific capacity of 3580 mA h g^{-1}, roughly 10 times higher than graphite.[30] However, with the inclusion of so many Li atoms, the volume of the lithium silicide increases by approximately 300% compared to the parent Si.[32] The swelling, and subsequent shrinking during battery discharge, eventually results in a structural fragmentation of the silicon material and electrically isolates the anode. This problem is compounded by the inherently low electrical conductivity of silicon. For these reasons, researchers have designed hybrid systems using silicon nanoparticles to supress the undesirable complications that arise from repeated lithiation and delithiation of silicon.[29]

When compared to other applications, the material requirements for SiNPs used in battery anodes are less rigorous. For example, the crystallinity of the nanoparticles in unimportant because the lithiation process transforms crystalline domains into amorphous silicon.[33] Porosity in the

anode material is beneficial because it allows the material to accommodate the volume expansion of the compound during Li insertion; however, this can be accomplished without need for porous SiNPs.[34] Nanoparticle shape is similarly unimportant. Fundamentally, the size of the nanoparticles is the most critical consideration. If the SiNPs become too large the effects of poor electrical conductivity and large volume expansion are more pronounced and offset the beneficial properties. In 2010, Yushin and coworkers used SiNPs to create a SiNP–C composite material that possessed a specific capacity of 1,950 mA h g^{-1} (Figure 1-3).[34] In their study, the authors utilized SiNPs ranging from 10–30 nm.

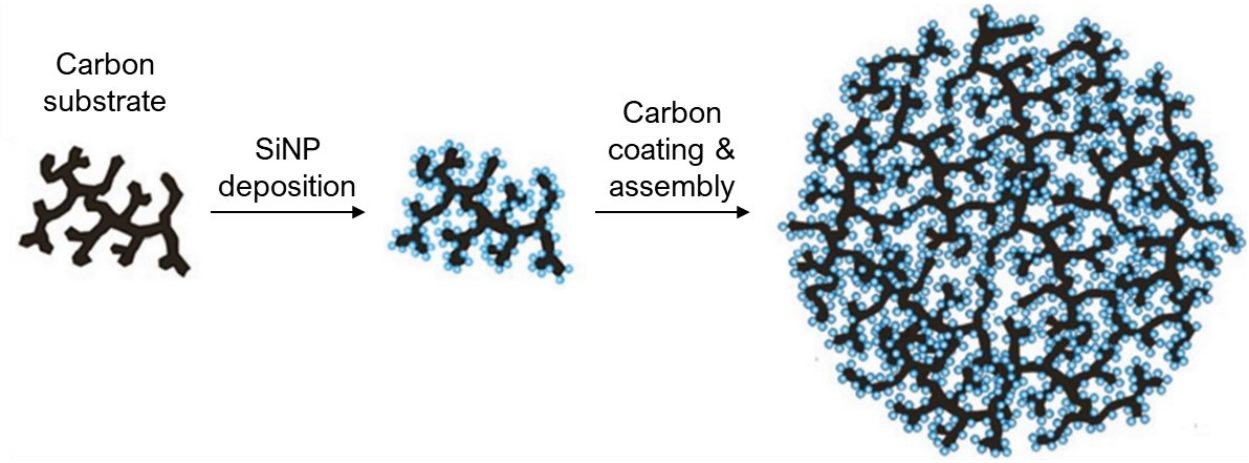

Figure 1-3. Schematic of SiNP–C composite granules used for Li-ion battery anodes. The silicon nanoparticles are depicted in blue. Adapted from *Nat. Mater.* **2010**, *9*, 353–358 (Ref. 34).

1.2.3 **Metamaterials**

Metamaterials are an emerging topic in materials research. The term 'metamaterial' denotes the technological step beyond conventional materials and describes a material that possess emergent properties through the carefully engineering of its structure.[35] Typically, these structures form arrays of repeating units or particles within a host matrix.[36, 37] When exposed to incident

electromagnetic or acoustic waves, the combined resonance of the individual particles results in unique, and often unprecedented, wavefront manipulation. Some of the most exciting phenomena made possible using metamaterials include negative refractive index, superlensing, and cloaking.[39]

In recent years, SiNPs were identified as an ideal particle for the construction of metamaterials active in the visible spectrum.[37-39] For this application, the resonating particles must have a high scattering efficiency, a higher refractive index than the host matrix, and a low absorption coefficient across the visible spectrum.[39] Silicon, with its high refractive index (n = 4–5) and near zero absorption coefficient across the visible spectrum, meets these criteria.[40] Similar to photoluminescence, scattering resonance is a function of particle size. As the size of a sphere approaches that of the incident wavelength, scattering can be described by Mie theory. For silicon particles, this theory predicts that visible light (λ = 300–800 nm) resonance can be achieved using particles ranging from 75 to 200 nm in diameter. The first Mie resonance is observed when the electromagnetic wavelength within the particle ($\lambda_p = \frac{\lambda_0}{n}$) is equal to the particle diameter (λ_0 is the vacuum wavelength). In addition, SiNPs ideal for this application should also be crystalline, spherical, monodisperse, and contain no porosity or impurities.[39]

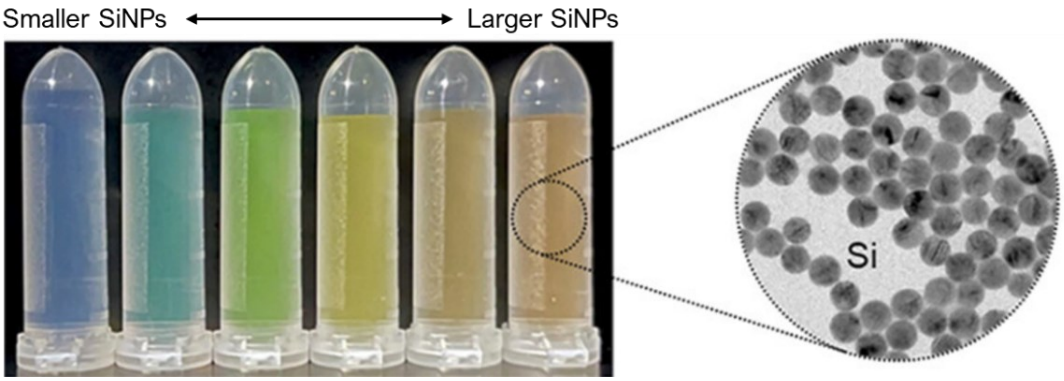

Figure 1-4. Photograph and electron microscopy image of SiNPs exhibiting wavelength-selective Mie scattering. Adapted from *Nano Lett*. **2023**, *23*, 5101–5107 (Ref. 41).

1.3 Silicon Nanoparticle Syntheses

The optical properties of SiNPs have served as the primary motivation for the development of new and robust synthesis methods. Both chemists and physicists have developed an array of approaches that are characteristic of the two fields. This variety will become evident in the following section which provides an overview of the methods used for SiNP preparation. The basic principles of each technique will be outlined along with a discussion regarding the practicality of the methods for addressing modern SiNP applications.

1.3.1 Top-down

The most straightforward of all methods is the top-down approach. This describes the breaking down of large, macro-scale silicon into small, nano-sized particles. The silicon source for these syntheses are typically crystalline lumps or wafers, and their conversion into the nanoscale is generally accomplished by electrochemical etching, laser ablation, or mechanical grinding.

Electrochemical Etching

Anodic etching of silicon wafers was initially developed for obtaining nanoporous silicon. It was adapted for SiNP preparation after it was discovered that sonication of the etched wafers would break down the films and result in a suspension of SiNPs.[42,43] This is accomplished using a single-cell system equipped with a Pt cathode and a Si anode in a solution of ethanoic or aqueous hydrofluoric acid (HF).[44] After washing and drying, the wafers are sonicated and the resulting colloidal SiNPs are collected via centrifugation.[43] Further size reduction of the SiNPs is possible by etching in a solution of nitric (HNO_3) and hydrofluoric acids, but this technique is not unique to electrochemical methods and has been combined with many other SiNP syntheses.[16,45,46]

Overall, the low yields, poor morphology control, and hazardous reagents make electrochemical etching an uncommon route for SiNP synthesis.

Laser Ablation

Laser ablation uses a high energy photon beam to evaporate material from a light-absorbing substrate. The concentrated laser light can remove material from the substrate through single-photon (bond scission) and multi-photon (thermal evaporation) excitation.[47] In addition to vaporizing the target material, this process creates a plume of plasma around the impact site. Outside the plasma, volatile species rapidly cool to form nanoparticles through physical condensation and coagulation.[47] This technique was originally developed as a low-pressure gas phase process, but newer methods now include laser ablation in liquids.[48] These SiNP preparations often utilize pulsed laser ablation of Si wafers in de-ionized water;[47-50] however, a one-pot synthesis and surface modification method has also been demonstrated using liquid alkenes.[49,50] A report from Yuan *et al.* developed this method further by performing laser ablation on macro-Si in a solution of 1-decene and hydrofluoric acid (HF, 3% vol.).[50] This produced 3 nm alkyl-terminated SiNPs with a PL quantum efficiency between 50–70%.[50]

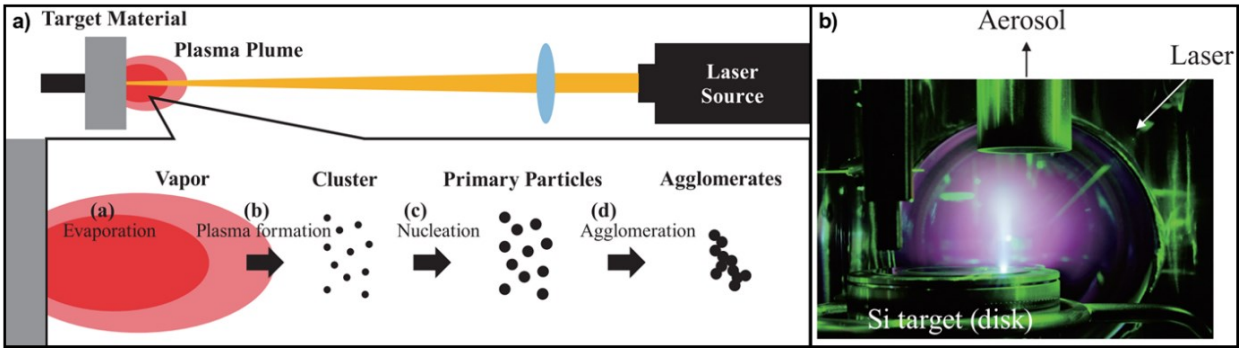

Figure 1-5. Silicon laser ablation in a low-pressure environment. (a) Schematic of the particle generation procedure in the laser ablation process. (b) Laser-induced plume of silicon. Adapted from *Kona Powder Part. J.* **2017**, 34, 80–90 (Ref. 51).

Mechanical and Mechanochemical

The synthesis of SiNPs is possible by mechanical ball milling,[52] but this method is more often combined with other reagents for mechanochemical reactions.[53-55] For example, Kuang *et al.* prepared alkyl-terminated SiNPs (~ 2 nm) by milling Si wafers with 1-hexene for 24 h at room temperature. The authors claim that fragmentation of the wafers creates reactive Si surfaces containing dangling bonds and silicon radicals which are passivated by the surrounding alkenes.[55] While straightforward, this approach results in amorphized nanoparticles with low quantum yield (PLQY ≤ 2%) along with iron impurities from the steel milling balls.[25,55]

Aiming for larger SiNPs, a unique report from Plain and coworkers used a kitchen blender to produce crystalline SiNPs with diameters spanning 100–200 nm.[56] After blending Si lumps in de-ionized water, the authors allowed the resulting colloid of exfoliated particles to settle for 4 days before carefully extracting the supernatant liquid. Further size selection was then carried out with a series of centrifugation steps. While the shape of the SiNPs was irregular, the particles were highly crystalline and successfully demonstrated electric and magnetic Mie resonances in the visible range.[56]

1.3.2 Reducing Agents

Numerous efforts have been made to produce SiNPs using reducing agents. Generally, these reactions fall under one of two categories: reduction of silicon halides or magnesiothermic reduction. Many of these methods offer room temperature routes using common wet laboratory techniques but can suffer from impurities and poor photoluminescence properties.[25]

Significant contributions to this field include works from the Tilley and Kauzlarich research groups. Tilley and coworkers explored the reduction of silicon tetrachloride ($SiCl_4$) using a selection of hydride reducing agents, including sodium borohydride ($NaBH_4$), lithium borohydride ($LiBH_4$), superhydride ($LiEt_3BH$), and lithium aluminum hydride ($LiAlH_4$).[57,58] These reactions were carried out in the presence of pentaethylene glycol monododecyl ether or tetraoctylammonium bromide (TOAB) surfactants to limit particle agglomeration and aggregation. Generally, stronger reducing agents produced smaller SiNPs with a narrower size distribution. All SiNPs were hydride-terminated, smaller than 3 nm, and displayed photoluminescence maxima around 350 nm after surface functionalization with allylamine.[58]

Avoiding the use of hazardous hydride-based reductants, Kauzlarich and coworkers accomplished similar results by reducing $SiCl_4$ using sodium naphthalide ($Na^+C_{10}H_8^-$) in glyme (dimethoxyethane). The authors could control the size of the silicon nanocrystals from 3–9 nm by modifying the reactant concentrations.[59,60] The Kauzlarich group has also used metal silicide (Zintl salt) metathesis reactions.[61] Again using glyme, this process reduces silicon halides (i.e., $SiCl_4$) through the oxidation of metal silicides (Mg_2Si). Alternatively, metal silicides (i.e., Na_4Si_4) can react with ammonium bromide (NH_4Br) in refluxing DMF. In both cases, the crystalline SiNPs are small (< 5 nm) and display blue photoluminescence after alkyl surface functionalization.[61,62] A recent report by the Drisko group synthesized SiNPs by room temperature reduction of $SiCl_4$ with Mg metal in solution of glyme, diglyme or tetraglyme, in THF. The resulting particles, while crystalline, showed and poor shape control, high polydispersity, and failed to reach particle sizes sufficient for Mie scattering.[63]

Lastly, reduction from magnesiothermic reactions offers a pathway to SiNPs using silica reagents. This solid-state reaction differs from the solution-based methods mentioned above as it

requires moderate heating. Dasog *et al.* prepared silicon nanocrystals spanning a wide size range (4–177 nm) by thermally treating Stöber silica particles with magnesium powder to 500°C.[64] A step involving HCl is required to remove the magnesium oxide formed in the reaction.

[1.1] $SiO_2 + 2\ Mg \rightarrow Si + 2\ MgO$

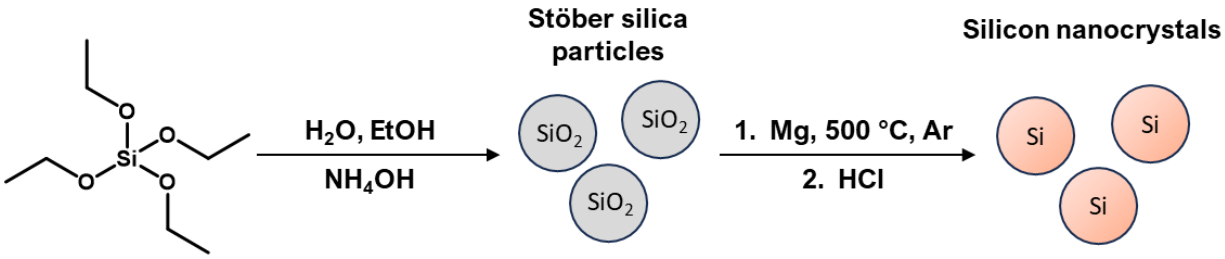

Figure 1-6. Preparation of silicon nanocrystals using the magnesiothermic reduction of silica nanoparticles.[64] Silica is reduced following reaction equation [1.1].

1.3.3 Silane Decomposition

When exposed to an appropriate energy source, silane molecules ($HSiR_3$; R = H, aromatic, alkyl) undergo decomposition, resulting in the nucleation and growth of SiNPs. This reaction is likely the earliest recorded method for making SiNPs.[65] Presented in its simplest form the overall equation is:

[1.2] $SiH_{4\,(g)} \rightarrow Si_{\,(s)} + 2H_{2\,(g)}$

Though conceptually straightforward, the variety of experimental procedures and reagents has resulted in silane decomposition becoming an extensive area of research for SiNP preparation. The most popular of these methods use gas and plasma phase reactors because they allow for a continuous "flow through" procedure.[66]

Thermally-Induced Decomposition

A typical gas-phase pyrolysis of silane is accomplished by flowing a dilute concentration of SiH_4 (< 1%) in an inert carrier gas (i.e., He, Ar, N_2, or H_2) through a heated reaction chamber.[67-69] At temperatures exceeding 370°C, the silanes dissociate into hydrogen and highly reactive silylene (SiH_2).[70] It is proposed that silylenes react with other silane molecules, starting a chain reaction that forms a series of silicon-hydride structures (Si_2H_6, Si_3H_8, *etc*.) leading to agglomeration and ultimately NP synthesis.[71] A recent study from Vazquez-Pufleau and Wang identified stable silane clusters (Si_7H_{11}) that result from silylene reactions, but the exact mechanism for aerosol nucleation remains elusive.[72]

[1.3] $SiH_4 \rightarrow SiH_2 + H_2$

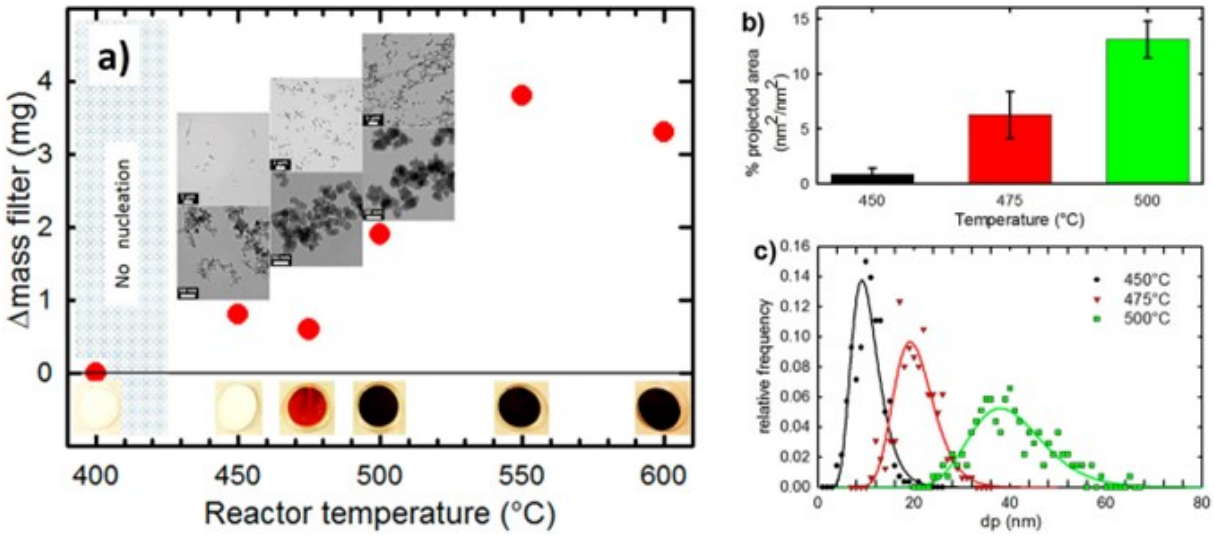

Figure 1-7. The temperature dependence of SiNP mass and size using silane pyrolysis (0.3% SiH_4 in He). (a) Mass of aerosols collected on filter over 5 minutes with inset transmission electron microscope images. (b) SiNP concentration based on percentage of TEM grid coverage by aerosols. (c) Size distribution of SiNPs prepared at 450°C (black), 475°C (red), and 500°C (green). Reprinted with permission from *J. Chem. Phys*. **2020**, *152*, 024304 (Ref. 72).

Nanoparticle formation and growth from silane pyrolysis are a function of both temperature and concentration. At a given temperature, particles will only form above the critical silane concentration. Similarly, a given concentration of silane will only form particles above the critical temperature (Figure 1-7).[72] Achieving crystallinity in SiNPs prepared this way is also possible, but it requires aerosol formation at temperatures exceeding 1100 K .[68]

Aiming to leverage the high-throughput potential of silane pyrolysis, the Swihart group designed a CO_2 laser reactor capable of producing photoluminescent silicon nanocrystals.[73] A mixture of silane, hydrogen, and sulfur hexafluoride (SF_6, a photosensitizer) was flowed through the path of a CO_2 laser (10.6 μm) thus heating the molecules and encouraging SiH_4 dissociation. This methodology afforded a SiNP production rate of 20–200 mg/h in an approximate yield of 10%; however, the particles only displayed photoluminescence after etching in a mixture of HF and nitric (HNO_3) acids.[73] The authors later improved the photoluminescence quantum yield from 0.5–1% to 10–20% by modifying their silicon nanocrystals with alkyl ligands.[73–75]

Thermal silane decomposition has also been explored using supercritical fluids. In comparison to their low-pressure counterparts, reactions in supercritical fluids benefit from solvating nanoparticle precursors in similar concentrations to solution-based routes.[39] Much of this work was developed by the Korgel group using trisilane (Si_3H_8) in a supercritical solution of n-hexane (*ca.* 450°C at 34.5 MPa).[76–79] This method produces high yields (> 90%) of amorphous SiNPs and the average particle size is tunable from 50 nm to 1.7 μm by adjusting the trisilane concentration. The research group also prepared small crystalline SiNPs (1–4 nm) from the decomposition of diphenylsilane in supercritical in mixtures of n-octanol and n-hexane (500°C at 34.5 MPa).[80] These alkoxide-terminated SiNPs demonstrated photoluminescence, but the quantum yield did not exceed 23%, and nanoparticle yields were low.[80] Earlier work from Heath combined the reducing

powder of sodium with a supercritical solution of silicon tetrachloride in n-hexane. After reacting for multiple days, a polydisperse range of crystalline SiNPs ranging from 5 nm to 3 μm was observed.[81] In general, SiNPs prepared from thermally-induced decomposition of silane suffer from wide size distributions and poor nanoparticle crystallinity.

Plasma-Induced Decomposition

One of the most popular and enduring methods for SiNP synthesis is the decomposition of silane in plasma. One variant of this protocol using nonthermal plasma has seen continued development over the last 30 years. The critical difference between a conventional plasma and a nonthermal plasma is the temperature of the constituent species. In a conventional plasma, the temperature of the ions and free plasma electrons is the same. Conversely, in nonthermal plasmas, the temperature of electrons are typically between 10 000–50 000 K while the heavier gas species remain close to room temperature.[82] These plasmas are generated by oscillating a strong electric field within a gas flow, accelerating electrons until they have sufficient energy to ionize gas molecules. This can start a cascading effect, drastically increasing the density of free electrons within the chamber until a steady state in reached.[66,82]

[1.4] $Ar + e^-_{fast} \rightarrow Ar^+ + 2e^-_{slow}$

When subject to the energetic electrons of the plasma, silanes form radicals and a silicon hydride anion. Two examples of these reactions are given below, but hundreds of different chemical species have been proposed to exist within the plasma.[82,83]

[1.5] $SiH_4 + e^- \rightarrow SiH_2 + 2H + e^-$ (Electron dissociation)

[1.6] $SiH_4 + e^- \rightarrow SiH_2^- + 2H$ (Electron attachment)

The silylene ($Si_nH_{2n}^-$) or silyl ($Si_nH_{2n+1}^-$) anions become reactive points for silane molecules, and lead to the formation of small anionic clusters. Aggregation of these clusters eventually affords small, negatively charged nanoparticles. At this point, electrostatic repulsion prevents the particles from interacting and further SiNP growth is driven solely by reactions with silane and its dissociated constituents (both ionic and neutral). At small sizes (< 5 nm), these exothermic surface reactions can heat the SiNPs to temperatures hundreds of degrees greater than the surrounding gas (T ~ 800 K) and promote silicon crystallization. The crystallization of larger (~10 nm) SiNPs is believed to result from epitaxial growth on the crystalline seeds.[82]

Much of the recent development for SiNP syntheses using nonthermal plasma can be credited to the Kortshagen group. They produced multiple flow-through plasma reactors capable of tuning nanocrystal size by adjusting silane concentration, gas flow rates, and/or reactor pressure.[84] Their recent innovations include a tandem nonthermal plasma-tube furnace system that synthesizes SiNPs and modifies their surface entirely within the reactor.[85] After leaving the plasma afterglow, a flow of hydrogen gas and alkene ligands are introduced to the SiNPs before briefly annealing in a tube furnace (Figure 1-8a). Functionalized particles prepared this way achieved a maximum quantum yield of 20%.[85] Other work from Eslamisaray *et al.* targeted the production of large SiNPs for Mie scattering.[86] The synthesis of SiNPs larger than 10 nm has historically been difficult due to short residence times and particle electrostatic repulsion.[25] This was overcome by electrostatically trapping nanoparticles within the reactor, allowing them to reach sizes spanning 60–214 nm (Figure 1-8b). SiNPs produced using nonthermal plasma typically possess narrow size distributions due to electrostatic repulsion from the SiNP surface.[25] Remarkable, even for particles exceeding 100 nm in diameter, the authors observed a size distribution of only 5.4% from the mean.[86]

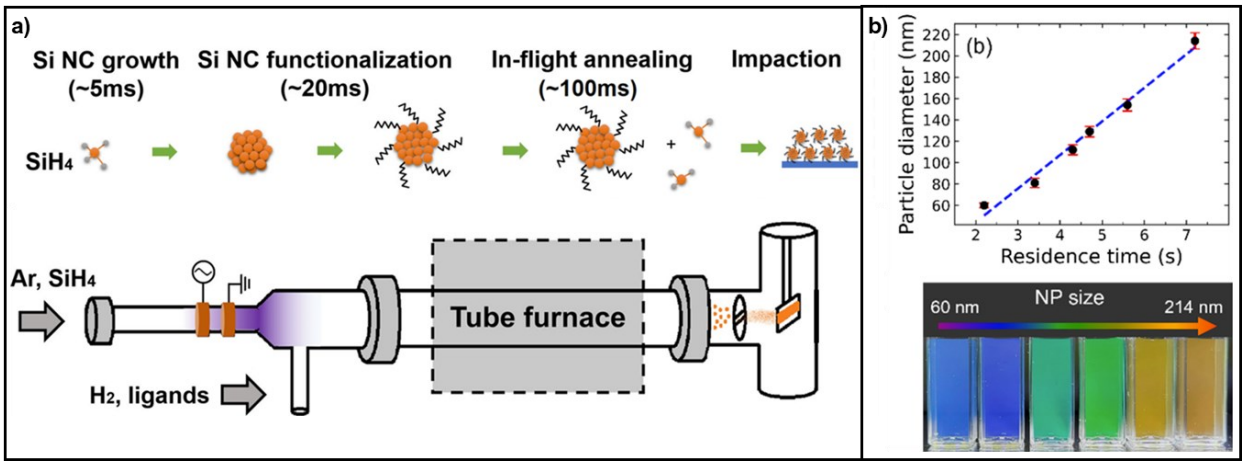

Figure 1-8. Recent innovations for non-thermal plasma synthesis of SiNPs. (a) Tandem plasma-tube furnace system for SiNP nucleation, growth and surface functionalization; adapted from *Chem. Mater*. **2019**, *31*, 8451−8458 (Ref. 85). (b) Increasing residence time in the tube using an electrostatic trap increased SiNP size (top). The size-dependent light scattering of silicon nanocrystals (bottom); adapted from *Nano Lett*. **2023**, *23*, 1930−1937 (Ref. 86).

Evident from the above sections is the predominant use of silane (SiH_4) for low-pressure syntheses of SiNPs. This pyrophoric molecule presents an undesirable safety concern, and, as such, alternative precursors have been explored. Examples of this include work by Guruvenket *et al*. using cyclohexasilane (Si_6H_{12}) as a pyrolysis reagent[87] and Yasar-Inceoglu *et al.* using silicon tetrachloride ($SiCl_4$) in a nonthermal plasma synthesis.[88] While both alternatives produced SiNPs, the quantum dots prepared from cyclohexasilane exhibited low PLQY values ($\leq$ 13%), and SiNPs prepared from $SiCl_4$ contained Cl impurities and required a relatively greater amount of power to crystallize.[87, 88]

1.3.4 Thermal Treatment of Silicon-rich Oxides

The final category of SiNP syntheses to be discussed is the thermally-induced decomposition of silicon-rich oxides (SROs). More accurately, these reactions describe the disproportionation of non-stoichiometric silicon oxides into domains of oxidized Si(IV) and reduced Si(0). The general formula for this reaction is presented below:

[1.7] $$2\ SiO_{x\,(s)} \rightarrow (2-x)\ Si_{\,(s)} + \ x\ SiO_{2\,(s)} \qquad (0 < x < 2)$$

The thermodynamically unstable SROs will disproportionate when subject to heat and render nano-sized domains of Si trapped within a 3-dimensional matrix of SiO_2. This method conveniently provides SiNPs in a protective encapsulation from a single starting material. The average particle size can be tuned by either modifying the SRO composition (ratio of Si to O) or adjusting the thermal processing temperature and time.[89] SiNPs formed this way are amorphous until approximately 1000°C, after which they begin to crystallize.[90-93]

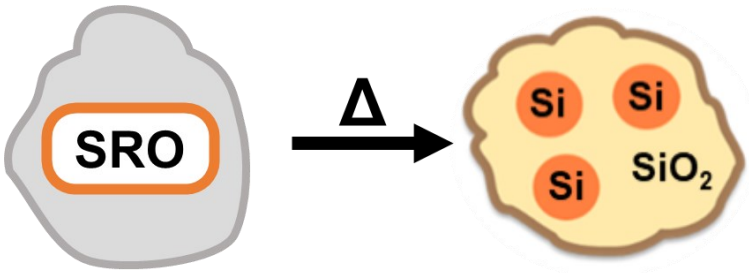

Figure 1-9. Oxide-embedded SiNPs prepared by thermal treatment of silicon rich oxides.

The most common methods used to make SROs are ion implantation, sputtering, vapour deposition, and silane hydrolysis-condensation. By the 1990s, these techniques were already established procedures, but each saw rapid development for SRO preparation shortly after quantum confinement was discovered in nano-silicon.

Ion implantation

Ion implantation describes a process in which charged particles of a desired element are accelerated into a chosen substrate. This beam of ions is rastered across the substrate, penetrating the surface, implanting ions into the material, and modifying its composition. This process, while versatile in element selection, is restricted by the penetration depth of the incident ions and therefore is only appropriate for the preparation of thin films. In the context of SRO preparation, Si^+ ions are bombarded into a SiO_2 substrate, creating a zone of excess silicon atoms stretching up to approximately 300 nm below the SiO_2 surface. [94-97] The small NP yields and irregular nanoparticle morphologies resulting from the SROs produced in this way have limited the use of ion implantation and the technique is mostly confined to doping silicon surfaces.[98]

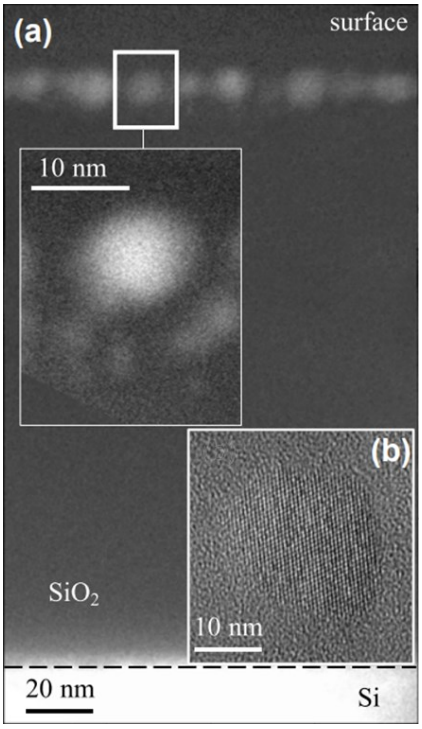

Figure 1-10. Electron microscopy of SiNPs synthesized using an ion implantation method. (a) Cross-section image. (b) High-resolution image of the nanocrystal. Adapted from *Nanophotonics*, **2022**, *11*, 3485–3493 (Ref. 97).

Sputtering

One of the downsides to ion implantation is the inadvertent destruction of the substrate caused by the high energy collisions from the incident ions. However, this same phenomenon is used advantageously for sputtering techniques. Sputtering methods use a beam of particles to eject atoms from a target material by transferring momentum from the particles to the target atoms such that the atoms are physically ejected.[99] For SRO preparation, this can be accomplished using a plasma of Ar^+ ions striking Si and SiO_2 targets concurrently.[100,101] This process is often referred to as co-sputtering because it uses multiple target materials. Another approach, termed reactive sputtering, places Si targets in a controlled mixture of argon and oxygen gas, allowing a partial oxidation of the ejected Si atoms.[102] In both cases, films of SiO_x are formed as the ejected atoms are deposited on a designated substrate.

Silicon Monoxide and Vapour Deposition Techniques

Of the SiO_x materials, the most commonly employed compound for SiNP synthesis is the amorphous solid known as "silicon monoxide".[25,103-106] Often referred to as SiO or $SiO_{(am)}$, this material has been the topic of a long debate as to whether $SiO_{(am)}$ exists as a unique compound or as a nanoscale mixture of Si and SiO_2.[107-111] Conversely, the diatomic and volatile $SiO_{(g)}$ molecule is a well-studied species. It is particularly important in the fields of metallurgy, where $SiO_{(g)}$ is encountered as a problematic impurity in the synthesis of single Si crystals;[112] and astronomy, where $SiO_{(g)}$ is suggested to be the most abundant form of Si atoms in the universe.[113,114] The materials science community is plagued by the careless and ambiguous use of the term "silicon monoxide". To avoid confusion this thesis will use $SiO_{(am)}$ to refer to the solid amorphous material and $SiO_{(g)}$ when discussing the molecular species. The debate regarding the makeup of $SiO_{(am)}$ as a distinct material will not be addressed as it is inconsequential for SiNP synthesis.

Conveniently, $SiO_{(g)}$ can be produced by the reaction of silica with carbon, silicon carbide, or pure silicon.

[1.8] $C_{(s)} + SiO_{2\,(s)} \rightarrow SiO_{(g)} + CO_{(g)}$

[1.9] $SiC_{(s)} + 2SiO_{2\,(s)} \rightarrow 3\ SiO_{(g)} + CO_{(g)}$

[1.10] $Si_{(s)} + SiO_{2\,(s)} \rightarrow 2\ SiO_{(g)}$

The $SiO_{(g)}$ is then carefully condensed onto a substrate as $SiO_{(am)}$. Like other SROs, $SiO_{(am)}$ will disproportionate when subject to heat, eventually forming crystalline SiNPs at approximately 1000°C.[104]

[1.11] $2\ SiO_{(g)} \rightarrow Si_{(s)} + SiO_{2\,(s)}$

Compared to ion implantation and sputtering, the vapour deposition method facilitated SRO preparation and, consequently, $SiO_{(am)}$ became a commercially available product. This made $SiO_{(am)}$ a popular precursor material for oxide-embedded and freestanding SiNPs in the academic literature.[25,103-106]

SiO_x can also be prepared using chemical vapour deposition (CVD) of SiH_4 in the presence of oxygen gas.[115,116] This technique is useful for the preparation of a Si/SiO_2 or $SiNP/SiO_2$ superlattice: a multilayered film of crystalline Si and amorphous SiO_2.[117]

The final SRO pertinent to this discussion differs significantly from the SiO_x materials described above. Formed from the hydrolysis and condensation of silanes, hydrogen silsesquioxane has distinguished itself as a prominent SiNP precursor and, given its central role in this thesis, it will be discussed in greater detail.

Hydrogen Silsesquioxane

The term silsesquioxane describes a class of materials composing a polymeric network of Si–O–Si linkages decorated with organic groups. These glassy polymers, sometimes called polyhedral oligomeric silsesquioxanes (POSS), can be generally formulated as $(RSiO_{1.5})_n$ or $(RSiO_{3/2})_n$ with R representing virtually any organic group. The vast array of possible molecules allows these compounds to cover a range of functions, particularly in the field of ceramics, where the strong thermal and mechanical properties brought on by Si–O bonds are beneficial.[118]

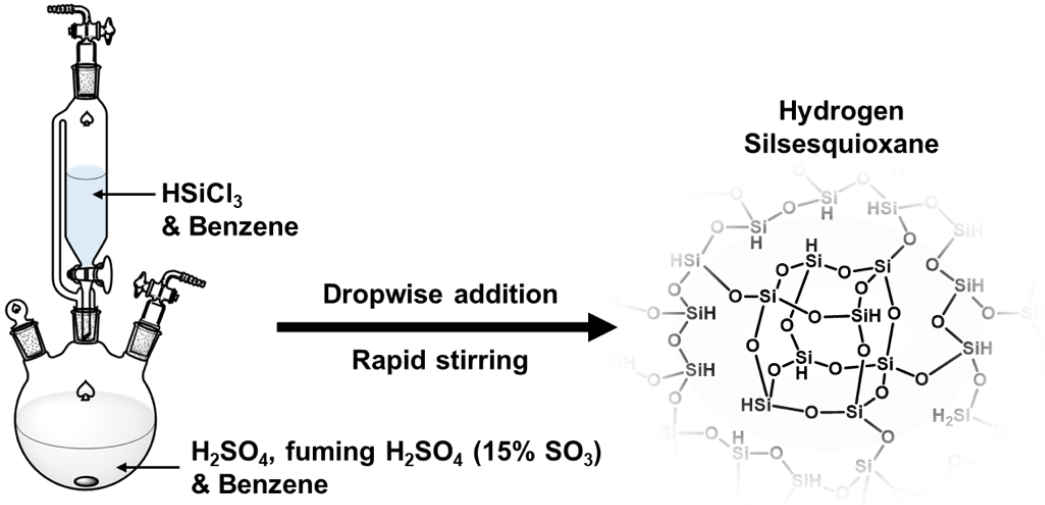

Figure 1-11. The "scarce-water" reaction scheme for the synthesis of hydrogen silsesquioxane based on work by Frye and Collins.[119]

The simplest silsesquioxane is the hydride derivative: hydrogen silsesquioxane (HSQ, or $HSiO_{1.5}$). The history of HSQ predates it association with SiNPs. Synthesized for the first time by Frye and Collins in 1970,[119] the polymer eventually became a well-known negative resist for electron-beam (e-beam) lithography. Upon exposure to high-energy electrons, Si–H bond scission within HSQ triggers the polymer to crosslink through the formation of additional siloxane bonds.[120] This procedure results in a greater resistance to alkaline dissolution, leaving the cured

regions of HSQ intact after application of the lithography developer (solvent). Research through the 1990s and 2000s praised the e-beam resist for its high-resolution (< 10 nm) and small line edge roughness.[121] Another common application saw HSQ used as a substitute for SiO_2 as a spin-on interlayer dielectric material for integrated circuits.[122] The commercial availability of HSQ combined with its solution processability and well-understood siloxane chemistry made it an attractive material for modeling silica surfaces.[93,118] Still, other silsesquioxanes were explored for catalysis, material strengthening, and drug-delivery.[118]

The Dow Corning Corporation was the sole commercial supplier of HSQ throughout the 1990s, 2000s, and early 2010s. The company sold HSQ in a solution of methyl isobutyl ketone (MIBK) under the trade name *Flowable Oxide* (FOx-X; X = batch number). Nearly all publications during this time credited Dow Corning with supplying the HSQ used in their experiments. In 2006, a study by Dow Corning's Analytical Sciences Department described how the molecular weight distribution and specific molecular structures within HSQ can vary greatly depending upon the synthetic reaction conditions.[123] The authors remarked that HSQ contains a diverse composition of polyhedral cages, ladders, tubes, partial cages, interconnected cages, and random structures.[123] Despite this range of structures, the consistency between batch numbers of *Flowable Oxide* made experiments easy to replicate and, as a result, many authors praised HSQ for its well-defined nature. A selection of the molecular structures comprising HSQ are illustrated in Figure 1-12, and their influence on silicon nanocrystal synthesis will be addressed later.

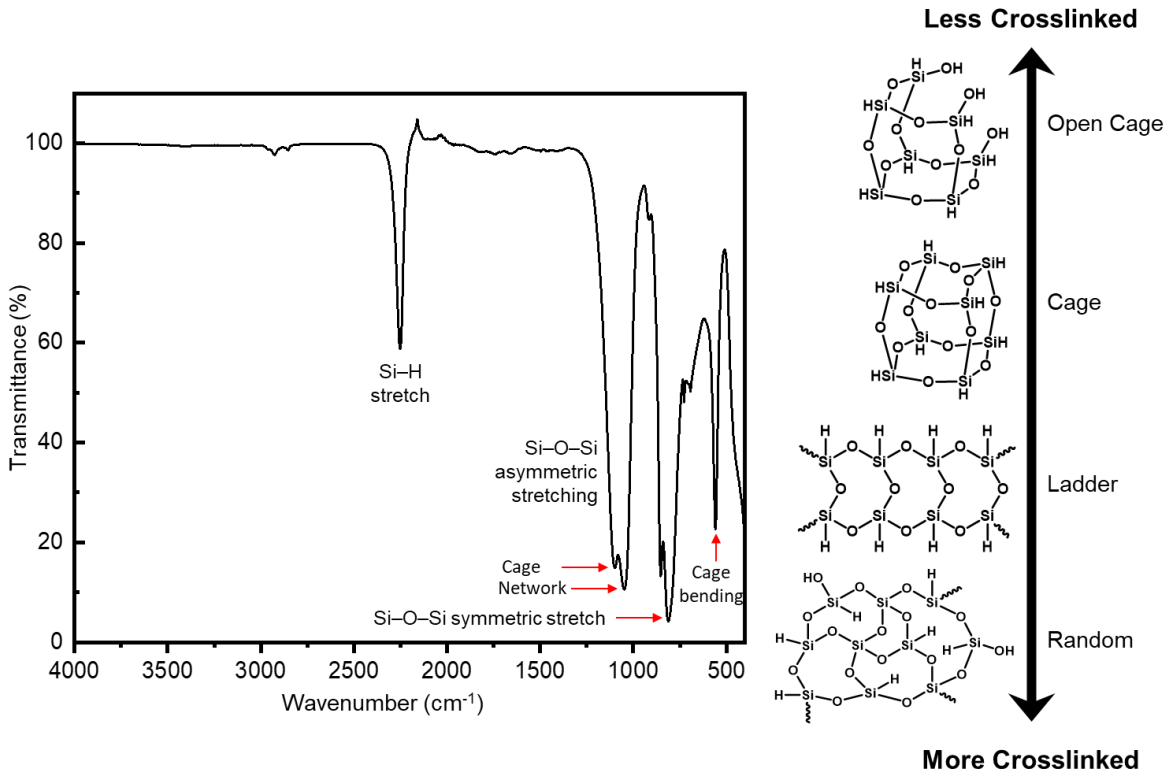

Figure 1-12. Fourier-transform infrared (FTIR) spectrum of HSQ (left) and common molecular structures that compose HSQ (right). More crosslinking is associated with greater network character in the polymer.

The local bonding environment within HSQ consists of Si–H bonds and Si–O–Si linkages. These give rise to the characteristic stretching frequencies observed in the infrared spectrum (Figure 1-12). Compared to the four Si–O bonds present in silicon dioxide, the Si atoms within HSQ only make three oxygen bonds and the resulting system is oxygen deficient. For this reason, HSQ and other $RSiO_{1.5}$ polymers are often recognized as silicon suboxides, and this framing was critical to their discovery as precursor materials for silicon nanocrystals.

The first example of hydrogen silsesquioxane used for silicon nanoparticle synthesis was reported by Pauthe *et al.* in 1999.[124] Their synthesis of HSQ differed from that of Frye and Collins, substituting triethoxysilane for trichlorosilane in the acidic hydrolysis-condensation reaction. After

a complicated procedure of dehydration and densification, the authors produced a film of silicon nanocrystals (5–20 nm) embedded in a silica matrix.[124] Subsequent studies simplified this method and demonstrated that silicon nanocrystals began to form around 1050°C.[92]

Inspired by these early efforts, Hessel *et al*. explored the use of Dow Corning's commercially available HSQ as a precursor for silicon nanocrystals.[93] The work was motivated by a desire to produce freestanding SiNPs with controllable size, shape, crystallinity, polydispersity, and surface chemistry while avoiding the use of the specialized and highly technical equipment often used to make other SROs. Additionally, the origin of photoluminescence from SiNPs was a topic of ongoing study, and it was hoped that HSQ could provide a straightforward, cost-effective, and scalable method for the preparation of silicon quantum dots.[93] In his initial publications, Hessel thoroughly characterized the effects of thermal processing on solid HSQ.[93,125] Under a constant flow of forming gas (mixture of 5% H_2 and 95% N_2), samples of HSQ were heated in a tube furnace to a peak processing temperature between 300 and 1100°C. After the 1 h dwell time (reaction time) had elapsed, the system was allowed to cool naturally to room temperature and the samples were removed and ground to a powder using a mortar and pestle. The authors observed that the thermal processing temperature changed the appearance of the white HSQ into shades ranging from brown to black, with higher temperatures rendering darker samples. At the time, HSQ was known to release silane gas (SiH_4) when heated above 350°C.[126,127] This, combined with the characterization of the thermally treated powders, formed the basis of a SiNP formation mechanism. Specifically, Hessel *et al*. proposed that silicon nanocrystals form within HSQ via a three-stage process:[125]

1) *HSQ Structural Changes (≤ 400°C).* Solvent is driven off from the sol-gel and structural changes, such as cross-linking and cage rearrangement, occur within the HSQ (Figure 1-12).
2) *Formation and Growth of Oxide-Embedded Si Nanodomains (500–900°C).* Silane Si–H bonds begin to decompose and Si–Si bonds emerge and organize into amorphous nanodomains.
3) *Nanodomain Crystallization and Particle Growth (≥ 1000°C).* The high temperatures required for silicon crystallization are reached and the nanoparticles crystallize. Increasing the temperature further promotes particle growth and larger nanocrystals are obtained.

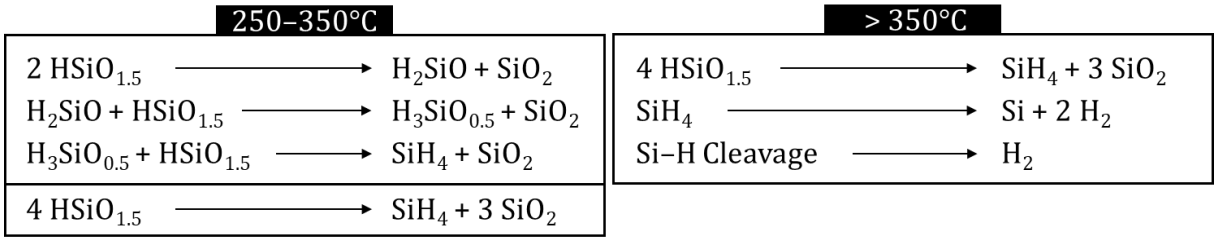

Figure 1-13. Reactions associated with the thermal decomposition of HSQ.[93]

These combined works established the minimum thermal treatment required for silicon nanocrystal formation and demonstrated the relationship between processing temperature and silicon nanoparticle size. Similar to other SROs, higher temperatures promoted SiNP growth and eventually the average particle size was reported for processing at various temperatures between 1100–1500°C (Table 1-1).[23,128] While thermal treatments were often standardized at 1 h, it was also known that prolonged exposure to high temperatures encouraged SiNP growth with a subsequent increase in particle size.[129]

Table 1-1. HSQ Heating and Silicon Nanoparticle Size

Processing Temperature (°C) [a]	Nanoparticle Size (nm) [b]
1100	3.5 ± 0.9
1200	5.5 ± 1.2
1300	8.7 ± 1.2
1400	20.7 ± 4.0
1500	64.0 ± 16.9

[a] HSQ heated at the processing temperature for 1 h (dwell time).

[b] nanoparticle size determined by electron microscopy.[23]

A follow-up report from Henderson *et al.* sought to compare SiNPs derived from Dow Corning's HSQ (FOx-X) to those from a $(HSiO_{1.5})_n$ polymer prepared in the laboratory.[130] The sol-gel provided by Dow Corning contained a lower cross-linking density and produced larger SiNPs under identical conditions (Figure 1-14a). The authors reasoned that the lower network character and greater number of cage structures decreased the energetic requirements for Si atom diffusion through the silica matrix, promoting the formation of larger SiNPs. The authors also prepared a methylsilsesquioxane and a $(HSiO_{1.5})_n(CH_3SiO_{1.5})_m$ ($m \ll n$) copolymer in the hope that the steric bulk from a methyl group would limit the polymeric cross-linking. At low methyl concentrations the desired Si atom mobility was facilitated by an opening of the network. However, beyond 10% CH_3 ($m > 0.1$) the compositional effects of unavailable Si atoms bound in oxycarbide phases outweighed the structural effects and SiNP size decreased.[130] Further experiments showed that alternating the $(RSiO_{1.5})_n$ functional group with large organic molecules (R = phenyl, octyl, decyl) resulted in the formation of oxide-embedded silicon carbide (SiC) nanocrystals.[131,132]

Recent publications from the Saitow lab featured similar manipulation of the HSQ structure by varying the amounts of solvent during synthesis.[133,134] Higher water-to-solvent ratios lead to a greater cross-linking density through the creation of additional Si(IV) sites. A greater degree of network structures resulted in smaller SiNPs with a reduced yield and crystallinity, confirming the conclusions of Henderson *et al*. Again, Si atom diffusion through the silica matrix was believed to be the cause for the differences in SiNP products (Figure 1-14b).[133,134]

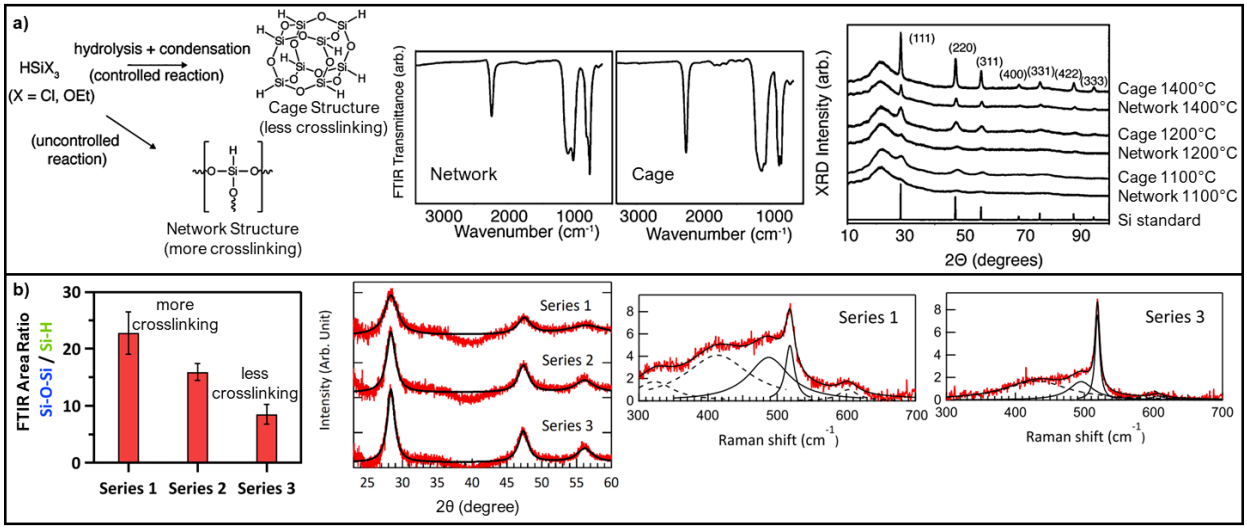

Figure 1-14. HSQ crosslinking and SiNP size. (a) A comparison of Dow Corning HSQ (cage structure) and a $(HSiO_{1.5})_n$ polymer (network structure) prepared in the laboratory; adapted from *Chem. Commun*. **2010**, *46*, 8704–8718 (Ref. 89). (b) A comparison of HSQ precursors prepared with more (Series 1) and less (Series 3) crosslinking; adapted from *Chem. Mater.* **2020**, *32*, 8382−8392 (Ref. 134).

It is worth noting that the above studies chose to hydrolyse solutions of trichlorosilane ($HSiCl_3$) by adding water directly to the reaction mixture. This method provides less control over the hydrolysis of silanes and reduces the number of Si–H bonds available for thermal disproportionation. While the exact procedure used by the Dow Corning Corporation for making Flowable-Oxide is proprietary, it is known the HSQ isolated from FOx contains a greater degree

of cage structures. For this reason, the HSQ supplied by Dow Corning likely uses the "scarce-water" reaction conditions as first reported by Frye and Collins.[119] All recent SiNP studies from the Veinot group have used HSQ synthesised using the "scarce-water" method (Figure 1-11).[8,12,14,23,24]

The use of HSQ over other Si-rich oxide precursors offers multiple advantages. Importantly, its preparation benefits from being a solution-based procedure. Recall that SROs made from chemical vapour deposition or ion-implantation require precise instrumentation operating in high-vacuum chambers. In addition to being expensive, these techniques are often inherently limited in practical scalability and ease-of-use. HSQ also benefits from its solution processability, allowing the polymer to be dissolved in organic solvents such as toluene or methyl isobutyl ketone. This makes techniques like spin-coating possible and provides as easier route to thin-film preparation than the thermal evaporation necessary for other SROs.

Another significant advantage for using HSQ is the exceptional photoluminescence of the Si quantum dots produced by its disproportionation. Relative to other SiNP preparations, the accessible PL range and PL quantum yields are consistently greater for SiNPs prepared via HSQ disproportionation.[25] Quantum dots prepared from HSQ have even outperformed other SRO materials. A 2018 study by Zhou *et al*. compared thin films of Si nanocrystals embedded in SiO_2 prepared by heating HSQ and SiO_x precursors.[135] Although films prepared from HSQ resulted in a lower volume fraction of SiNPs than films prepared from SiO_x (17% vs. 26%), the HSQ-prepared films displayed a PL intensity approximately six times greater than that of the SiO_x films. The authors speculated that higher spatial density of SiNPs in the SiO_x films may be responsible for fluorescence quenching.[135]

Unfortunately, like all disproportionation-based SiNP syntheses, the use of HSQ as a precursor suffers from a poor atom economy. Using the stoichiometry presented in Figure 1-13, the theoretical ratio of silicon atoms available to form nanoparticles is 1 in 4. While HSQ synthesis can achieve yields exceeding 95%,[130] at least 75% of the Si atoms present in HSQ will fully oxidize to Si(IV) after heating. Experimental results are worse as SiNP yields from heating HSQ are typically about 10%.[25,134] Additionally, the generation of freestanding SiNPs necessitates chemical etching of the surrounding silicon oxide matrix with hydrofluoric acid. While the resulting Si–H surface bonds provide an excellent substrate for further chemical functionalization, this step introduces a dangerous hazard into the procedure.

1.4 Thesis Outline

The objective of the research described in this thesis is to synthesize SiNPs possessing diameters exceeding 75 nm using HSQ. During our investigation, additional questions arose concerning the role of $SiO_{(g)}$ and the processing atmosphere during thermal treatment. Along with a summary of the academic literature concerning the synthesis of SiNPs, this introduction outlines the unique requirements related to some of the most promising SiNP applications. The remainder of this Chapter is centered on the synthesis of silicon nanocrystals from the thermal disproportionation of hydrogen silsesquioxane. Chapter 2 focuses on expanding our understanding of the high-temperature behaviour of HSQ. Specifically, a strange anomaly in SiNP growth was discovered and its origins are discussed. Chapter 3 focuses on the effects of the gas environment during thermal treatment through the analysis of nanocrystals grown under reducing, inert, and oxidizing atmospheres.

1.5 References

1. Feldman, L. C. Introduction. In *Fundamental Aspects of Silicon Oxidation*; Chabal, Y. J., Ed.; Springer Series in Materials Science; Springer: Berlin, 2001; Vol. 46, pp 1–11.
2. Ameta S. C. Nanomaterials: An Introduction. In *The Science of Nanomaterials: Basics and Applications*; Ameta S. C.; Ameta, R., Ed.; Apple Academic Press: New York, 2022; pp 1–18.
3. Lehmann, V.; Gösele, U. Porous silicon: Quantum sponge structures grown via a self-adjusting etching process. *Adv. Mater*. **1992**, *4*, 114–116.
4. Canham, L. T. Silicon quantum wire array fabrication by electrochemical and chemical dissolution of wafers. *Appl. Phys. Lett*. **1990**, *57*, 1046–1048.
5. Sailor, M.J. Preparation of Micro-, Meso-, and Macro-Porous Silicon Layers. In *Porous Silicon in Practice: Preparation, Characterization and Applications*, Sailor, M. J., Ed.; Wiley: 2011; pp 43-76.
6. Faure, G. *Principles and Applications of Inorganic Geochemistry : A Comprehensive Textbook for Geology Students*. Macmillan Pub. Co.: New York, 1991.
7. Reiss, P.; Carrière, M.; Lincheneau, C.; Vaure, L.; Tamang, S. Synthesis of Semiconductor Nanocrystals, Focusing on Nontoxic and Earth-Abundant Materials. *Chem. Rev.* **2016**, *116*, 10731−10819.
8. Warner, J. H.; Hoshino, A.; Yamamoto, K.; Tilley, R. D. Water-Soluble Photoluminescent Silicon Quantum Dots. *Angew. Chem. Int. Ed*. **2005**, *44*, 4550−4554.
9. Park, J. H.; Gu, L.; Maltzahn, G.; Ruoslahti, E.; Bhatia, S. N.; Sailor, M. J. Biodegradable luminescent porous silicon nanoparticles for in vivo applications. *Nat. Mater*. **2009**, *8*, 331–336.
10. Cheong, I. T.; Mock, J.; Kallergi, M.; Groß, E.; Meldrum, A.; Rieger, B.; Becherer, M.; Veinot, J. G. C. Colloidal Silicon Quantum Dot-Based Cavity Light-Emitting Diodes with Narrowed and Tunable Electroluminescence. *Adv. Opt. Mater.* **2023**, *11*, 2201834.
11. Erogbogbo, F.; Yong, K. T.; Roy, I.; Hu, R.; Law, W. C.; Zhao, W.; Ding, H.; Wu, F.; Kumar, R.; Swihart, M. T.; Prasad, P. N. In Vivo Targeted Cancer Imaging, Sentinel Lymph Node Mapping and Multi-Channel Imaging with Biocompatible Silicon Nanocrystals. *ACS Nano* **2011**, *5*, 413–423.

12. Cheong, I. T.; Morrish, W.; Sheard, W.; Yu, H.; Luppi, B. T.; Milburn, L.; Meldrum, A.; Veinot, J. G. C. Silicon Quantum Dot–Polymer Fabry–Pérot Resonators with Narrowed and Tunable Emissions. *ACS Appl. Mater. Interfaces* **2021**, *13*, 27149−27158.
13. Meinardi, F.; Ehrenberg, S.; Dhamo, L.; Carulli, F.; Mauri, M.; Bruni, F.; Simonutti, R.; Kortshagen, U.; Brovelli, S. Highly Efficient Luminescent Solar Concentrators Based on Earth-Abundant Indirect-Bandgap Silicon Quantum Dots. *Nat. Photonics* **2017**, *11*, 177–185.
14. Milburn, L.; Robidillo, C.J.; Dalangin, R.; Shen, Y.; Veinot, J. G. C. A Complementary Silicon Quantum Dot-Enzyme Platform for the Selective Detection of Nitroaromatic Compounds: Explosives versus Nerve Agents. *ACS Appl. Nano Mater.* **2022**, *5*, 11984−11990.
15. Canham, L. Introductory Lecture: Origins and Applications of Efficient Visible Photoluminescence from Silicon-Based Nanostructures. *Faraday Discuss.* **2020**, *222*, 10−81.
16. Sato, K.; Tsuji, H.; Hirakuri, K.; Fukata, N.; Yamauchi, Y. Controlled Chemical Etching for Silicon Nanocrystals with Wavelength-Tunable Photoluminescence. *Chem. Commun.* **2009**, 3759−3761.
17. Shirahata, N.; Nakamura, J.; Inoue, J. I.; Ghosh, B.; Nemoto, K.; Nemoto, Y.; Takeguchi, M.; Masuda, Y.; Tanaka, M.; Ozin, G. A. Emerging Atomic Energy Levels in Zero-Dimensional Silicon Quantum Dots. *Nano Lett.* **2020**, *20*, 1491–1498.
18. Beard, M. C.; Knutsen, K. P.; Yu, P.; Luther, J. M.; Song, Q.; Metzger, W. K.; Ellingson, R. J.; Nozik, A. J. Multiple Exciton Generation in Colloidal Silicon Nanocrystals. *Nano Lett.* **2007**, *7*, 2506–2512.
19. Lin, S. W.; Chen, D. H. Synthesis of Water-Soluble Blue Photoluminescent Silicon Nanocrystals with Oxide Surface Passivation. *Small* **2009**, *5*, 72–76.
20. Brus, L. E.; Szajowski, P. F.; Wilson, W. L.; Harris, T. D.; Schuppler, S.; Citrin, P. H. Electronic Spectroscopy and Photophysics of Si Nanocrystals: Relationship to Bulk c-Si and Porous Si. *J. Am. Chem. Soc.* **1995**, *117*, 2915–2922.
21. Yu, Y.; Fan, G.; Fermi, A.; Mazzaro, R.; Morandi, V.; Ceroni, P.; Smilgies, D. M.; Korgel, B. A. Size-Dependent Photoluminescence Efficiency of Silicon Nanocrystal Quantum Dots. *J. Phys. Chem. C* **2017**, *121*, 23240–23248.

22. Anthony, R.; Kortshagen, U. Photoluminescence Quantum Yields of Amorphous and Crystalline Silicon Nanoparticles. *Phys. Rev. B* **2009***, 80*, 115407.
23. Thiessen, A. N.; Ha, M.; Hooper, R. W.; Yu, H.; Oliynyk, A. O.; Veinot, J. G. C.; Michaelis. Silicon Nanoparticles: Are They Crystalline from the Core to the Surface? *Chem. Mater*. **2019**, *31*, 678−688.
24. Thiessen, A. N.; Zhang, L.; Oliynyk, A. O.; Yu, H.; O'Connor, K. M.; Meldrum, A.; Veinot, J. G. C. A Tale of Seemingly "Identical" Silicon Quantum Dot Families: Structural Insight into Silicon Quantum Dot Photoluminescence. *Chem. Mater.* **2020***, 32,* 6838−6846.
25. Milliken, S.; Thiessen, A. N.; Cheong, I. T.; O'Connor, K. M.; Li, Z.; Hooper, R. W.; Robidillo, C. J. T.; Veinot, J. G. C. "Turning the dials": Controlling Synthesis, Structure, Composition, and Surface Chemistry to Tailor Silicon Nanoparticle Properties. *Nanoscale,* **2021***, 13,* 16379–16404.
26. Dasog, M.; De, l. R.; Titova, L. V.; Hegmann, F. A.; Veinot, J. G. C. Size vs Surface: Tuning the Photoluminescence of Freestanding Silicon Nanocrystals Across the Visible Spectrum via Surface Groups. *ACS Nano* **2014***, 8*, 9636–9648.
27. Sinelnikov, R.; Dasog, M.; Beamish, J.; Meldrum, A.; Veinot, J. G. C. Revisiting an Ongoing Debate: What Role Do Surface Groups Play in Silicon Nanocrystal Photoluminescence? *ACS Photonics* **2017**, *4*, 1920–1929.
28. Manthiram, A. Material Aspects: An Overview. In *Lithium Batteries*; Nazri, G. A.; Pistoia, G., Ed.; Science and Technology; Springer: New York, 2003; pp 3–41.
29. Julien, C.; Mauger, A.; Vijh, A.; Zaghib, K. *Lithium Batteries*; Science and Technology; Springer: New York, 2015.
30. Entwistle, J.; Rennie, A.; Patwardhan, S. A Review of Magnesiothermic Reduction of Silica to Porous Silicon for Lithium-Ion Battery Applications and Beyond. *J. Mater. Chem. A* **2018**, *6*, 18344–18356.
31. Zamfir, M. R.; Nguyen, H. T.; Moyen, E.; Leeac, Y. H.; Pribat, D. Silicon Nanowires for Li-Based Battery Anodes: A Review. *J. Mater. Chem. A* **2013**, *1*, 9566–9586.
32. Aghajamali, M.; Xie, H.; Javadi, M.; Kalisvaart, W. P.; Buriak, J. M.; Veinot, J. G. C. Size and Surface Effects of Silicon Nanocrystals in Graphene Aerogel Composite Anodes for Lithium Ion Batteries. *Chem. Mater.* **2018**, *30*, 7782–7792.

33. Zhu, G.; Luo, W.; Wang, L.; Jiang, W.; Yang, J. Silicon: Toward Eco-friendly Reduction Techniques for Lithium-ion Battery Applications. *J. Mater. Chem. A* **2019**, *7*, 24715–24737.
34. Magasinski, A.; Dixon, P.; Hertzberg, B.; Kvit, A.; Ayala, J.; Yushin, G. High-Performance Lithium-ion Anodes Using a Hierarchical Bottom-up Approach. *Nat. Mater.* **2010**, *9*, 353–358.
35. Pendry, J. B.; Schurig, D.; Smith, D. R. Controlling Electromagnetic Fields. *Science* **2006**, *312*, 1780–1782.
36. Jahani, S.; Jacob, Z. All-Dielectric Metamaterials. *Nat. Nanotechnol.* **2016**, *11*, 23–36.
37. Zhang, C.; Xu, Y.; Liu, J.; Li, J.-T.; Xiang, J.; Li, H.; Li, J.-X.; Dai, Q.-F.; Lan, S.; Miroshnichenko, A. E. Lighting up Silicon Nanoparticles with Mie Resonances. *Nat. Commun.* **2018**, *9*, 2964.
38. Kuznetsov, A. I.; Miroshnichenko, A. E.; Brongersma, M. L.; Kivshar, Y. S.; Luk'yanchuk, B. Optically Resonant Dielectric Nanostructures. *Science* **2016**, *354*, aag2472.
39. De Marco, M. L.; Semlali, S.; Korgel, B. A.; Barois, P.; Drisko, G. L.; Aymonier, C. Silicon-Based Dielectric Metamaterials: Focus on the Current Synthetic Challenges. *Angew. Chem. Int. Ed.* **2018**, *57*, 4478–4498.
40. De Marco, M. L. Supercritical Synthesis of High Refractive Index Silicon Particles for Optical Metamaterials. Ph.D. Dissertation, Université de Bordeaux, 2019.
41. Hidemasa Negoro; Sugimoto, H.; Fujii, M. Helicity-Preserving Optical Metafluids. *Nano Lett.* **2023**, *23*, 5101–5107.
42. Wang, L.; Reipa, V.; Blasic, J. Silicon Nanoparticles as a Luminescent Label to DNA. *Bioconjugate Chem*. **2004**, *15*, 409−412.
43. Choi, J.; Wang, N. S.; Reipa, V. Photoassisted Tuning of Silicon Nanocrystal Photoluminescence. *Langmuir* **2007**, *23*, 3388−3394.
44. Jung, K. H.; Shih, S.; Hsieh, T. Y.; Kwong, D. L.; Lin, T. L. Intense Photoluminescence from Laterally Anodized Porous Si. *Appl. Phys. Lett.* **1991**, *59*, 3264–3266.
45. Hwang, J.; Jeong, Y.;Lee, K. H.; Seo, Y.; Kim, J.; Hong, J. W.; Kamaloo, E.; Camesano, T. A.; Choi, J. Simple Preparation of Fluorescent Silicon Nanoparticles from Used Si Wafers. *Ind. Eng. Chem. Res.* **2015**, *54*, 5982–5989.

46. Zhu, J.; Wu, Yd.; Li, Th.; Chen, H.; Fan, L.; Xiao, C. Silicon Nanocrystallites Produced Via a Chemical Etching Method and Photoluminescence Properties. *J. Mater. Sci.* **2014**, *49*, 4349–4353.

47. Zhang, D.; Gökce, B.; Barcikowski, S. Laser Synthesis and Processing of Colloids: Fundamentals and Applications. *Chem. Rev.* **2017**, *117*, 3990−4103.

48. Ishikawa, Y.; Tsuji, T.; Sakaki, S.; Koshizaki, N. Pulsed laser melting in liquid for crystalline spherical submicrometer particle fabrication– Mechanism, process control, and applications. *Prog. Mater Sci*. **2023**, *131*, 101004.

49. Shirahata, N.; Hirakawaa, D.; Sakka, Y. Interfacial-related Color Tuning of Colloidal Si Nanocrystals. *Green Chem.* **2010**, *12*, 2139–2141.

50. Yuan, Z.; Nakamura, T.; Adachi, S.; Matsuishi, K. Improvement of Laser Processing for Colloidal Silicon Nanocrystal Formation in a Reactive Solvent. *J. Phys. Chem. C* **2017**, *121*, 8623–8629.

51. Kim, M.; Osone, S.; Kim, T.; Higashi, H.; Seto, T. Synthesis of Nanoparticles by Laser Ablation: A Review. *Kona Powder Part. J.* **2017**, *34*, 80–90.

52. Švrček, V.; Rehspringer, J. -L.; Gaffet, E.; Slaoui, A.; Muller, J. -C. Unaggregated Silicon Nanocrystals Obtained by Ball Milling. *J. Cryst. Growth* **2005**, *275*, 589–597.

53. Lam, C.; Zhang, Y. F.; Tang, Y. H.; Lee, C. S.; Bello, I.; Lee, S. T. Large-scale Synthesis of Ultrafine Si Nanoparticles. *J. Cryst. Growth* **2000**, *220*, 466–470.

54. Chaudhary, A. -L.; Sheppard, D. A.; Paskevicius, M.; Saundersc, M.; Buckley, C. E. Mechanochemical Synthesis of Amorphous Silicon Nanoparticles by Ball Milling. *RSC Adv*. **2014**, *4*, 21979–21983.

55. Kuang, L.; Mitchell, B. S.; Fink, M. J. Silicon nanoparticles synthesised through reactive high-energy ball milling: enhancement of optical properties from the removal of iron impurities. *J. Exp. Nanosci.* **2015**, *10*, 1214–1222.

56. Chaâbani, W.; Proust, J.; Movsesyan, A.; Béal, J.; Baudrion, A. -L.; Adam, P. -M.; Chehaidar, A.; Plain, J. Large-Scale and Low-Cost Fabrication of Silicon Mie Resonators. *ACS Nano* **2019**, *13*, 4199−4208.

57. Tilley, R. D.; Warner, J. H.; Yamamoto, K.; Matsuib, I.; Fujimoric, H. Micro-emulsion Synthesis of Monodisperse Surface Stabilized Silicon Nanocrystals. *Chem. Commun*. **2005**, 1833−1835.

58. Shiohara, A.; Prabakar, S.; Faramus, A.; Hsu, C. -Y.; Lai, P. -S.; Northcotea, P. T.; Tilley, R. D. Sized controlled synthesis, purification, and cell studies with silicon quantum dots. *Nanoscale* **2011**, *3*, 3364–3370.

59. Baldwin, R. K.; Pettigrew, K. A.; Ratai, E.; Augustine, M. P.; Kauzlarich, S. M. Solution reduction synthesis of surface stabilized silicon nanoparticles. *Chem. Commun*. **2002**, 1822–1823.

60. Zou, J.; Sanelle, P.; Pettigrew, K. A.; Kauzlarich, S. M. Size and Spectroscopy of Silicon Nanoparticles Prepared via Reduction of $SiCl_4$. *J. Cluster Sci*. **2006**, *17*, 565–578.

61. Yang, C. -S.; Bley, R. A.; Kauzlarich, S. M.; H. Lee, H. W. H.; Delgado, G. R. Synthesis of Alkyl-Terminated Silicon Nanoclusters by a Solution Route. *J. Am. Chem. Soc*. **1999**, *121*, 5191–5195.

62. Dasog, M.; Yang, Z.; Regli, S.; Atkins, T. M.; Faramus, A.; Singh, M. P.; Muthuswamy, E.; Kauzlarich, S. M.; Tilley, R. D.; Veinot, J. G. C. Chemical Insight into the Origin of Red and Blue Photoluminescence Arising from Freestanding Silicon Nanocrystals. *ACS Nano* **2013***, 7*, 2676-2685.

63. Semlali, S.; Cormary, B.; De Marco, M. L.; Majimel, J.; Saquet, A.; Coppel, Y.; Gonidec, M.; Rosa, P.; Drisko, G. L. Effect of Solvent on Silicon Nanoparticle Formation and Size: A Mechanistic Study. *Nanoscale* **2019**, *11*, 4696–4700

64. Dasog, M.; Yang, Z.; Veinot, J. G. C. Size-controlled solid state synthesis of luminescent silicon nanocrystals using Stober silica particles. *CrystEngComm*. **2012**, *14*, 7576–7578.

65. Murthy, T. U. M. S.; Miyamoto, N.; Shimbo, M.; Nishizawa, J. Gas-phase nucleation during the thermal decomposition of silane in hydrogen. *J. Cryst. Growth* **1976**, *33*, 1–7.

66. Kakati, M.; Das, A. K. Chapter 1 – Thermal Plasma Assisted Techniques for Synthesis of High Temperature Meteraial Nanoparticles. In *New Nanotechniques*; Malik, A.; Rawat, R. J., Ed.; Nova Science Publishers: New York, 2009; pp 1–20.

67. Slootman, F.; Parent, J. -C. Homogeneous gas-phase nucleation in silane pyrolysis. *J. Aerosol Sci*. **1994**, 25, 15–21.

68. Littau, K. A.; Szajowski, P. J.; Muller, A. J.; Kortan, A. R.; Bins, L. E. A Luminescent Silicon Nanocrystal Colloid via a High-Temperature Aerosol Reaction. *J. Phys. Chem*. **1993**, *97*, 1224–1230.

69. Onischuk, A. A.; Strunin, V. P.; Ushakova, M. A.; Panfilov, V. N. On the pathways of aerosol formation by thermal decomposition of silane. *J. Aerosol Sci*. **1997**, *28*, 207–222.
70. Zhang, P.; Duan, J.; Chen, G.; Li, J.; Wang, W. Production of polycrystalline silicon from silane pyrolysis: A review of fines formation. *Sol. Energy* **2018**, *175*, 44–53.
71. Girshick, S. L.; Swihart, M. T.; Suh, S.-M.; Mahajan, M. R.; Nijhawan, S. Numerical Modeling of Gas-Phase Nucleation and Particle Growth during Chemical Vapor Deposition of Silicon. *J. Electrochem. Soc.* **2000**, *147*, 2303–2311.
72. Vazquez-Pufleau, M.; Wang, Y.; Biswas, P.; Thimsen, E. Measurement of sub-2 nm stable clusters during silane pyrolysis in a furnace aerosol reactor. *J. Chem. Phys*. **2020**, *152*, 024304.
73. Li, X.; He, Y.; Talukdar, S. S.; Swihart, M. T. Process for Preparing Macroscopic Quantities of Brightly Photoluminescent Silicon Nanoparticles with Emission Spanning the Visible Spectrum. *Langmuir* **2003**, *19*, 8490–8496.
74. Li, X.; He, Y.; Swihart, M. T. Surface Functionalization of Silicon Nanoparticles Produced by Laser-Driven Pyrolysis of Silane followed by HF–HNO_3 Etching. *Langmuir* **2004**, *20*, 4720–4727.
75. Hua, F.; Swihart, M. T.; Ruckenstein, E. Efficient Surface Grafting of Luminescent Silicon Quantum Dots by Photoinitiated Hydrosilylation. *Langmuir* **2005**, *21*, 6054–6062.
76. Pell, L. E.; Schricker, A. D.; Mikulec, F. V.; Korgel, B. A. Synthesis of Amorphous Silicon Colloids by Trisilane Thermolysis in High Temperature Supercritical Solvents. *Langmuir* **2004**, *20*, 6546–6548.
77. Harris, J. T.; Hueso, J. L.; Korgel, B. A. Hydrogenated Amorphous Silicon (a-Si:H) Colloids. *Chem. Mater*. **2010**, *22*, 6378–6383.
78. Shi, L.; Harris, J.; Fenollosa, R.; Rodriguez, I.; Lu, X.; Korgel, B. A.; Meseguer, F. Monodisperse silicon nanocavities and photonic crystals with magnetic response in the optical region. *Nat. Commun*. **2013**, *4*, 1904.
79. De Marco, M. L.; Jiang, T.; Fang, J.; Lacomme, S.; Zheng, Y.; Baron, A.; Korgel, B. A.; Barois, P.; Drisko, G. L.; Aymonier, C. Broadband Forward Light Scattering by Architectural Design of Core–Shell Silicon Particles. *Adv. Funct. Mater*. **2021**, *31*, 2100915.

80. Holmes, J. D.; Ziegler, K. J.; Doty, R. C.; Pell, L. E.; Johnston, K. P.; Korgel, B. A. Highly Luminescent Silicon Nanocrystals with Discrete Optical Transitions. *J. Am. Chem. Soc*. **2001**, *123*, 3743–3748.

81. Heath, J. R. A Liquid-Solution-Phase Synthesis of Crystalline Silicon. *Science* **1992**, *258*, 1131–1133.

82. Kortshagen, U. R.; Sankaran, R. M.; Pereira, R. N.; Girshick, S. L.; Wu, J. J.; Aydil, E. S. Nonthermal Plasma Synthesis of Nanocrystals: Fundamental Principles, Materials, and Applications. *Chem. Rev.* **2016**, *116*, 11061–11127.

83. Bhandarkar, U. V.; Swihart, M. T.; Girshick, S. L.; Kortshagen, U. R. Modelling of silicon hydride clustering in a low-pressure silane plasma. *J. Phys. D: Appl. Phys.* **2000**, *33*, 2731–2746.

84. Loh, K. Q. Andaraarachchi, H. P.; Ferry, V. E.; Kortshagen, U. R. Photoluminescent Si/SiO_2 Core/Shell Quantum Dots Prepared by High-Pressure Water Vapor Annealing for Solar Concentrators, Light-Emitting Devices, and Bioimaging. *ACS Appl. Nano Mater.* **2023**, *6*, 6444−6453.

85. Li, Z.; Kortshagen, U. R. Aerosol-Phase Synthesis and Processing of Luminescent Silicon Nanocrystals. *Chem. Mater.* **2019**, *31*, 8451−8458.

86. Eslamisaray, M. A.; Wray, P. R.; Lee, Y.; Nelson, G. M.; Ilic, O.; Atwater, H. A.; Kortshagen, U. R. A Single-Step Bottom-up Approach for Synthesis of Highly Uniform Mie-Resonant Crystalline Semiconductor Particles at Visible Wavelengths. *Nano Lett.* **2023**, *23*, 1930−1937.

87. Guruvenket, S.; Hoey, J. M.; Anderson, K. J.; Frohlich, M. T.; Krishnan, R.; Sivaguru, J.; Sibi, M. P.; Boudjouk, P. Synthesis of Silicon Quantum Dots Using Cyclohexasilane (Si_6H_{12}). *J. Mater. Chem. C* **2016**, *4*, 8206–8213.

88. Yasar-Inceoglu, O.; Lopez, T.; Farshihagro, E.; Mangolini, L. Silicon Nanocrystal Production through Non-Thermal Plasma Synthesis: A Comparative Study between Silicon Tetrachloride and Silane Precursors, *Nanotechnology* **2012**, 23, 255604.

89. Kelly, J. A.; Henderson, E. J.; Veinot, J. G. C. Sol–gel precursors for group 14 nanocrystals. *Chem. Commun*. **2010**, *46*, 8704–8718.

90. Meldrum, A. Hryciw, A.; MacDonald, A. N.; Blois, C.; Marsh, K.; Wang, J.; Li, Q. Photoluminescence in the silicon-oxygen system. *J. Vac. Sci. Technol., A* **2006**, *24*, 713–717.

91. Ma, Z.; Liao, X.; He, J.; Cheng, W.; Yue, G.; Wang, Y.; Kong, G. Annealing behaviors of photoluminescence from SiO_x : H. *J. Appl. Phys.* **1998**, *83*, 7934–7939.

92. Sorarù, G. D.; Modena, S.; Bettotti, P.; Das, G.; Mariotto, G.; Pavesi, L. Si Nanocrystals Obtained Through Polymer Pyrolysis. *Appl. Phys. Lett.* **2003**, *83*, 749–751.

93. Hessel, C. M.; Henderson, E. J.; Veinot, J. G. C. Hydrogen Silsesquioxane: A Molecular Precursor for Nanocrystalline Si-SiO2 Composites and Freestanding Hydride Surface Terminated Silicon Nanoparticles. *Chem. Mat.* **2006**, 18, 6139–6146.

94. Shimizu-Iwayama, T.; Ohshima, M.; Niimi, T.; Nakao, S.; Kazuo, S.; Fujita, T.; Itoh, N. Visible Photoluminescence Related to Si Precipitates in Si^+-Implanted SiO_2. *J. Phys.: Condens. Matter* **1993**, *5*, L375–L380.

95. Withrow, S. P.; White, C. W.; Meldrum, A.; Budai, J. D.; Hembree, D. M.; Barbour, J. C. Effects of Hydrogen in the Annealing Environment on Photoluminescence from Si Nanoparticles in SiO_2. *J. Appl. Phys.* **1999**, *86*, 396–401.

96. Meldrum, A.; Haglund, R. F. Jr.; Boatner, L. A.; White, C. W. Nanocomposite Materials Formed by Ion Implantation. *Adv. Mater.* **2001**, *13*, 1431–1444.

97. Zhang, M.; Poumirol, J. -M.; Chery, N.; Majorel, C.; Demoulin, R.; Talbot, E.; Rinnert, H.; Girard, C.; Cristiano, F.; Wiecha, P. R.; Hungria, T.; Paillard, V.; Arbouet, A.; Pécassou, B.; Gourbilleau, F.; Bonafos, C. Infrared Nanoplasmonic Properties of Hyperdoped Embedded Si Nanocrystals in the Few Electrons Regime. *Nanophotonics* **2022**, *11*, 3485–3493.

98. Rimini, E. *Ion Implantation: Basics to Device Fabrication*; The Springer International Series in Engineering and Computer Science; Springer US: Boston, 1995.

99. Behrisch, R., Eckstein, W. *Sputtering by Particle Bombardment: Experiments and Computer Calculations from Theshold to MeV Energies*; Behrisch, R., Eckstein, W., Eds.; Topics in Applied Physics 110; Springer: Berlin, 2007.

100. Hayashi, S.; T. Nagareda; Yuchi Kanzawa; Yamamoto, K. Photoluminescence of Si-Rich SiO_2 Films: Si Clusters as Luminescent Centers. *Jpn. J. Appl. Phys.* **1993**, *32*, 3840–3840.

101. Bera, S.; Chaudhuri, S.; Bandyopadhyay, A. K.; Chakraborty, B.; Pal, A. K. Quantum Size Effect in Silicon Nanocrystals Prepared by Dc Magnetron Sputtering. *J. Phys. D: Appl. Phys.* **2001**, *34*, 273–278.

102. Iwamori, S.; Gotoh, Y.; Moorthi, K. Silicon Oxide Gas Barrier Films Deposited by Reactive Sputtering. *Surf. Coat. Technol.* **2003**, *166*, 24–30.

103. Mamiya, M.; Takei, H.; Kikuchi, M.; Uyeda, C. Preparation of Fine Silicon Particles from Amorphous Silicon Monoxide by the Disproportionation Reaction. *J. Cryst. Growth* **2001**, *229*, 457–461.

104. Sun, W.; Qian, C.; Cui, X. S.; Wang, L.; Wei, M.; Casillas, G.; Helmy, A. S.; Ozin, G. A. Silicon Monoxide – a Convenient Precursor for Large Scale Synthesis of near Infrared Emitting Monodisperse Silicon Nanocrystals. *Nanoscale* **2016**, *8*, 3678–3684.

105. Sugimoto, H.; Okazaki, T.; Fujii, M. Mie Resonator Color Inks of Monodispersed and Perfectly Spherical Crystalline Silicon Nanoparticles. *Adv. Opt. Mater.* **2020**, *8*, 2000033–2000033.

106. Kasai, H.; Sugimoto, H.; Fujii, M. Selective Enhancement of Crystal-Field-Split Narrow *F-F* Emission Lines of Europium Ions by Electric and Magnetic Purcell Effect of Mie Resonant Silicon Nanosphere. *Adv. Opt. Mater.* **2023**, 2301204.

107. Benyon, J. Silicon Monoxide: Fact or Fiction. *Vacuum* **1970**, *20*, 293–294.

108. J. Yasaitis; Kaplow, R. Structure of Amorphous Silicon Monoxide. *J. Appl. Phys.* **1972**, *43*, 995–1000.

109. Hohl, A.; Wieder, T.; van Aken, P. A.; Weirich, T. E.; Denninger, G.; Vidal, M.; Oswald, S.; Deneke, C.; Mayer, J.; Fuess, H. An Interface Clusters Mixture Model for the Structure of Amorphous Silicon Monoxide (SiO). *Non-Cryst. Solids* **2003**, *320*, 255–280.

110. Schulmeister, K.; Mader, W. TEM Investigation on the Structure of Amorphous Silicon Monoxide. *Non-Cryst. Solids* **2003**, *320*, 143–150.

111. Hirata, A.; Kohara, S.; Asada, T.; Arao, M.; Yogi, C.; Imai, H.; Tan, Y.; Fujita, T.; Chen, M. Atomic-Scale Disproportionation in Amorphous Silicon Monoxide. *Nat. Commun.* **2016**, *7*, 11591.

112. Tangstad, M. Chapter 6 - Ferrosilicon and Silicon Technology. In *Handbook of Ferroalloys: Theory and Technology*; Gasik, M., Ed.; Butterworth-Heinemann, 2013; pp 179–220.

113. Snyder, L. E.; Buhl, D. Detection of Possible Maser Emission near 3.48 Millimeters from an Unidentified Molecular Species in Orion. *Astrophys. J.* **1974**, *189*, L31–L33.

114. Yoon, D.-H.; Cho, S.-H.; Yun, Y.; Choi, Y. K.; Dodson, R.; Rioja, M.; Kim, J.; Imai, H.; Kim, D.; Yang, H.; Byun, D.-Y. Astrometrically Registered Maps of H_2O and SiO Masers toward VX Sagittarii. *Nat. Commun.* **2018**, *9*, 2534.

115. Kenyon, A. J.; P.F. Trwoga; Pitt, C.; Rehm, G. The Origin of Photoluminescence from Thin Films of Silicon-Rich Silica. *J. Appl. Phys.* **1996**, *79*, 9291–9300.

116. Ma, Z.; Liao, X.; He, J.; Cheng, W.; Yue, G.; Wang, Y.; Kong, G. Annealing Behaviors of Photoluminescence from SiOx:H. *J. Appl. Phys.* **1998**, *83*, 7934–7939.

117. Zacharias, M.; Heitmann, J.; Scholz, R.; Kahler, U.; Schmidt, M.; Bläsing, J. Size-Controlled Highly Luminescent Silicon Nanocrystals: A SiO/SiO2 Superlattice Approach. *Appl. Phys. Lett.* **2002**, *80*, 661–663.

118. Kickelbick, G. Silsesquioxanes. In *Functional Molecular Silicon Compounds I: Regular Oxidation States*. Scheschkewitz, D., Ed.; Structure and Bonding; Springer, 2014; Vol. 155, pp 1–28.

119. Frye, C. L.; Collins, W. T. The Oligomeric Silsesquioxanes, $(HSiO_{3/2})_n$. *J. Am. Chem. Soc.*, **1970**, *92*, 5586–5588.

120. Namatsu, H.; Yamaguchi, T.; Nagase, M.; Yamazaki, K.; Kurihara, K. Nano-Patterning of a Hydrogen Silsesquioxane Resist with Reduced Linewidth Fluctuations. *Microelectron. Eng.* **1998**, *41*, 331–334.

121. Grigorescu, A. E.; van der Krogt, M. C.; Hagen, C. W.; Kruit, P. 10 nm lines and spaces written in HSQ, using electron beam lithography. *Microelectron. Eng.* **2007**, *84*, 822– 824.

122. Baek, I.-B.; Yang, J.-H.; Cho, W.-J.; Ahn, C.-G.; Im, K.; Lee, S. Electron beam lithography patterning of sub-10nm line using hydrogen silsesquioxane for nanoscale device applications. *J. Vac. Sci. Technol., B* **2005**, *23*, 3120–3123.

123. Chen, H.; Tecklenburg, R. E. Characterization of Low and Intermediate Molecular Weight Hydrogen Silsesquioxanes by Mass Spectrometry. *J. Am. Soc. Mass Spectrom*. **2006**, *17*, 1438–1441.

124. Pauthe, M.; Bernstein, E.; Dumas, J,; Saviot, L.; Pradel, A.; Ribes, M. Preparation and characterisation of Si nanocrystallites embedded in a silica matrix. *J. Mater. Chem*. **1999**, *9*, 187–191.

125. Hessel, C. M.; Henderson, E. J.; Veinot, J. G. C. An Investigation of the Formation and Growth of Oxide Embedded Silicon Nanocrystals in Hydrogen Silsesquioxane Derived Nanocomposites. *J. Phys. Chem. C* **2007**, *111*, 6956–6961.

126. Yang, C.-C.; Chen, W.-C. The structures and properties of hydrogen silsesquioxane (HSQ) films produced by thermal curing. *J. Mater. Chem*. **2002**, *12*, 1138–1141.

127. Belot, V.; Corriu, R.; Leclercq, D.; Mutin, P. H.; Vioux, A. Thermal Reactivity of Hydrogenosilsesquioxane Gels. *Chem. Mater.* **1991**, *3*, 127–131.

128. Hessel, C. M.; Reid, D.; Panthani, M. G.; Rasch, M. R.; Goodfellow, B. W.; Wei, J. W.; Fujii, H.; Akhavan, V.; Korgel, B. A. Synthesis of Ligand-Stabilized Silicon Nanocrystals with Size-Dependent Photoluminescence Spanning Visible to Near-Infrared Wavelengths. *Chem. Mater.* **2012**, *24*, 393– 401.

129. Yang, Z.; Dobbie, A. R.; Cui, K.; Jonathan. A Convenient Method for Preparing Alkyl-Functionalized Silicon Nanocubes. *J. Am. Chem. Soc.* **2012**, *134*, 13958–13961.

130. Henderson, E. J.; Kelly, J. A.; Veinot, J. G. C. Influence of $HSiO_{1.5}$ Sol-Gel Polymer Structure and Composition on the Size and Luminescent Properties of Silicon Nanocrystals. *Chem. Mater*. **2009**, *21*, 5426–5434.

131. Henderson, E. J.; Veinot, J. G. C. From Phenylsiloxane Polymer Composition to Size-Controlled Silicon Carbide Nanocrystals. *J. Am. Chem. Soc*. **2009**, *131*, 809–815.

132. Dasog, M.; Rachinsky, C.; Veinot, J. G. C. From Si and C encapsulated SiO_2 to SiC: Exploring the influence of sol-gel polymer substitution on thermally induced nanocrystal formation. *J. Mater. Chem.* **2011**, *21*, 12422–12427.

133. Xin, Y.; Wakimoto, R.; Saitow, K. Synthesis of Size-controlled Luminescent Si Nanocrystals from $(HSiO_{1.5})_n$ Polymers. *Chem. Lett*. **2017**, *46*, 699−702.

134. Terada, S.; Xin, Y.; Saitow, K. Cost-Effective Synthesis of Silicon Quantum Dots. *Chem. Mater.* **2020**, *32*, 8382−8392.

135. Zhou, W. J.; Zheng, Y. X.; Zhang, C.; Ma, X. F.; Li, D. H.; Ma, L.; Hu, F.; Yang, S. D.; Yang, L.; Gao, M. Y.; Lu, M.; Zhang, R. J.; Wang, S. Y.; Chen, L. Y. Optical properties of high photoluminescence silicon nanocrystals embedded in SiO2 matrices obtained by annealing hydrogen silsesquioxane. *Opt. Mater.* **2018**, *84*, 874–878.

Chapter 2

High-Temperature (T > 1400°C) Annealing of HSQ and the Silicon Monoxide Problem*

Hydrogen silsesquioxane (HSQ) is known to disproportionate at elevated temperatures, resulting in nanoscale elemental silicon inclusions within a matrix of SiO_2. Previous investigations suggest a continuous and direct relationship in which particle size can be increased by increasing either the processing temperature or processing time. Recent attempts at synthesizing large particles (d > 100 nm) using temperatures above 1400°C and dwell times greater than 1 hour uncovered anomalies in both nanoparticle size and the composition of the resulting composite materials. Silicon nanoparticle (SiNP) growth occurs as predicted at temperatures up to 1400°C, but prolonged heating between 1500–1600°C results in SiO_2 being the sole product of the reaction, and no nanoparticles are recovered. The standard trends regarding particle formation, size, and relative SiNP:SiO_2 composition reemerge beyond this temperature region and are restored at 1700°C. In addition to quantifying the boundaries of this parameter space, our characterization of the resulting materials suggests that silicon monoxide formation, promoted through the crystallization of cristobalite SiO_2, is responsible for the strange behavior of HSQ at high temperatures.

** This Chapter has been adapted with permission from the following publications:*

O'Connor, K. M.; Rubletz, A.; Ni, C.; He, Y.; Butler, C.; Veinot, J. G. C. *Chem. Mater.* **2023**, *35*, 7967–7973.

O'Connor. K. M.; Rubletz, A.; Trach, J.; Butler, C.; Veinot, J. G. C. *Nanoscale Horiz.* **2023**, *8*, 892–899.

2.1 In pursuit of Large (d > 100 nm) Silicon Nanocrystals, Part I: The High-Temperature Anomaly in HSQ

2.1.1 Introduction

For more than three decades, the photoluminescent properties of nano-silicon have garnered academic and commercial interest.[1] The discovery of quantum confinement in a naturally abundant, biologically benign, and electrochemically stable material made nano-silicon a seemingly ideal candidate for optical, electronic, and biological applications.[2] Inherent to the tailorable photoluminescence of silicon quantum dots is the requirement for carrier confinement. To this end, studies on the preparation and functionalization of silicon nanoparticles (SiNPs) have focused mainly on *small* (3-9 nm) nanoparticles.[3]

Recently, developments in the field of metamaterials have identified crystalline SiNPs as an ideal material for electromagnetic wave manipulation across the visible and infrared spectrum.[4, 5] This light-matter interaction is different from that of photoluminescence. Rather than generating a photon through exciton recombination, the particles exhibit a scattering effect as incident electromagnetic radiation oscillates the charge carriers within the dielectric, re-emitting the wave. Under certain conditions, a size-dependent magnetic and electric dipole resonance (Mie resonance) will form within the SiNP, significantly enhancing the directional scattering response.[6] These materials have the potential to realize unique optical phenomena, such as perfect reflection, negative refractive index, magnetic mirrors, and Huygens metasurfaces.[7]

The important distinction between SiNPs used for photoluminescence and those used for Mie scattering is particle size. While quantum confinement necessitates *small* particles ($d \leq 9$ nm),

Mie scattering in the visible spectrum requires relatively *large* particles ($75 \leq d \leq 200$ nm).[7] The pursuit of this new size regime encouraged researchers to either adapt established methods or develop entirely new protocols for *large* SiNP synthesis. Examples of this span a variety of synthetic techniques, including reactions in the gas, supercritical, and solid phases. The Kortshagen group modified their nonthermal plasma synthesis by creating an electrostatic potential trap in the filamentary discharge region of their plasma reactor. This modification enhanced particle sintering and could produce SiNPs more than 200 nm in diameter.[8] De Marco *et al.* used a supercritical hexane-based synthesis with trisilane and bis(N,N′-diisopropylbutyl)dichlorosilane.[9] While this method does not produce crystalline silicon, it allows for a wide range in particle sizes. By adjusting the relative concentration of the molecular precursors, they could tune the average particle size of their amorphous SiNPs from 150 to 400 nm.[9] Similarly, amorphous particles have also been prepared by Saitow and coworkers via straightforward mechanical ball milling of silicon powder.[10, 11] Their recent work went on to combine the magnesiothermic reduction reaction with laser-induced melting to afford porous Si microparticles containing crystalline spheroids as large as 500 nm.[12] The Fujii Team produced SiNPs through a solid-state thermal disproportionation of commercial "silicon monoxide" ($SiO_{(s)}$). After subjecting $SiO_{(s)}$ to temperatures of 1350–1600°C, the resulting SiNPs were liberated from a SiO_2 matrix with HF etching.[13] These examples, while not exhaustive, showcase the range in approaches taken toward realizing spherical silicon nanoparticles in this new, larger size regime.

In 2006, the Veinot group developed a method for producing oxide-embedded SiNPs by thermal disproportionation of solid hydrogen silsesquioxane (HSQ).[14] Subsequent silicon nanoparticle research from our lab has focused on probing the internal nanoparticle structure or exploring new applications for SiNPs.[15–18] In both cases, *small* nanoparticles are typically targeted

to achieve particle photoluminescence. While previous work has reported a positive correlation between annealing temperature and particle size, these studies stopped short of the ideal Mie scattering size window for visible wavelengths.[19,20] In this work, we target *large* silicon nanocrystals (75–200 nm) and expand our understanding of high-temperature treatment of HSQ. The influence of reaction temperature (1400–1700°C) and time (1–10 h) is explored. Additionally, an anomalous region of reduced SiNP yield between 1500–1600°C is examined and discussed.

2.1.2 Results and Discussion

Silicon nanoparticle preparation from HSQ disproportionation is presented in Scheme 2-1. In a typical experiment, 2 g of solid, white HSQ is thermally treated in a tube furnace under flowing Ar. The product of this thermal treatment is a composite of SiNPs embedded in a matrix of silica ("the composite"). This material is then mechanically ground to a powder before chemical etching with a hydrofluoric acid mixture liberates the silicon particles.

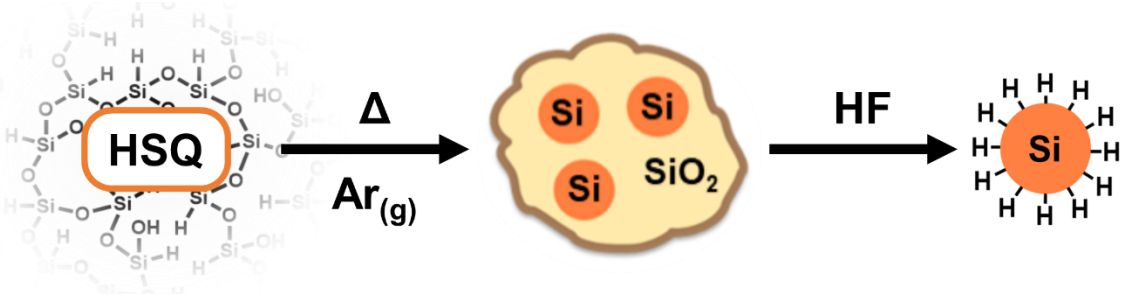

Scheme 2-1. Reaction scheme for hydride-terminated silicon nanoparticles prepared from hydrogen silsesquioxane (HSQ). Solid HSQ is an amorphous extended structure consisting of Si–H bonds decorating a polymeric network of Si–O bonds. Peak processing temperatures range between 1400–1700°C for reaction times of 1–10 h. Chemical etching is carried out in a solution of 1:1:1 ethanol, water, and HF (49 wt.%) before SiNPs are liquid-liquid extracted using toluene.

Our experiments include samples of HSQ heated to 1400, 1500, 1600, and 1700°C for 1, 2, 5, and 10 h. This array of reaction conditions was chosen to illuminate the SiNP size range accessible via HSQ disproportionation. Typically, the composite obtained from thermal treatment and grinding is a brown powder, indicative of the nanodomains of silicon trapped within it. To our surprise, some high-temperature reaction conditions produce powders that are grey or white. The visual appearance of these composites is illustrated in Figure 2-1.

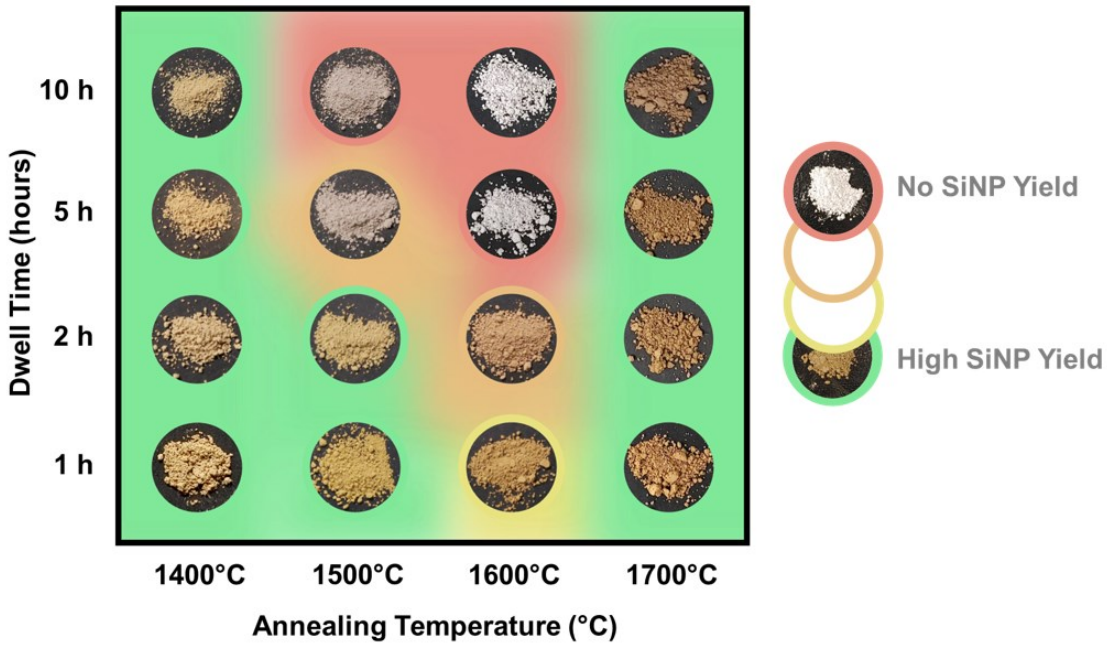

Figure 2-1. Qualitative colour map indicating the yield of silicon nanoparticle across an array of reaction conditions. Reaction temperature is given along the x-axis and reaction time (i.e., dwell time) is given along the y-axis. Photographs of the composite material are presented within circles. Surrounding the pictures is a colour guide denoting the relative SiNP quality and yield.

The gradient in product colour across the array of reaction conditions presents a perplexing circumstance. Following HSQ disproportionation at 1400°C, the composite is a brown powder. The onset of grey and white materials at 1500 and 1600°C, particularly for reactions times of 5 and 10 h (i.e., dwell times), suggests a deviation from the expected composition of the material. More surprisingly, this trend abruptly stops when HSQ is subject to 1700°C, and the resulting composite returns to a brown colour. Additionally, surrounding each picture is an approximate colour map reflecting the quality and yield of nanoparticles derived from the various composite materials after chemical etching. Green regions highlight reaction conditions that effectively produce SiNPs while red regions highlight reaction conditions from which no SiNPs are recovered. This figure will reappear throughout the text, acting as a visual guide as we examine the nature of the annealed composite materials across the array of reaction conditions.

To assess the oxidation states of Si present in the composites, X-ray photoelectron spectroscopy (XPS) is used (Figure 2-2). Following thermal treatment at 1400°C for 1 h, the XP spectrum of the composite is dominated by Si(IV), attributed to the silica oxide matrix, but also includes a distinct Si(0) emission originating from the SiNPs present within it. The spectra from composites heated at 1600°C for 1 and 2 h (Figure 2-2b, c) show a similar signature. At 1700°C for 10 h (Figure 2-2e), the intensity of the emission associated with elemental Si is noticeably higher, suggesting a greater amount of Si(0) is present in the sample. This finding is consistent with the observed growth of larger SiNPs at higher temperatures.[19, 20] The spectra of these samples (Figure 2-2a, b, c, e) is expected and indicates the composite comprise a mixture of SiO_2 and Si. This trend, however, deviates for composites prepared at 1600°C for 10 h (Figure 2-2d), where no Si(0) is observed.

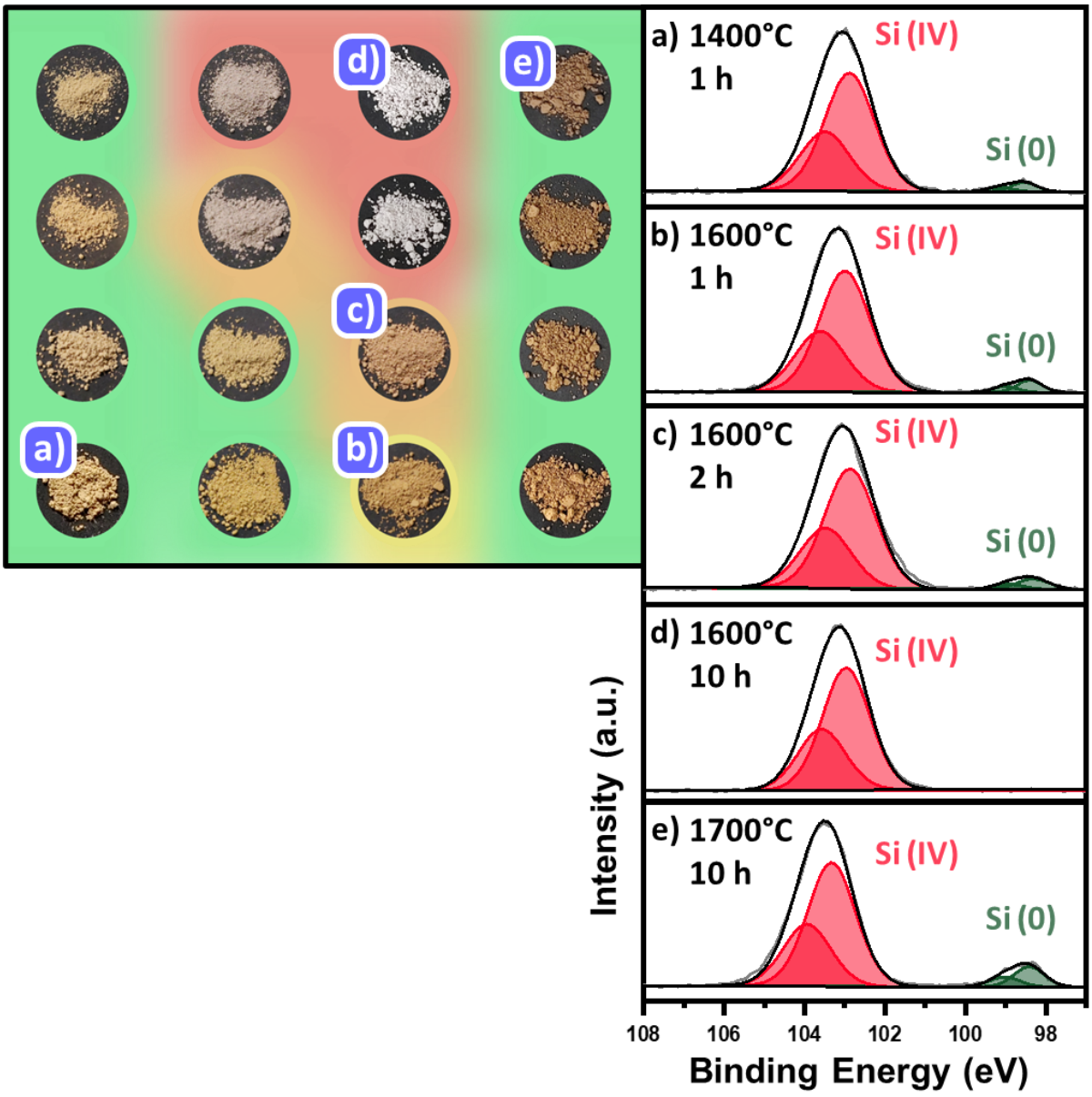

Figure 2-2. X-ray photoelectron spectral analysis of composites produced across a range of reaction conditions. The composites are ground into a powder before analysis to probe their interior more effectively. The figure left of the spectra (Figure 2-1) guides the reader through the dataset. Si peak fitting includes spin orbit splitting ($2p_{1/2}$, $2p_{3/2}$).

A more direct analysis of the SiNPs is accomplished by chemically etching the composite material with hydrofluoric acid. This process effectively removes the silicon dioxide and affords colloidal SiNPs. Imaging these nanoparticles with a transmission electron microscope (TEM) provides critical insight into the morphology of the nano-silicon domains. Seen in Figure 2-3, HSQ treated at 1400, 1500, and 1700°C for 1 h (Figure 2-3a, b, d) generates isolated, spherical nanoparticles. The average diameter of these particles increases with peak processing temperature (1400°C: 13 ± 3 nm, 1500°C: 42 ± 9 nm, 1700°C: 135 ± 42 nm). An anomaly in this trend occurs at 1600°C where SiNPs are much smaller than expected (13 ± 3 nm) and sometimes misshapen or conjoined (Figure 2-3c). Composite materials produced using extended dwell times at 1500 and 1600°C demonstrate a complete breakdown of nanoparticle morphology (Figure 2-3e, f). Conversely, the thermal treatment of HSQ using longer dwell times at 1400°C and 1700°C retained SiNP morphology, with longer dwell times resulting in larger nanoparticle diameters (Figure 2-4).

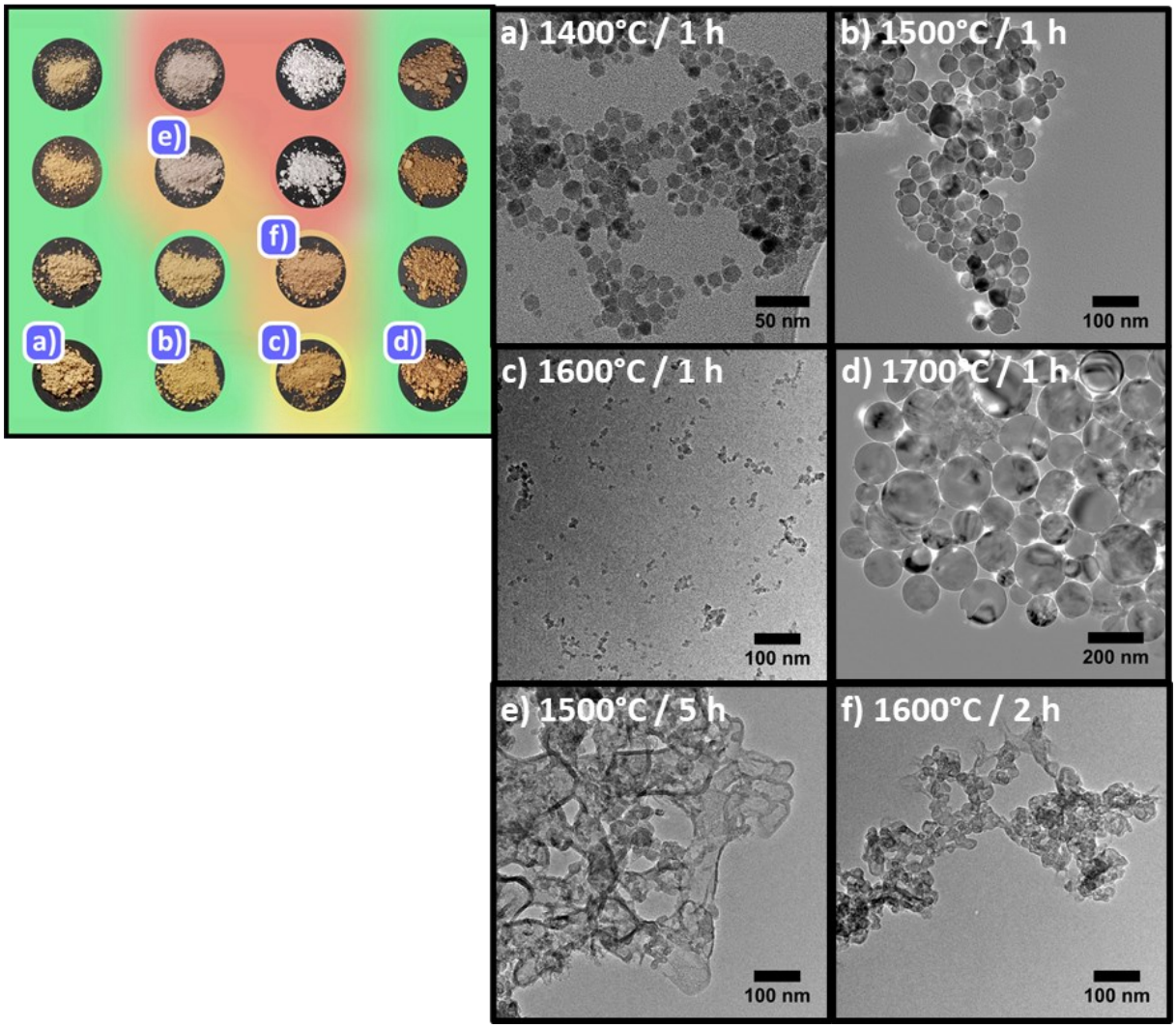

Figure 2-3. Bright field transmission electron microscopy of the silicon nanoparticles after chemical etching and liberation from the composite material. The figure left of the images (Figure 2-1) guides the reader through the dataset. Note: Scale bars are as indicated to ensure presentation of a suitable number of representative particles.

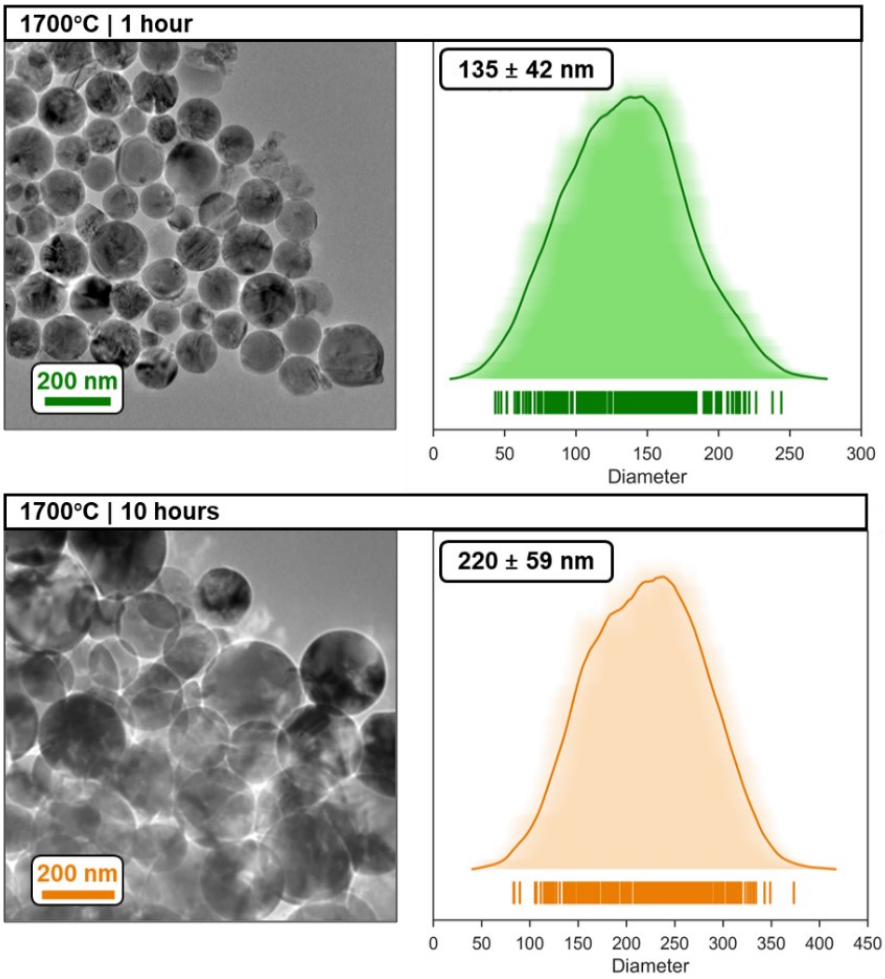

Figure 2-4. TEM images and average-shifted histogram for SiNPs made at 1700°C for 1 h (top) and 10 h (bottom).

The elemental analysis of isolated SiNPs is also possible using XPS. Like TEM preparation, these samples are made by chemically etching the composite material with HF and extracting the nanoparticles trapped within them. The XP spectrum indicates that the SiNPs comprise elemental silicon with some surface oxides and sub-oxides (Figure 2-5).

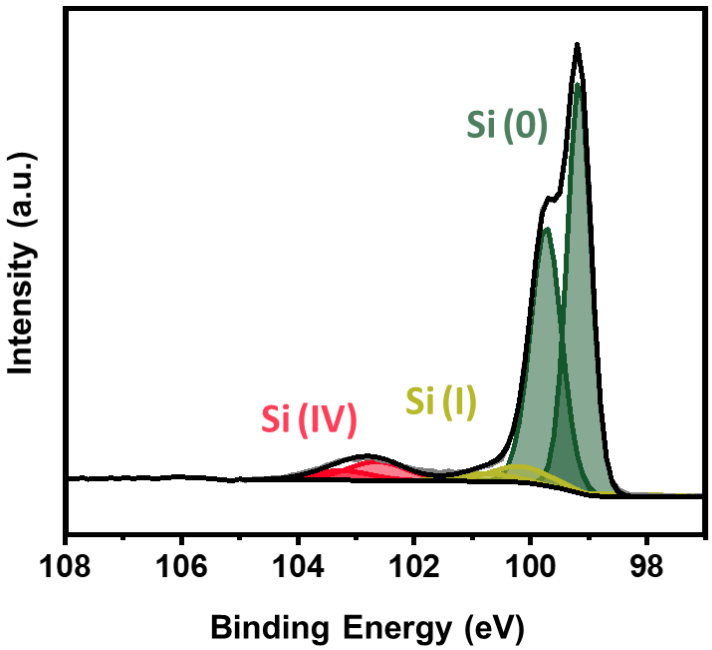

Figure 2-5. High-resolution Si X-ray photoelectron spectrum of liberated silicon nanoparticles after chemical etching with HF. Silicon nanoparticles were prepared at 1700°C for 10 h. Peak fitting includes spin orbit splitting ($2p_{1/2}$, $2p_{3/2}$).

Using powder X-ray diffraction (XRD) we can also analyze the evolving crystallinity within the composite materials across various reaction conditions. Thermal treatment of HSQ at 1400°C results in the characteristic pattern of crystalline nano-silicon (Figure 2-6a). Longer dwell times at this temperature narrow these peaks, consistent with growth of the crystalline domains and in agreement with electron microscopy observations (i.e., longer reaction times yield larger SiNPs).

The diffraction patterns for composites produced at 1500°C reveal the development of intense reflections characteristic of crystalline SiO_2 (Figure 2-6c). The features associated with this phase of crystalline silicon dioxide (cristobalite) are comparatively weak after 1 and 2 h reaction times but dominate the diffractogram after 5 or 10 h of heating. This observation suggests that a

lengthy incubation period is required before substantial crystallization of the SiO_2 matrix can occur. Similar to the trend observed at 1400°C, the silicon reflections become narrow with longer reaction times, however, these peaks also become less intense (Figure 2-6c insets). This loss in Si peak intensity is consistent with the XPS and suggests a decrease in overall Si(0) content. The trend observed at 1500°C is also seen in the series of diffraction patterns from composites prepared at 1600°C (Figure 2-6d). Again, the emergence of crystalline SiO_2 peaks at 1600°C coincides with the decrease and near total disappearance of the Si reflections.

The diffraction patterns of composites after thermal treatment at 1700°C resemble those at 1400°C. These conditions produce materials that exhibit the sharpest Si reflections, consistent with the observation of larger SiNPs in TEM.

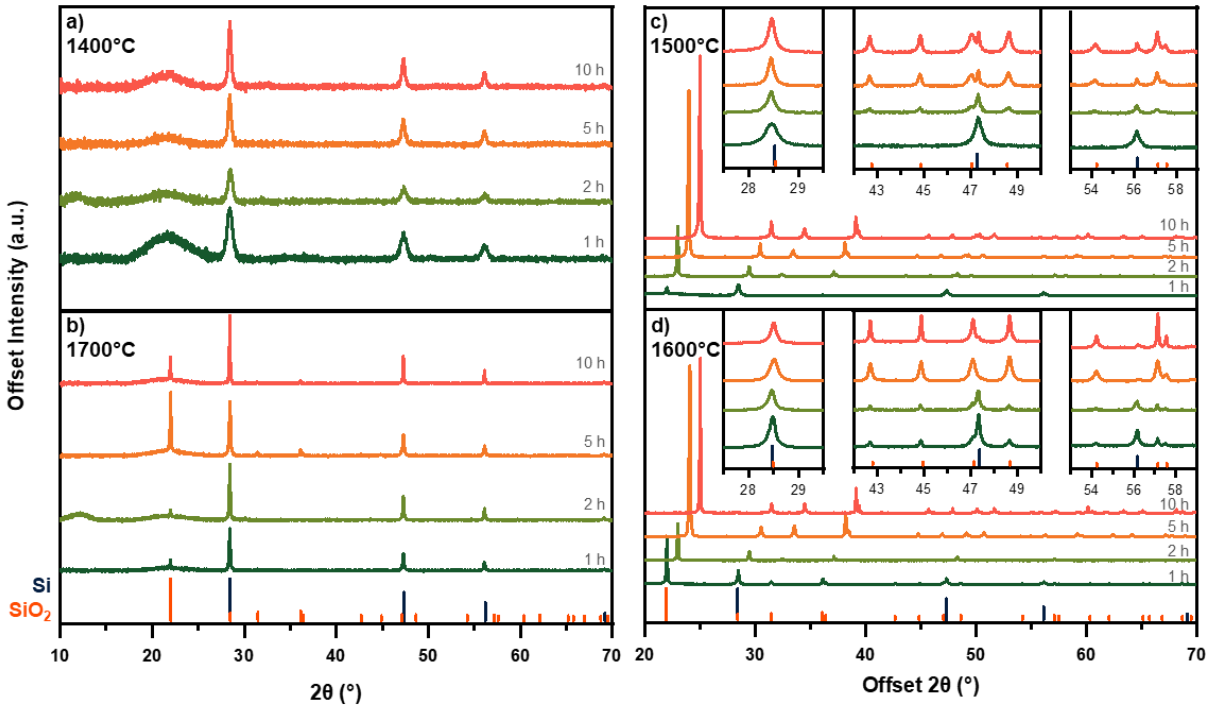

Figure 2-6. Powder X-ray diffraction (XRD) of composites after thermal treatment at indicated temperatures: (a) 1400°C, (b) 1700°C, (c) 1500°C, and (d) 1600°C. The diffraction patterns of composites produced using different dwell times (1, 2, 5, and 10 h) are presented as different colours. The expected reflections for crystalline Si and SiO_2 (cristobalite) are included below the patterns as blue and orange lines, respectively.[21, 22] Diffractograms c) and d) are offset and include insets to help illustrate the reflections.

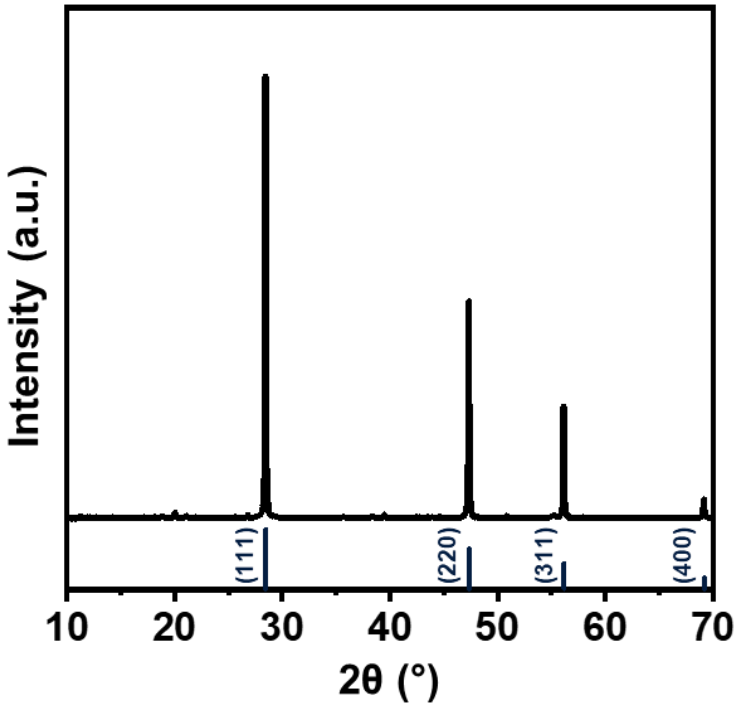

Figure 2-7. X-ray diffraction of liberated silicon nanoparticles after chemical etching with HF. Silicon nanoparticles were prepared at 1700°C for 10 h.

Additionally, we present the X-ray diffraction of isolated SiNPs in Figure 2-7. The strong reflections characteristic of crystalline silicon support our assertion that the large SiNPs prepared from high temperature annealing of HSQ are highly crystalline.

Despite our thorough characterization of the SiNP/SiO_2 composites and the free-standing silicon nanocrystals, the question remains: what is happening to the Si atoms between 1500–1600°C? The following section describes our investigation into the likely culprit.

2.2 Understanding Silicon Monoxide Evolution from Mixed Silicon and Silica Powders

While seeking an explanation for the mysterious disappearance of the silicon nanoparticles in HSQ, we noticed a lightweight, voluminous material had deposited along the walls and thermal insulation plugs of the alumina tube furnace. Imaging using a scanning electron microscope (SEM) revealed this material to be a collection of nanowires (Figure 2-8). Notably, the morphology and composition of these nanowires is remarkably similar to nanowires synthesized using silicon monoxide ($SiO_{(g)}$) deposition (Figure 2-8c).[23] These findings prompted an investigation into silicon monoxide.

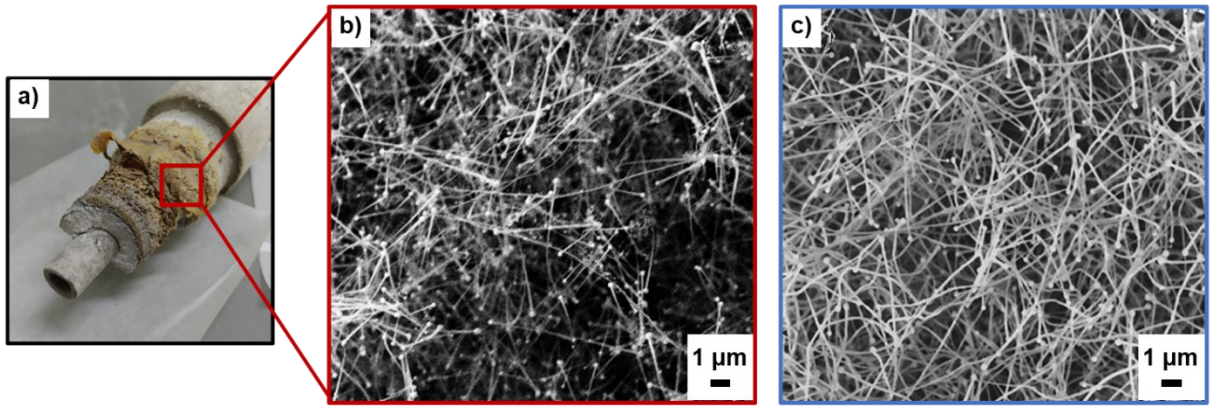

Figure 2-8. Nanowire deposition on tube furnace insulation. Picture of the furnace insulation plug with deposited material (a). SEM of the material (b), and SEM of Si-based nanowires adapted from *J. Phys. Chem. B* **2001**, *105*, 2507–2514 (Ref. 23).

2.2.1 Silicon Nanomaterials and Silicon/Silica Reactions

Silicon nanomaterials are routinely prepared via high-temperature processing of Si and SiO_2 mixtures obtained from sol-gel precursors (i.e., hydrogen silsesquioxane),[3, 17, 24, 25] commercial

sources (i.e., "SiO_X"),[3, 13, 26, 27] plasma-enhanced chemical vapor deposition,[28–30] and ion implantation.[31–33] Similar mixtures of Si and SiO_2 can also provide silicon monoxide gas (SiO) which is a prominent molecular precursor for silicon and silica nanowire synthesis.[34–37] As such, an understanding of the factors influencing the high temperature reaction between Si and SiO_2 as well as the corresponding SiO evolution is essential to the advancement of these attractive metal-free nanomaterials.

Early interest in SiO began with researchers pursuing an inorganic analogue of carbon monoxide. The direct reduction of SiO_2 with Si was first attempted by Winkler in 1890, however it was not successfully demonstrated until 1907 by Potter with the advent of new furnace technologies.[38–40] SiO gas is evolved in this way by heating mixtures of solid silicon and silica following reaction (1).

(1) $Si_{(s)} + SiO_{2\,(s)} \rightarrow 2\ SiO_{(g)}$

(2) $2\ \text{“}SiO_{(s)}\text{”} \rightarrow\ Si_{(s)} + SiO_{2\,(s)}$

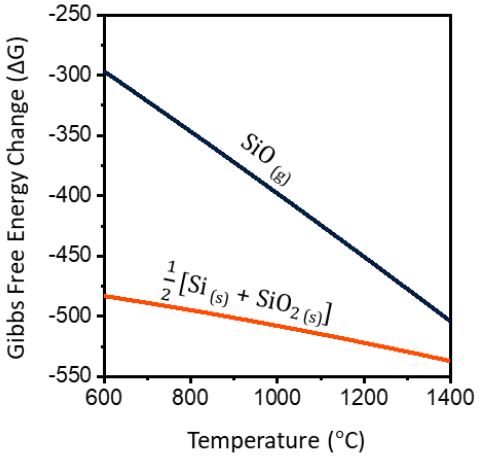

Figure 2-9. Reaction equations for the production (1) and decomposition (2) of silicon monoxide. Graph of the high-temperature Gibbs free energy change for reactions (1) and (2).[41, 42]

In his report, Potter describes SiO as an isolated solid. After subjecting silicon/silica mixtures to thermal treatment at ca. 1700°C, the resulting $SiO_{(g)}$ was cooled and deposited along

the furnace walls as a brown, voluminous powder.[40] When heated, the powder appeared to fully disproportionate to yield Si and SiO_2 (Equation 2).

The exact chemical composition of solid "silicon monoxide" has since been a subject of academic disagreement. While some claim $SiO_{(s)}$ can exist as a unique material, others argue its disproportionation is unavoidable.[43–47] Regardless, controlling the evolution of $SiO_{(g)}$ via reaction (1) has provided a reliable synthetic route to producing silicon nanowires.[34–37] In a typical experiment, authors flow inert gas over heated silicon/silica mixtures, carrying the resulting $SiO_{(g)}$ to cooler regions where it deposits into nanowire structures. While many of these studies focus on nanowire doping or mechanisms of nucleation and growth, the reaction conditions used to promote $SiO_{(g)}$ evolution differ significantly between publications and are seldom discussed.[34–37, 48–52] These differences include precursor composition (e.g., Si–SiO_2, SiC–SiO_2, "$SiO_{(s)}$ / SiO_X"), processing atmosphere (e.g., vacuum, reducing, inert), peak processing temperatures, and heating (i.e., dwell) times.

The Si–SiO_2 system and the interaction between Si, SiO, SiO_X and SiO_2 during thermal treatment has been investigated computationally and experimentally.[33, 53–56] Heating silica on silicon films under vacuum is known to remove large sections of SiO_2 from the Si surface. While the evolution of $SiO_{(g)}$ is ultimately responsible for this phenomenon, the role of oxygen vacancies and interstitials have been identified as mediators for SiO diffusion through the buried Si/SiO_2 interface.[33] Similarly, a SiO-mediated mechanism for Si atom transport during thermal disproportionation of SiO_X has been proposed computationally.[54] Interestingly, commercial solid "silicon monoxide" has seen use as a precursor material for $SiO_{(g)}$ evolution and silicon nanoparticle synthesis under comparable reaction conditions.[3, 13, 26, 27, 35–37] It is difficult to

reconcile the simultaneous growth of silicon nanodomains by "$SiO_{(s)}$" disproportionation and the reaction of silicon domains with the surrounding silica matrix.

Herein, we present a methodical study of the conditions necessary to drive reaction (1) by characterizing silicon/silica mixtures before and after thermal treatment. The effects of temperature, dwell time, and sample composition are examined.

2.2.2 Results and Discussion

Predefined mixtures of crystalline silicon and silica powder are loaded into a zirconia boat and subjected to thermal treatment in a standard tube furnace under flowing argon (Scheme 3-2).

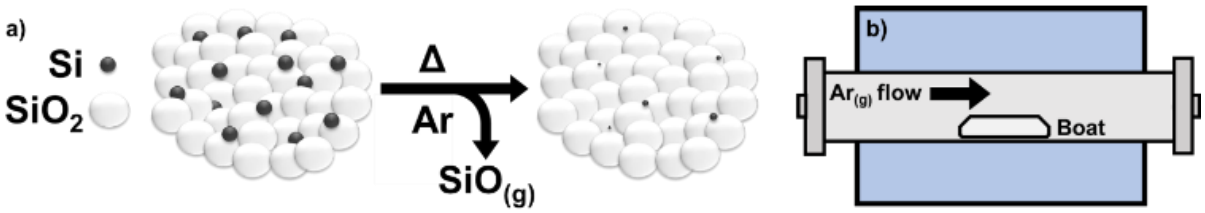

Scheme 2-2. A summary of the procedure used for silicon monoxide gas evolution from physically mixed Si and SiO_2 powders. (a) General illustration of the reaction; (b) tube furnace setup with sample boat.

After thermal processing, samples are cooled to room temperature, removed from the reaction tube, weighed, and mechanically ground to a uniform powder with a mortar and pestle for analyses using powder X-ray diffraction (XRD), X-ray photoelectron spectroscopy (XPS) and electron microscopy. Qualitative inspection reveals that, prior to heating, all Si/SiO_2 mixtures are free-flowing, uniform grey powders. Following thermal processing, the product powders vary from grey to white, depending upon the amount of elemental silicon remaining in the sample. As

Si(0) is consumed, the high SiO_2 band gap dominates the sample colour, resulting in a white powder.

To gain more detailed insight into the nature of these powers, we employed powder X-ray diffraction (XRD). It is a key analytical method for the present study because it provides a rapid and effective identification of the crystalline silica and silicon components. By comparing the intensity of cubic silicon reflections across diffraction patterns, it is possible to survey the loss of crystalline $Si_{(s)}$ under specific reaction conditions. These analyses are complemented by additional characterization techniques (*vide supra*) to circumvent the inherent limitations of XRD when probing amorphous and non-crystalline materials. While these characterization techniques only provide indirect evidence for silicon monoxide evolution, the deposition of silicon nanowires (Figure 2-10) on the cooler regions of the alumina furnace tube provide support for its production.

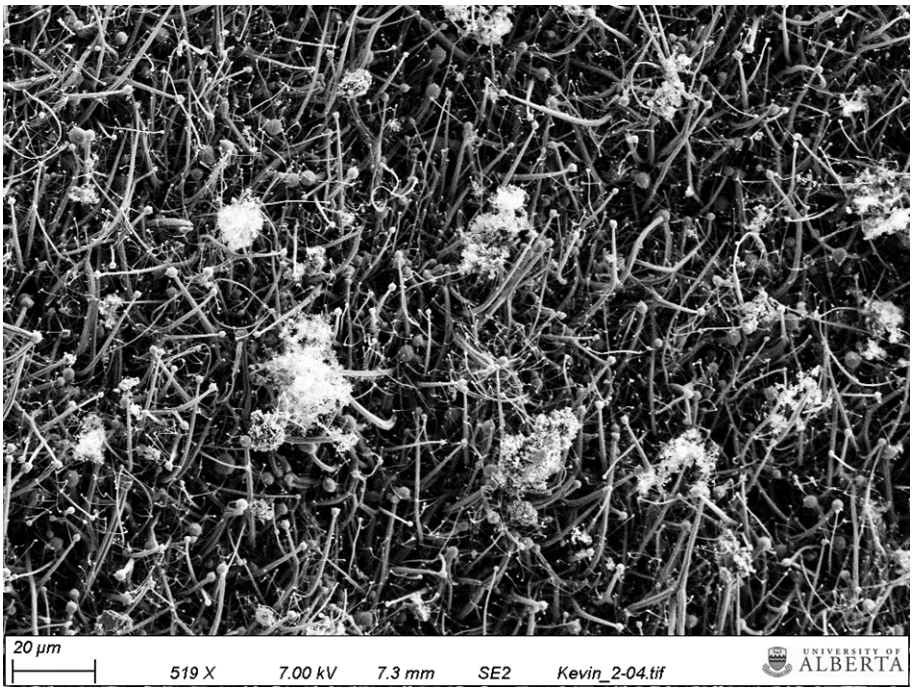

Figure 2-10. SEM of silicon nanowires produced by deposition of silicon monoxide gas.

Additionally, the evolution of $SiO_{(g)}$ from mixtures of Si and SiO_2 results in a decreased sample mass following thermal processing; in contrast, experiments in which $Si_{(s)}$ and $SiO_{2(s)}$ powders are heated independently yield no change in sample mass or crystallinity (Figure 2-11). Taken together, these results allow us to confidently assert that reaction (1) is responsible for loss of silicon from the reaction mixtures. The direct identification of SiO as the primary vaporizing species has also been previously achieved by heating similar Si/SiO_2 mixtures in a Knudsen cell and mass spectrometer assembly.[57]

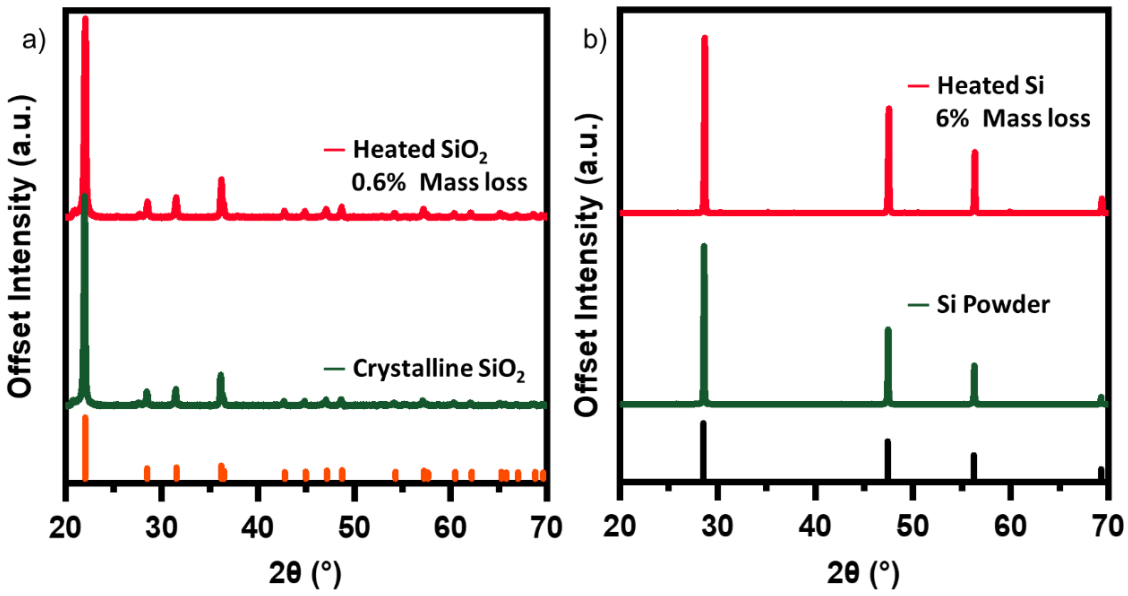

Figure 2-11. Mass loss and XRD of silica and silicon heated separately. (a) Bulk crystalline SiO_2 (cristobalite) heated independently (without silicon) to 1400°C for 5 h; (b) silicon powder heated independently (without silica) to 1300°C for 5 h. Literature reference peaks are given below the patterns for silicon[21] and cristobalite.[22]

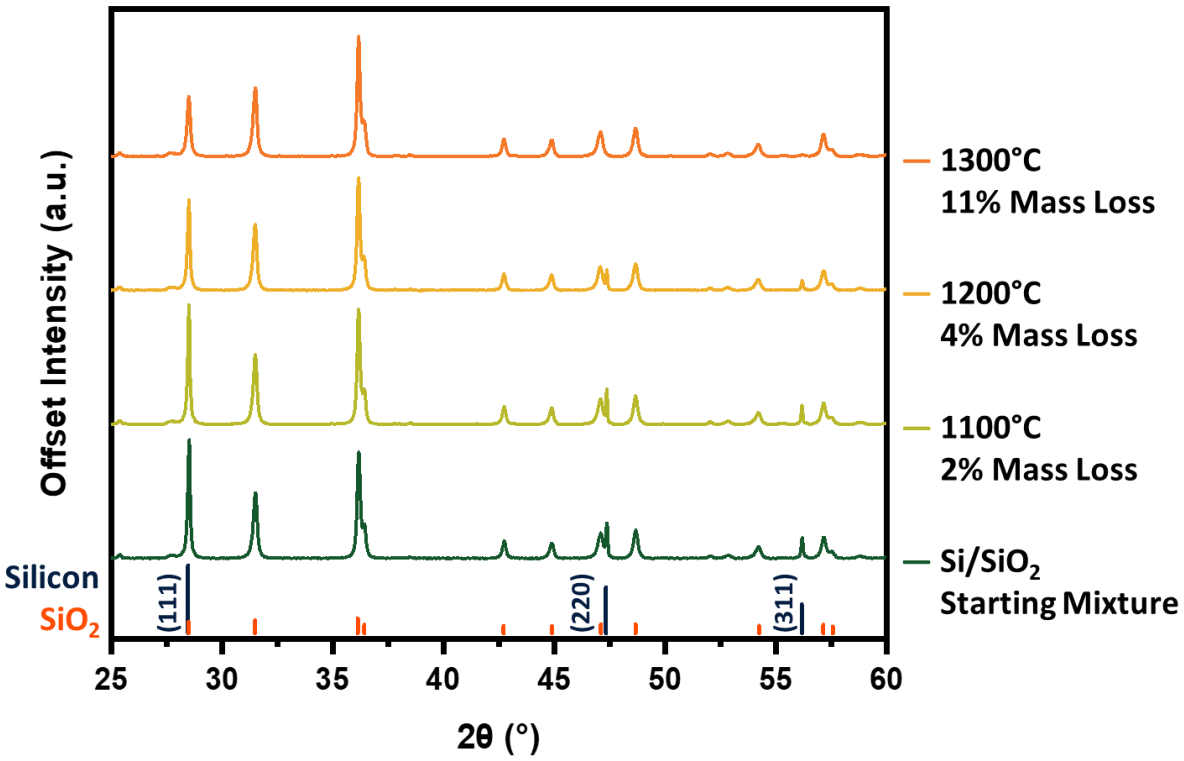

Figure 2-12. Powder X-ray diffraction of silica/silicon mixture before and after thermal treatment for 5 h under flowing argon. Literature reference peaks are given below the patterns for silicon[21] and cristobalite.[22]

Our investigation begins with identifying the thermal energy required to initiate this reaction. Unfortunately, the intense reflection at 28.5° is shared by silicon and crystalline silicon dioxide (cristobalite), making the peaks difficult to resolve and rendering it less diagnostic of reaction progress. Hence, we have chosen to compare the diffraction patterns of the Si/SiO_2 mixture before and after thermal treatment by focusing on the silicon 220 and 311 reflections at 47.3° and 56.2°, respectively (Figure 2-12). Heating at 1100°C produces no obvious change in the XRD pattern, however, increasing the processing temperature to 1200°C effects a significant decline in the intensity in all three silicon reflections. An additional increase in processing temperature to 1300°C sees the complete disappearance of all characteristic silicon reflections

from the pattern, suggesting reaction (1) has reached completion. The loss of silicon peaks is consistent with the noted decline in sample mass after thermal processing as well as in energy dispersive X-ray analysis and X- ray photoelectron spectroscopy (*vide infra*). At a SiO_2 to Si mass ratio of 20:1, the theoretical mass conversion/loss to $SiO_{(g)}$ is 15%. The 11% mass loss noted at 1300°C falls short of this mark and is reasonably attributed to some $SiO_{(g)}$ depositing onto the sample and sample boat as amorphous Si-based nanostructures (Figure 2-13), rather than being carried away by the flowing argon.

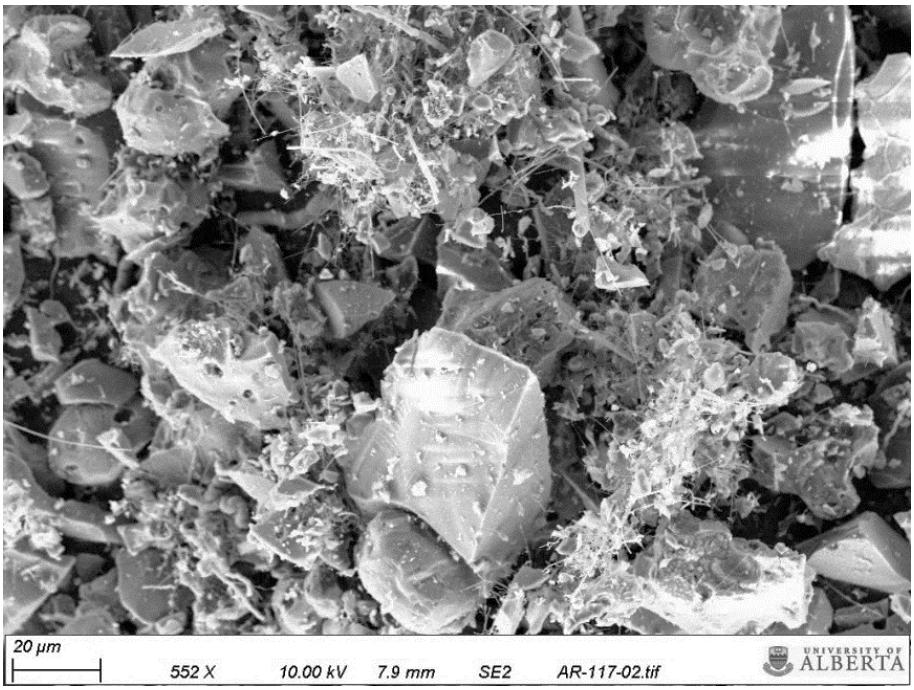

Figure 2-13. Nanowires and other Si-based nanostructures originating from SiO deposition decorate the silica/silicon mixtures after thermal treatment.

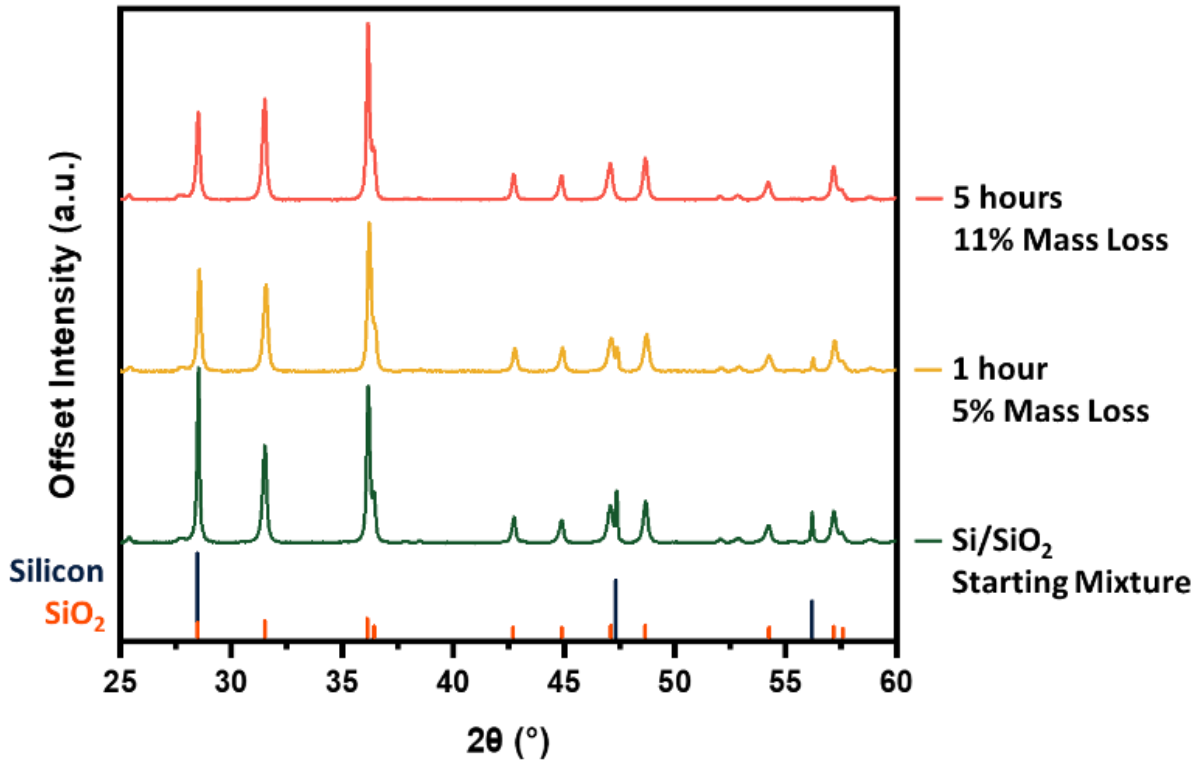

Figure 2-14. Powder X-ray diffraction investigating the impact of furnace dwell time on silicon monoxide evolution. Silicon/silica material before and after thermal treatment at a peak processing temperature of 1300°C for 1 (yellow) and 5 h (orange).

We now turn our attention to the influence of furnace dwell time (reaction time). Fixing the peak processing temperature at 1300°C, the products obtained from dwell times of 1 and 5 h were compared (Figure 2-14). Tracking the intensity of the silicon reflections, particularly those at 47.3° and 56.2°, demonstrates that prolonged exposure to appropriately high temperatures pushes the SiO-producing reaction toward completion. Again, the trend in sample mass loss aligns with additional $SiO_{(g)}$ leaving the sample boat during the longer dwell time.

To compliment XRD we employed electron microscopy to visualize the loss of silicon. Figure 2-15 shows scanning electron microscope (SEM) secondary electron (SE) images overlaid

with energy dispersive X-ray spectroscopy (EDX) colour mapping of silicon, oxygen, and carbon. Before heating we observe an abundance of silicon-rich regions (red) with dimensions of approximately 1-5 μm that we attribute to elemental silicon domains. These Si domains are dispersed throughout larger oxygen-rich fragments that we attribute to SiO_2 (Figure 2-15a). After heating at 1300°C in an inert argon atmosphere for 5 h, there is no evidence of the silicon-rich domains (Figure 2-15b). The absence of Si particles after thermal treatment agrees with our observation that reflections associated with crystalline silicon are absent from the XRD (Figure 2-12). Additional characterization of the oxidation states of silicon in the samples was performed with X-ray photoelectron spectroscopy (XPS). Again, the elemental silicon present in the sample before thermal treatment is absent afterwards (Figure 2-16).

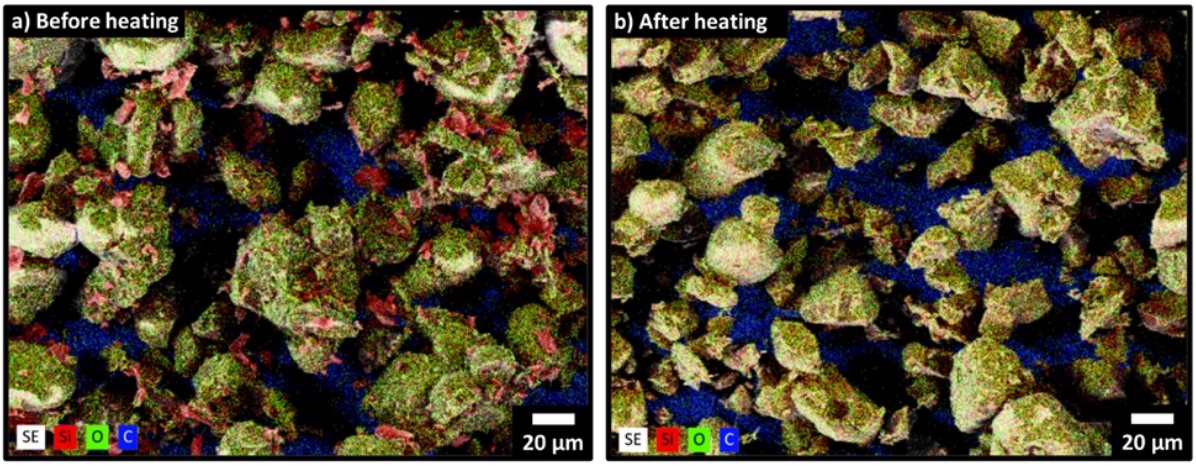

Figure 2-15. Secondary electron SEM images overlaid with EDX mapping of silicon (red), oxygen (green), and carbon (blue). (a) Silicon + silica mixtures before thermal treatment; (b) after thermal treatment at 1300°C for 5 hours.

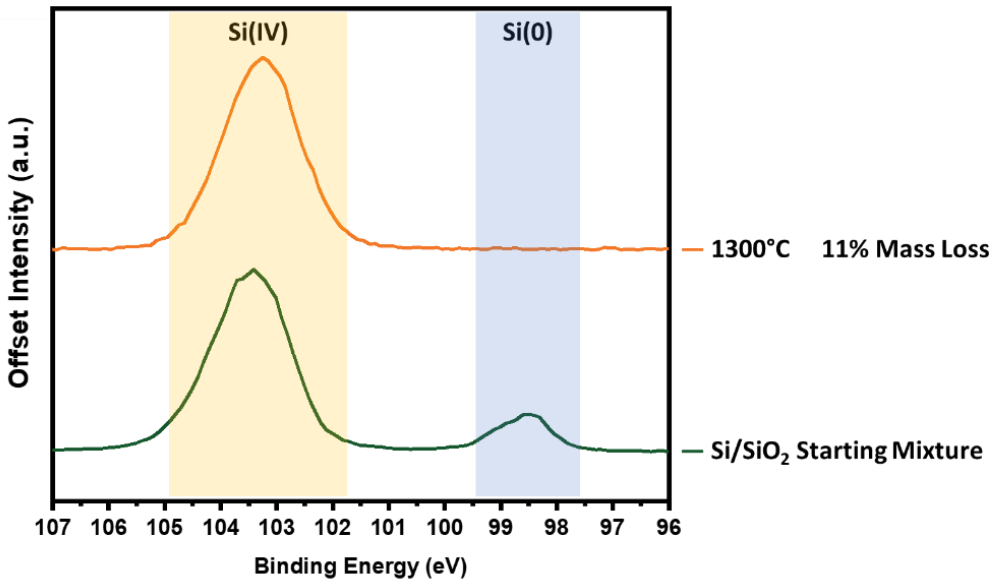

Figure 2-16. XPS of silicon/silica powder mixtures before and after heating.

The trend toward completion of reaction (1) with higher temperatures and longer reaction times is expected. While the formation of $SiO_{(g)}$ is entropically favorable (211.58 $J \cdot mol^{-1} \cdot K^{-1}$),[58] the strong Si–O bonds necessitate high reaction temperatures. Put simply, the greater number of Si–O bonds present in SiO_2 compared to SiO makes silicon monoxide evolution enthalpically unfavorable. In our study, evidence for Si transport by $SiO_{(g)}$ begins at 1200°C, and providing additional energy furthers SiO production by breaking more Si–O bonds. A more thorough discussion of the thermodynamics and partial pressure of $SiO_{(g)}$, including temperatures below 1200°C, are found in references 44, 45 and 59–62.

To allow straightforward comparisons of XRD patterns, reaction mixtures in Figure 2-12 and Figure 2-14 comprise crystalline SiO_2 and Si. Initial experiments using amorphous silica showed the emergence of overlapping peaks from crystalline SiO_2 at temperatures coinciding with the decrease in intensity of Si related features. This overlap made correlating changes in the XRD

pattern with reaction (1) progress challenging. To circumvent this interference, we chose to crystallize the SiO_2 before mixing with Si as this minimized any temperature-induced change in SiO_2 peak intensity and allows for a more direct analysis of the silicon 111, 220, and 311 reflections. We wondered then if the use of crystalline SiO_2 in our reaction mixtures influenced Si–SiO_2 reactivity. To investigate the role of crystallinity, we compared the reactivities of amorphous and crystalline SiO_2. Figure 2-17 shows that heating amorphous SiO_2 to 1200°C sees the appearance of a small peak corresponding to crystalline SiO_2 at 28.5°. Heating to 1300°C results in the appearance and increased intensity of peaks characteristic of crystalline SiO_2. Interestingly, it is only after the formation of crystalline SiO_2 that the intensity of the silicon reflections begins to decrease. We also note that the elimination of the silicon peaks requires temperatures 100°C higher than the corresponding samples prepared using crystalline SiO_2 (Figure 2-12). The crystalline and amorphous SiO_2 sources were imaged using SEM and no significant morphological differences are apparent (Figure 2-18c, d).

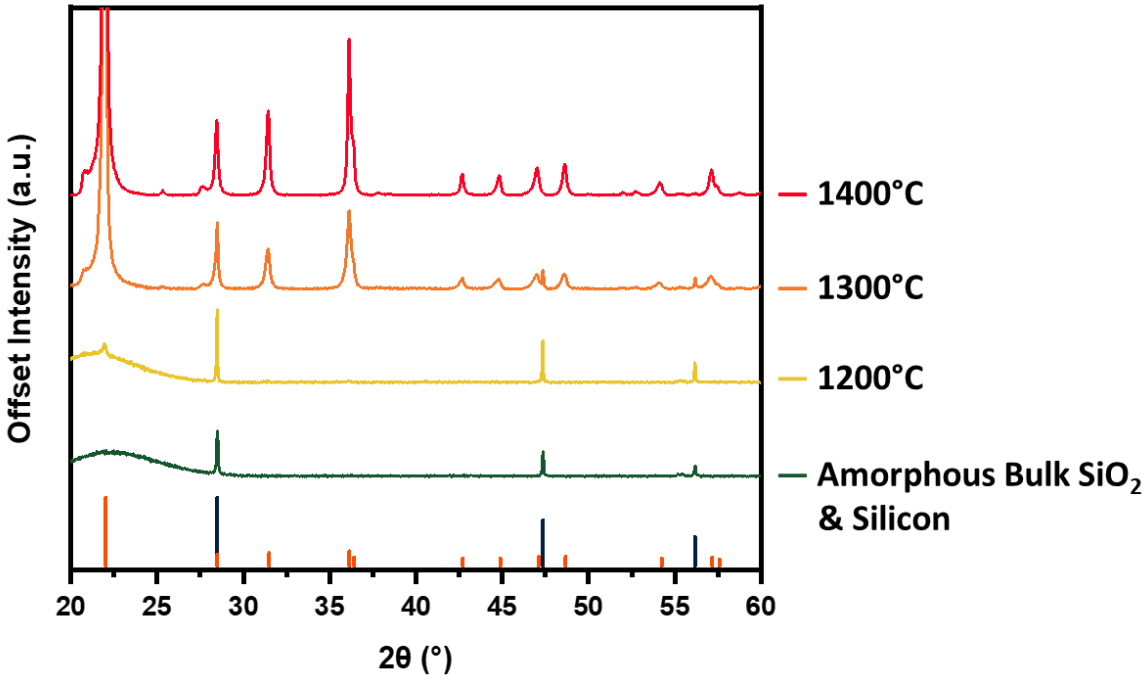

Figure 2-17. Powder X-ray diffraction investigating the effects of amorphous SiO_2 on the silicon monoxide reaction. All reactions are subject to a 5 h dwell time.

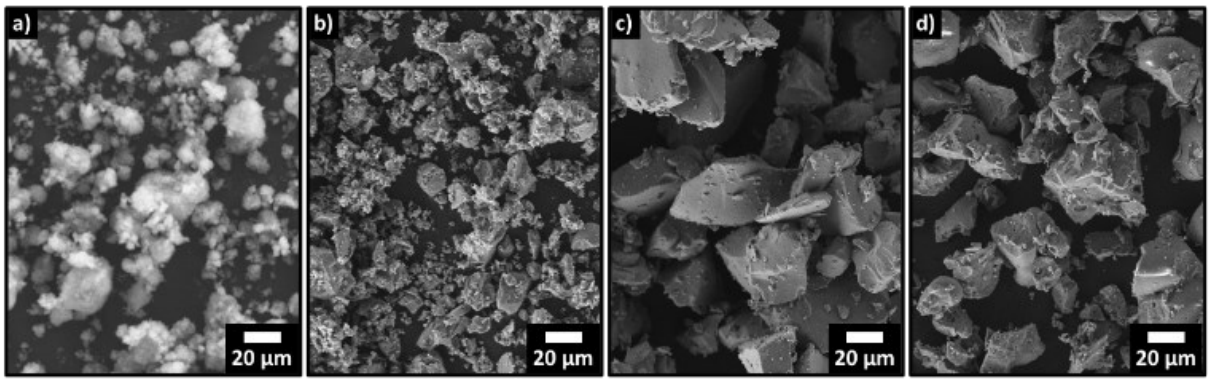

Figure 2-18. SEM images of various silica source material. (a) amorphous silica nanopowder; (b) silica nanopowder after crystallization; (c) amorphous bulk silica; (d) bulk silica after crystallization.

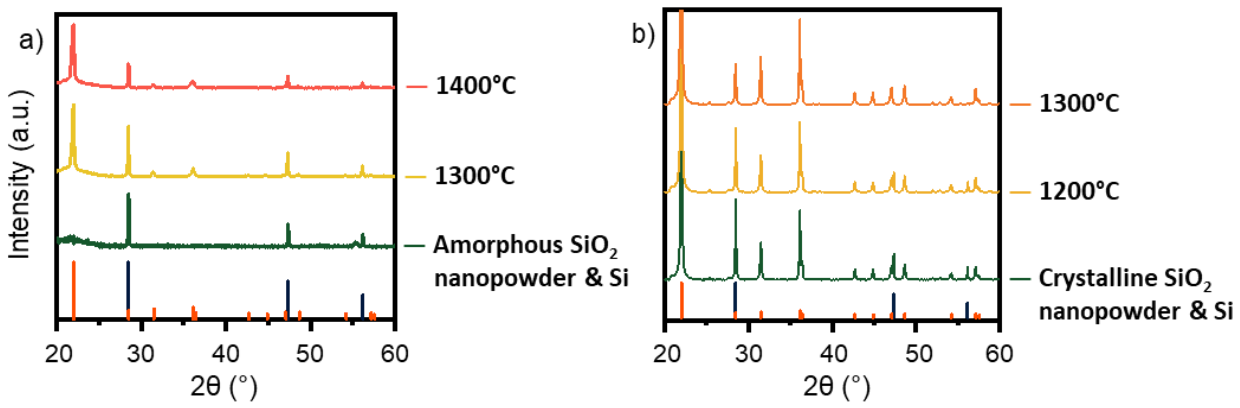

Figure 2-19. Powder X-ray diffraction pattern of silica/silicon mixtures after heating. Mixtures were prepared using amorphous SiO_2 nanopowder (a) and SiO_2 nanopowder that was crystallized before mixing with Si (b).

Additionally, we hypothesized that increasing the SiO_2 surface area available for reaction would promote $SiO_{(g)}$ evolution. To test this, we used a SiO_2 nanopowder (*d* ~5–10 nm) in the starting mixture. When amorphous nanopowder is used, no detectable reduction in the crystalline Si domains is observed until 1400°C (Figure 2-19a). This result is notable given the higher reactivity associated with powder edge sites and provides further support for the importance of crystalline SiO_2 domains to reaction (1). Crystallization of the nanopowder before introducing it to the reaction mixture resulted in reaction (1) proceeding (e.g., weight loss, evolution of XRD). This is demonstrated in Figure 2-19b which shows a complete elimination of silicon related peaks upon heating to 1300°C for reaction mixtures containing crystalline silica nanopowder. To our surprise, these results are nearly identical to the behavior of reaction mixtures containing bulk crystalline SiO_2 particles (Figure 2-12). One possible explanation for this similarity in reactivity is found in the electron microscopy and XRD of the crystallized nanopowder. When the voluminous, amorphous SiO_2 nanopowder is crystallized, its particle size increases dramatically to ~20 μm and the material becomes morphologically similar to bulk crystalline SiO_2 (Figure 2-

18). This particle growth is also reflected in the XRD analysis that shows narrow reflections indicative of bulk crystalline material. The repeated observation of disappearing Si reflections coinciding with the rise in SiO_2 reflections suggests that the presence of crystalline SiO_2 plays a critical role in reaction (1).

The reactants' surface area were also adjusted using Si/SiO_2 mixtures with relatively smaller silicon particles (< 100 nm). In this experiment, silicon nanoparticles were mixed with crystalline silica and subject to 1300°C for 1 hour (Figure 2-20). Unlike the relatively larger Si powder, which only partially converted into $SiO_{(g)}$ (Figure 2-12), these conditions fully consumed the silicon nanoparticles.

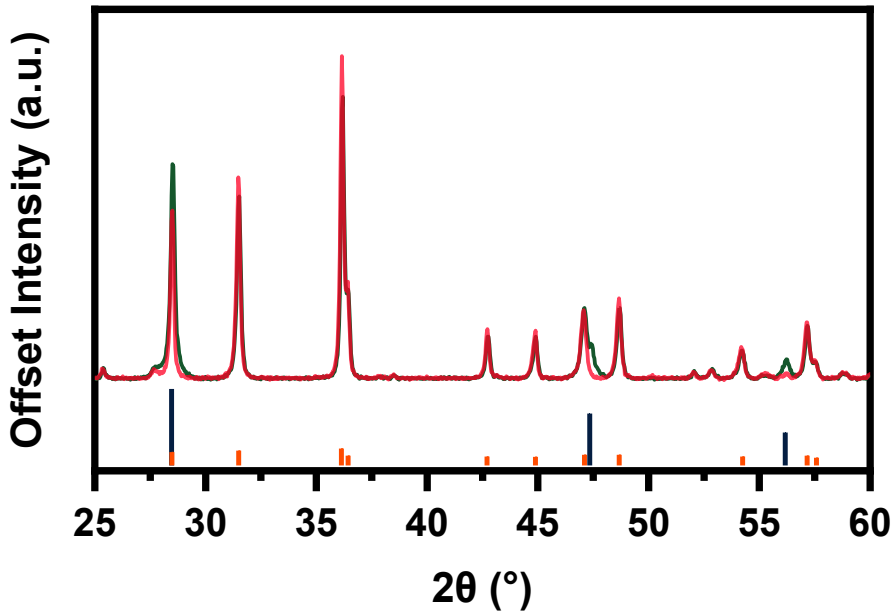

Figure 2-20. Overlaid powder XRD patterns for mixtures of silicon nanoparticles with crystalline SiO_2 (cristobalite) before (green) and after (red) heating at 1300°C for 1 hour. The diffraction peaks associated with Si and SiO_2 are presented below the patterns in blue and orange, respectively. After heating, the peak at 56.2° and the shoulder at 47.4° disappears, indicating a loss of crystalline Si. The peak at 28.5° also becomes less intense.

Defining the relative amounts of silicon and silica in the reaction mixture also impacts the nature of the resulting material obtained from thermal treatment. SiO_2 plays a unique role; it acts as both a reagent and diluent. At lower SiO_2:Si ratios, the temperatures required to promote reaction (1) induce sintering of the Si particles. This decreases the surface area and forms large silicon domains. The growing intensity of the silicon XRD peaks at temperatures below 1300°C suggests sintering is occurring for a SiO_2:Si mass ratio of 8:1 (Figure 2-21). Evidence for sintering is also observed in optical microscopy images where heating a SiO_2:Si mixture (mass ratio 4:1) to 1400°C produces necked bulbous particles of silicon metal (Figure 2-22). Increasing the temperature or extending dwell times cause reaction (1) to proceed, producing $SiO_{(g)}$ and overwhelming the influences of silicon particle sintering, thereby eliminating the crystalline Si peaks in the XRD (Figure 2-21, orange and red traces).

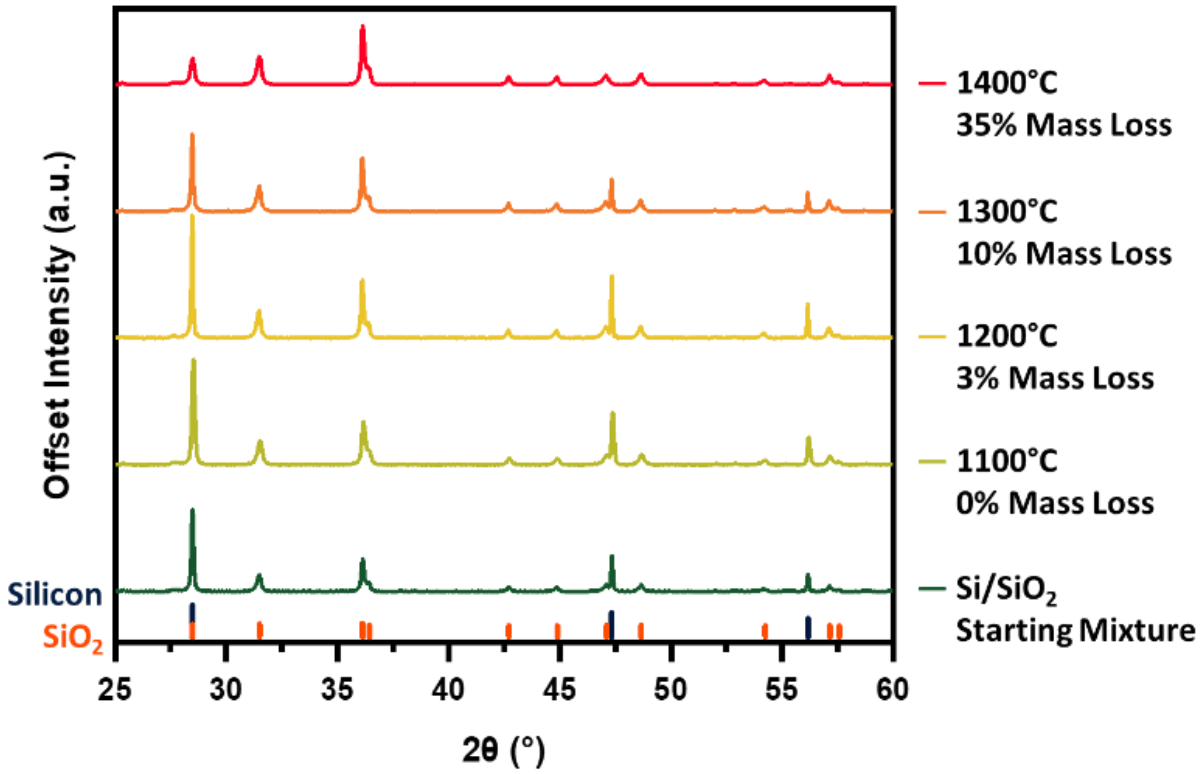

Figure 2-21. Powder X-ray diffraction patterns of a Si/SiO_2 mixture with a SiO_2:Si mass ratio 8:1 suggest sintering of silicon particles after 5 hours of thermal treatment.

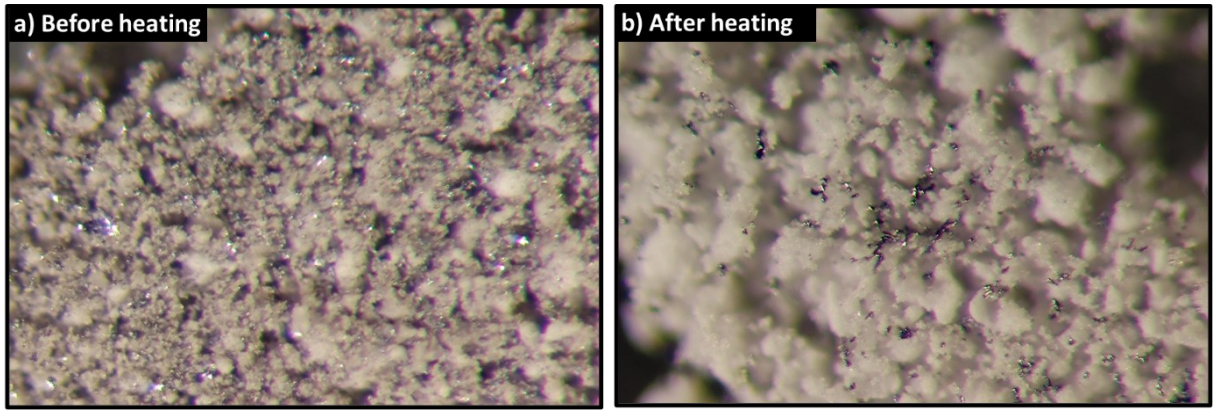

Figure 2-22. Optical images (magnification 160x) of silicon/silica powder mixtures before (a) and after (b) thermal treatment at 1400°C for 5 hours. Silica to silicon ratio 4:1 by mass. Larger relative quantities of silicon results in the Si microparticles melting together after heating.

It should be noted that much of the present discussion aims to identify the reaction conditions necessary to noticeably affect silicon domains in the powdered reaction mixtures while preventing Si particle sintering. This prerequisite required reaction mixtures containing excess SiO_2. If, however, maximizing silicon monoxide evolution is the desired outcome, the SiO_2:Si mass ratio should approach stoichiometric amounts (i.e., ca. 2:1 by mass).

2.2.3 Conclusions from the Powder System

By characterizing mixtures of silicon and silica powders after thermal treatment, we outline the reaction parameters necessary for the evolution of silicon monoxide via the direct reduction of silica by silicon. The loss of silicon domains was observable at 1200°C, but this result was highly contingent on the composition of the samples. Specifically, the crystallinity of the silica plays a dominant role in promoting sample reactivity. The use of silica as both a reagent and diluent also exposes the possibility of Si particle sintering in the reaction mixtures. Efforts to increase surface area of the silica to better interactions with silicon domains were met with mixed results as amorphous nanopowdered silica formed larger micro-sized particles upon crystallization.

2.3 In pursuit of Large (d > 100 nm) Silicon Nanocrystals, Part II: The Silicon Monoxide Problem

2.3.1 Results and Discussion: Continued from Section 2.1.2

Experiments using the silicon/silica powder system provided a wealth of information on the evolution of SiO. Armed with this knowledge, we return to the HSQ system. Recall the nanowires that deposited along the walls of the alumina tube furnace during heat treatment of HSQ (Figure 2-8). Further characterization of this material using XPS, XRD, and EDX indicated that the nanowires contained crystalline silicon and a mixture of crystalline and amorphous silicon oxides (Figures 3-23, 3-24, 3-25). Attempts to intentionally produce SiO from HSQ never yielded nanowire products in the same mass as the mass lost from the HSQ sample during heating (Table 2-1), but this was because the system was not optimized for nanowire deposition. Additionally, some of the HSQ is always inevitably lost due to silane gas ($SiH_{4(g)}$) formation during thermal decomposition.[63]

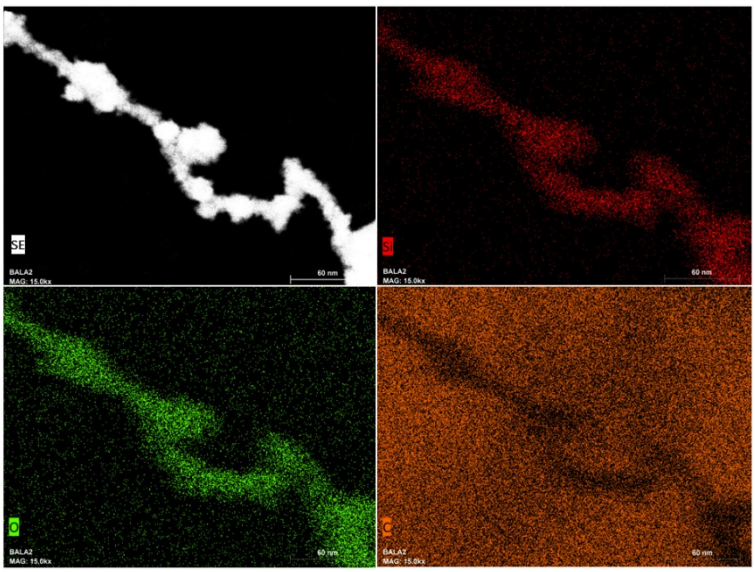

Figure 2-23. Secondary electron (SE) SEM image and corresponding EDX elemental mapping of nanowires. Elemental mapping shows silicon (red), oxygen (green), and carbon (orange). Sample was prepared by adhering the nanowires to an aluminum stub using carbon tape.

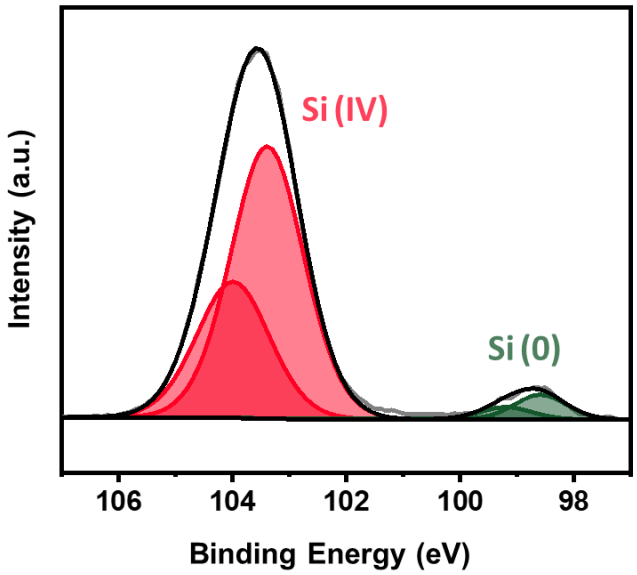

Element	Atomic %
Silicon	37.7
Oxygen	54.6
Carbon	6.5
Aluminum	1.2

Figure 2-24. High-resolution Si X-ray photoelectron spectrum of nanowires recovered from the surfaces within the alumina tube furnace (left); and elemental composition revealed by the XPS survey spectrum (right). Nanowires were prepared by annealing HSQ at 1600°C for 10 h. Alumina contamination originates from the tube and was a consequence of the nanowire collection method.

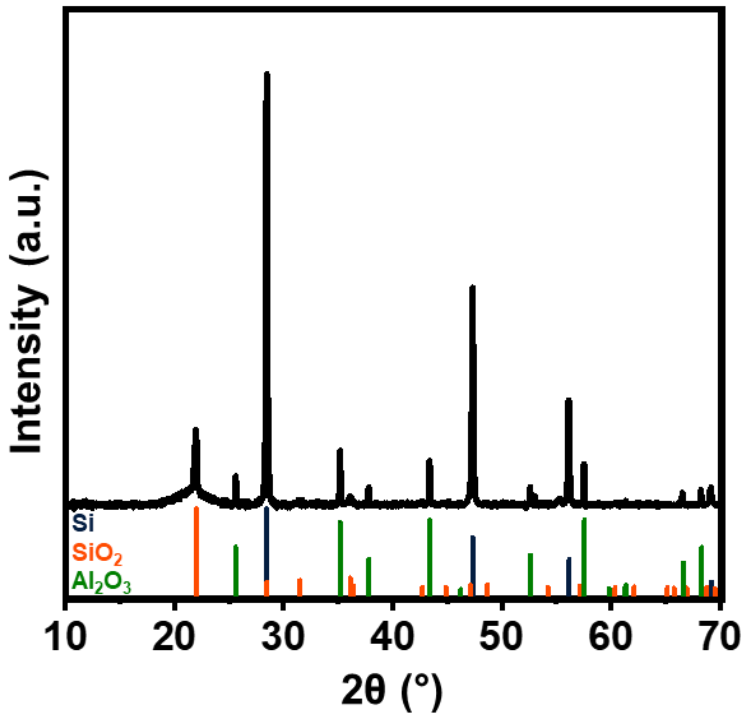

Figure 2-25. X-ray diffraction of the nanowires recovered from the surfaces within the alumina tube furnace. Nanowires were prepared by annealing HSQ at 1600°C for 10 h. Alumina contamination originates from the tube and was a consequence of the nanowire collection method.

Table 2-1. Mass analysis of HSQ and recovered nanowires.

Sample	Mass before heating (g)	Mass after heating (g)*
HSQ	2.1975	1.3773
Nanowires	n/a	0.1870

* HSQ Heated to 1600°C for 10 h.

As discussed in Section 3.2, the literature concerning Si-based nanowire fabrication from $SiO_{(g)}$ typically use mixtures of Si and SiO_2 which, when subject to high temperatures, react to form $SiO_{(g)}$ following reaction (1):

(1) $Si + SiO_2 \rightarrow 2\ SiO$

Given the similar mixture of silicon and silica that forms during HSQ disproportionation, it is reasonable that reaction (1) could transport Si atoms away from the annealing composite material and deposit them as nanowires in the cooler regions of the tube furnace. Unfortunately, comparing our observations with the existing academic literature concerning $SiO_{(g)}$ production is difficult. These studies ofthiten use temperatures below 1400°C or different reaction environments (e.g., vacuum, reducing atmospheres). These conditions differ from the present study where SiNP yield from HSQ is unaffected at 1400°C and only breaks down between 1500 and 1600°C. Moreover, there is nothing inherent to the reduction of silica by silicon which prevents the reaction from occurring at 1700°C, and there is no mention of a temperature limit for reaction (1) in the literature.[42] This is another deviation from our observation that the disappearance of SiNPs stops when HSQ is heated to 1700°C.

With a unique focus on the properties of the mixtures before and after thermal treatment, the data presented in Section 3.2 provided useful insights into the reaction conditions necessary for Si transport via $SiO_{(g)}$ evolution. We found that the crystallization of silica into cristobalite played a key role in $SiO_{(g)}$ formation and consistently increased the degree of Si removal from the mixtures. Similarly, our report explored the effect of reaction time on $SiO_{(g)}$ formation and found that longer reaction times resulted in more Si atom transport.[64] The data concerning the high-temperature HSQ anomaly is consistent with these findings. As illustrated in Figure 2-2, Figure 2-

3, and Figure 2-6, the appearance of strong diffraction peaks corresponding to crystalline SiO_2 coincides with the destruction of SiNP quality and eventual removal of virtually all Si(0) from the composite materials. The necessity for crystalline silica also explains the apparent lack of $SiO_{(g)}$ evolution from HSQ heated to 1700°C. At this temperature, the silica matrix begins to soften into a molten state, losing its crystal structure and preventing $SiO_{(g)}$ evolution. It is noteworthy that thermal treatment at 1700°C would push through the 1500–1600°C temperature window during heating and cooling. This likely results in the formation of some cristobalite and relatively weak SiO_2 peaks are observed in the diffraction patterns of these samples (Figure 2-6b). At a heating rate of 5°C/min the total time elapsed between 1500–1600°C is only 40 minutes; an insufficient length of time for SiNP damage via reaction (1). The cooling rate (10°C/min) is even faster, preventing any large-scale growth of cristobalite SiO_2.

We also find the onset of $SiO_{(g)}$ formation in agreement with a thermodynamic examination of the system. Based on the work by Schnurre *et al.,*[42] we present the Gibbs free energy (ΔG) curves of the SiO formation and decomposition reactions from 600–1700°C in Figure 2-26. The crossing of the curves at ~1570°C signifies the temperature beyond which the energy profit of silicon monoxide formation is higher than its decomposition into Si and SiO_2. This model closely approximates the onset of noticeable SiNP destruction presented in our study. Contrary to our observations, this plot also suggests that $SiO_{(g)}$ production should be favored even at $T \geq 1700$°C. In alignment with our previous study, we find the crystallization of cristobalite is key to the formation of silicon monoxide.[64] The softening of the silica matrix at 1700°C thus preserves the SiNPs by preventing $SiO_{(g)}$ formation.

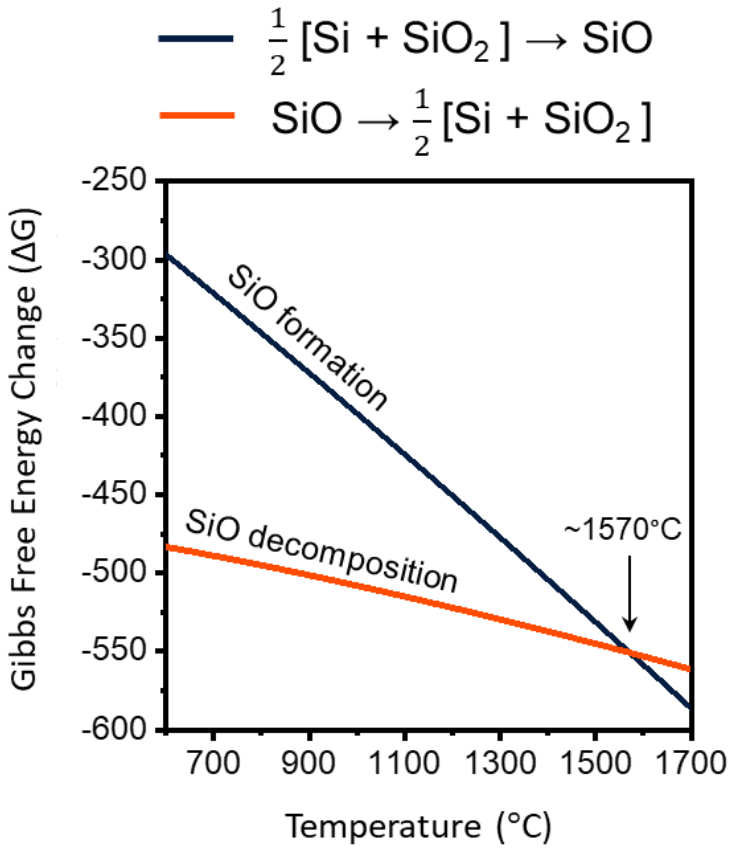

Figure 2-26. Plot of the Gibbs free energy change (kJ/mol) of the silicon monoxide formation and decomposition reactions.[42]

Lastly, we conducted an experiment to account for any unforeseen effects of using a pure Ar environment rather than the reducing atmosphere typically employed for thermal annealing of silicon-rich oxides. An analysis of this composite material reveals that heating HSQ in a flow of mixed Ar (95%) and H_2 (5%) does not prevent the loss of silicon domains from the composite material (Figure 2-27).

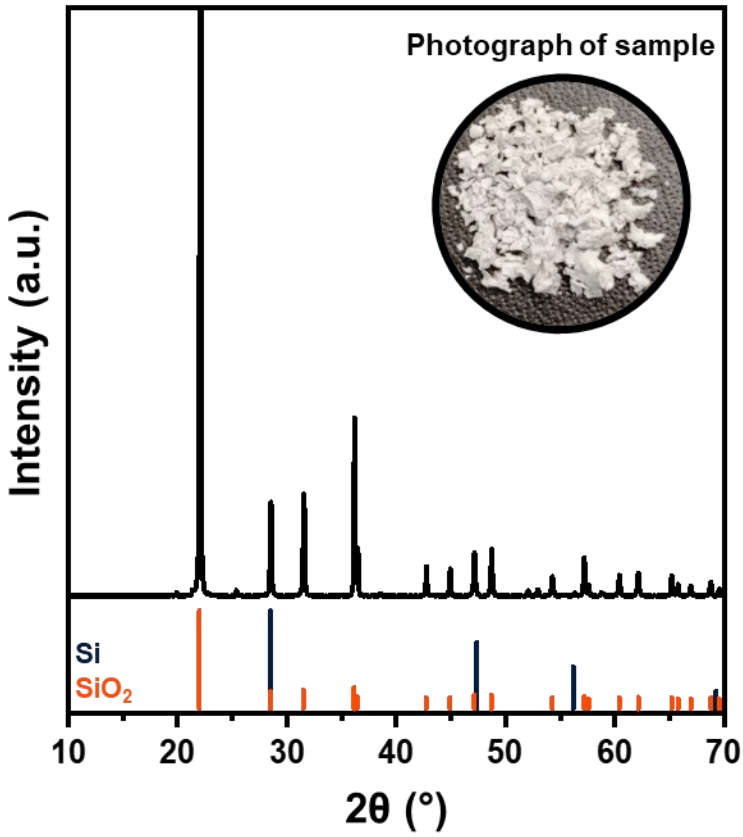

Figure 2-27. X-ray diffraction of the composite material after heating HSQ to 1600°C for 10 h under flowing Ar (95%) / H_2 (5%). Inset: photograph of the sample.

2.3.2 Conclusions

The work presented here demonstrates the continued reliability of hydrogen silsesquioxane as a precursor material for silicon nanoparticles. Aiming to reach a new, larger SiNP size-regime, HSQ was subjected to previously unexplored high temperatures. While charting the disproportionation reaction under an array of temperatures and dwell times, we discovered a perplexing range of reaction conditions which produced material devoid of any elemental silicon. Using X-ray photoelectron spectroscopy and electron microscopy, we tracked this anomalous region to between 1500°C and 1600°C and found the problem was made worse during longer reaction times. The

observation of silicon nanowires in conjunction with X-ray diffraction revealed that the crystallization of the silica matrix into cristobalite promoted the transport of Si atoms via gaseous silicon monoxide. This process was determined to be the cause of SiNP destruction. Increasing the reaction temperature to 1700°C limited this unwanted reaction by softening the surrounding silica and preventing the crystallization of the matrix.

2.3.3 Experimental

Materials

Silicon powder (325 mesh, 99% trace metals basis), silicon nanopowder (< 100 nm, trace metals basis), silicon dioxide (high-purity SiO_2 gel, 200-425 mesh size), and SiO_2 nanopowder (10-20 nm particle size, 99.5% trace metals basis) were purchased from Sigma Aldrich and used as received. The SiO_2 gel is denoted as "bulk" silica to differentiate it from the silica nanopowder. The Si nanopowder is referred to as "silicon nanoparticles" in the discussion. Fuming sulfuric acid (reagent grade, 20% free SO_3 bases), trichlorosilane (99%), and toluene (HPLC grade), were purchased from MilliporeSigma. Hydrofluoric acid (electronic grade, 48−50%) and sulfuric acid (reagent grade, 95−98%) were purchased from Fisher Scientific. Dry toluene was obtained from a Pure-Solv purification system with N_2 as the operating gas. All reagents and solvents were used as received.

Preparation of Crystalline SiO_2

While some of our experiments used amorphous silica in the mixed powder starting material, other experiments used crystalline silica. The preparation of crystalline silicon dioxide (cristobalite) starting materials required a thermal treatment prior to mixing with the silicon precursor. For these

experiments, high-purity amorphous SiO_2 gel ("bulk silica", 6.0 g) was placed in a ZrO_2 boat and transferred to a SentroTech Corporation STT-1700-2-12 high-temperature tube furnace equipped with a 2.5" diameter Al_2O_3 tube. The tube was heated in air to a peak temperature 1500°C at 5°C/min where it remained for 5 h. The tube furnace was allowed to cool naturally to room temperature. If the amorphous SiO_2 nanopowder was used in place of the high-purity SiO_2 gel, 1.0 g of nanopowder was crystallized at 1400 °C at a heating rate of 5°C/min for 5 h before cooling naturally to room temperature. Heating of SiO_2, irrespective of the precursor, provided a white, chalky solid that was subsequently ground in an agate mortar and pestle to yield a uniform white powder. The crystallinity of the product was evaluated using powder X-ray diffraction. All manipulations of the SiO_2 precursors and the products obtained from thermal processing were performed in a fumehood. In addition to standard laboratory personal protective equipment, personnel also wore N95 masks to minimize inhalation risks.

Preparation of Silica/Silicon Powder Mixtures

Four different silica materials were used to prepare the silica-silicon mixtures: amorphous bulk silica, crystalline bulk silica, amorphous nanopowder silica and crystalline nanopowder silica. In all cases, 4 g of the selected silica source and 0.2 g of 325 mesh silicon powders were dispensed in a 20:1 mass ratio into a round bottom flask equipped with a stir bar. Absolute ethanol (10 mL) was then added, the flask stoppered, and the mixture was stirred rapidly with a Teflon stir bar to disperse the powders. After approximately 5 minutes an additional 40 mL of ethanol was added to produce a viscous suspension that was stirred for an additional 1 h. Following removal of the ethanol using a rotary evaporator, the resulting Si/SiO_2 mixture was recovered as a homogenously mixed free-flowing grey powder. Further drying was achieved *via* submersion in an oil bath set to 100 °C for 1 h under flowing nitrogen gas.

Thermal Processing of Silica/Silicon Mixed Powders

In a typical experiment, Si/SiO_2 powder mixtures (ca. 0.25 g) are weighed, loaded into a ZrO_2 boat, and transferred to the SentroTech Corporation STT-1700-2-12 high-temperature tube furnace equipped with a 2.5" diameter Al_2O_3 tube. The tube was charged with flowing argon gas (10 cm^3/sec) and the furnace ramped to the predefined processing temperature (i.e., 1100-1400°C) at a rate of 5 °C/min. After holding at the peak temperature for the predefined dwell time (i.e, 1-5 h), the furnace cooled naturally to room temperature (ca. 16 h) before the samples were collected, weighed, and transferred to vials for storage.

Optical Microscopy

Optical images are taken using a Leica MZ9.5 stereo microscope equipped with a 48MP camera (LG LM-G900UM) mounted using a Celestron NexYZ 3-Axis Universal Smartphone Adapter. Powdered samples were pressed between two glass slides to achieve a flat surface. The top slide was removed before imaging.

X-ray Photoelectron Spectroscopy

X-ray photoelectron spectra were collected using a Kratos Axis 165 Ultra X-ray Photoelectron Spectrometer equipped with a monochromatic Al Kα radiation source (1486.6 eV) operating at 210 W. High-resolution spectra were measured using an analyzer pass energy of 20 eV and a step of 0.1 eV. For survey spectra, a pass energy of 160 eV and a step of 0.5 eV were used. Spectra were calibrated to C 1s 284.8 eV using adventitious carbon. Powdered samples adhere to double sided scotch tape on a metal loading bar.

Preparation of Hydrogen Silsesquioxane (HSQ)

HSQ is synthesized using an adapted literature procedure.[65] On an Ar-charged Schlenk line, concentrated sulfuric acid (15 mL) and fuming sulfuric acid (7 mL) are mixed in a 2 L RBF. Dry toluene (45 mL) is added dropwise, followed by a solution of trichlorosilane (16 mL) in dry toluene (110 mL), added dropwise overnight. Both additions occur with vigorous stirring from a Teflon stir bar. The mixture is decanted into a separatory funnel where the toluene layer is isolated and then washed three times with a solution of aqueous sulfuric acid (1.2 L H_2O, 0.4 L H_2SO_4). The washed organic layer is dried and neutralized over $MgSO_4$ and $CaCO_3$ overnight. Solvent reduction using a rotary evaporator followed by a final evaporation in vacuo yields a white solid that is stored under vacuum until use.

Preparation of Silicon Nanoparticles in a Silica Matrix ("The Composite Material")

HSQ (2 g) is transferred into a yttria-stabilised zirconia boat and loaded into a Carbolite CTF 18/300 tube furnace equipped with an alumina tube. The furnace is programed to heat at a ramp rate of 5°C/min to the selected temperature under flowing Ar gas, dwell for the desired time, then cool at 10°C/min. This yields an oxide composite containing Si nanodomains ("the composite material"). The resulting composite is ground using an agate mortar and pestle before shaking in a solution of ethanol and glass beads for 12 h. This procedure renders the composite into a powder with an approximate gain size of 1 μm. The powder is collected via vacuum filtration and dried overnight.

Preparation of Colloidal Hydride-terminated Silicon Nanoparticles

Powdered composite (300 mg) is etched using a 1:1:1 solution of ethanol: deionized water: HF (3 mL : 3 mL : 3 mL) in a plastic beaker with stirring from a Teflon stir bar. After 90 minutes,

toluene is added to the aqueous solution and the SiNPs are extracted using a plastic pipette. The colloidal SiNPs are isolated by centrifugation (5000 rpm for 5 min) before redispersing in 15 mL of toluene. This process is repeated twice to remove residual etchant.

X-Ray Photoelectron Spectroscopy (XPS)

X-ray photoelectron spectra were collected using a Kratos Axis 165 Ultra X-ray Photoelectron Spectrometer equipped with a monochromatic Al K_α radiation source (1486.6 eV) operating at 210 W. High-resolution spectra were measured using an analyzer pass energy of 20 eV and a step of 0.1 eV. For survey spectra, a pass energy of 160 eV and a step of 0.5 eV were used. Spectra were calibrated to C 1s 284.8 eV using adventitious carbon.

Transmission Electron Microscopy (TEM)

Transmission electron microscopy bright field images were acquired using a JEOL JEM-ARM200CF S/TEM electron microscope at an accelerating voltage of 200 kV. TEM samples were prepared by depositing a drop of a dilute toluene suspension of the desired SiNPs onto an ultra-thin carbon coated copper grid (Electron Microscopy Inc.). The grid bearing the sample was kept in a vacuum chamber at 0.2 bar for at least 12 h prior to data collection. Images were analysed using ImageJ. When calculating nanoparticle size, 300 particles were counted, and their sizes plotted as an average-shifted histogram.[66]

Powder X-Ray Diffraction (XRD)

Powder X-ray diffraction was performed using a Bruker D8 Advance powder diffractometer. The instrument is equipped with a SSD160 detector and a Cu radiation source ($K_{\alpha1}$ = 1.54056 Å; $K_{\alpha2}$ removed) operating at 40 kV and 40 mA. All samples were finely ground using a mortar and pestle before analysis on a zero-background silicon substrate. The amount of powder loaded onto the

diffraction plate was consistent between samples and the resulting diffraction patterns were not normalized.

Scanning Electron Microscopy and Energy Dispersive X-ray Spectroscopy

Scanning electron microscopy was performed on a Zeiss Sigma 300 VP-FESEM. The instrument is equipped with a Bruker energy dispersive X-ray spectroscopy system with dual silicon drift detectors each with an area of 60 mm^2 and a resolution of 123 eV. Imaging was collected using a secondary electron detector at accelerating voltages varying between 5 and 15 kV. Samples are prepared by adhering powder to an aluminum stub using double sided carbon tape.

2.4 References

1. Takagi, H.; Ogawa, H.; Yamazaki, Y.; Ishizaki, A.; Nakagiri, T. Quantum Size Effects on Photoluminescence in Ultrafine Si Particles, *Appl. Phys. Lett.* **1990**, *56*, 2379–2380.
2. Mangolini, L. Synthesis, properties, and applications of silicon nanocrystals. *J. Vac. Sci. Technol. B* **2013**, *31*, 020801.
3. Milliken, S.; Thiessen, A. N.; Cheong, I. T.; O'Connor, K. M.; Li, Z.; Hooper, R. W.; Robidillo, C. J. T.; Veinot, J. G. C. "Turning the dials": Controlling Synthesis, Structure, Composition, and Surface Chemistry to Tailor Silicon Nanoparticle Properties. *Nanoscale* **2021**, *13*, 16379–16404.
4. Fu, Y. H.; Kuznetsov, A. I.; Miroshnichenko, A. E.; Yu, Y. F.; Luk'yanchuk, B. Directional visible light scattering by silicon nanoparticles. *Nat. Commun.* **2013**, *4*, 1527.
5. Sugimoto, H.; Fujii, M. Colloidal Mie resonant silicon nanoparticles. *Nanotechnology* **2021**, *32*, 452001.
6. Jahani, S.; Jacob, Z. All-dielectric metamaterials. *Nat. Nanotechnol*. **2016**, *11*, 23–36.
7. De Marco, L. M.; Semlali, S.; Korgel, B. A; Barois, P.; Drisko, G. L.; Aymonier, C. Silicon-Based Dielectric Metamaterials: Focus on the Current Synthetic Challenges. *Angew. Chem. Int. Ed.* **2018**, *57*, 4478–4498.

8. Eslamisaray, M. A.; Wray, P. R.; Lee, Y.; Nelson, G. M.; Ilic, O.; Atwater, H. A.; Kortshagen, U. R. A Single-Step Bottom-up Approach for Synthesis of Highly Uniform Mie-Resonant Crystalline Semiconductor Particles at Visible Wavelengths. *Nano Lett.* **2023**, *23*, 1930–1937.
9. De Marco, L. M.; Jiang, T.; Fang, J.; Lacomme, S.; Zheng, Y.; Baron, A.;. Korgel, B. A.; Barois, P.; Drisko, G. L.; Aymonier, C. Broadband Forward Light Scattering by Architectural Design of Core–Shell Silicon Particles. *Adv. Funct. Mater.* **2021**, *31*, 2100915.
10. Sun, H.; Miyazaki, S.; Tamamitsu, H.; Saitow, K. One-Pot Facile Synthesis of a Concentrated Si Nanoparticle Solution. *Chem. Commun.* **2013**, *49*, 10302–10302.
11. Saitow, K.; Suemori, H.; Tamamitsu, H. Enhancement of Fluorescence Intensity by Silicon Particles and Its Size Effect. *Chem. Commun.* **2014**, *50*, 1137–1140.
12. Sakamoto, M.; Terada, S.; Mizutani, T.; Saitow, K. Large Field Enhancement of Nanocoral Structures on Porous Si Synthesized from Rice Husks. *ACS Appl. Mater. Interfaces* **2021**, *13*, 1105–1113.
13. Sugimoto, H.; Okazaki, T.; Fujii, M. Mie resonator color inks of monodispersed and perfectly spherical crystalline silicon nanoparticles. *Adv. Opt. Mater.* **2020**, *8*, 2000033.
14. Hessel, C. M.; Henderson, E. J.; Veinot J. G. C. Hydrogen Silsesquioxane: A Molecular Precursor for Nanocrystalline Si-SiO_2 Composites and Freestanding Hydride-Surface-Terminated Silicon Nanoparticles. *Chem. Mater.* **2006**, *18*, 6139–6146.
15. Milburn, L.; Robidillo, C. J.; Dalangin, R.; Shen, Y.; Veinot, J. G. C. A Complementary Silicon Quantum Dot-Enzyme Platform for the Selective Detection of Nitroaromatic Compounds: Explosives versus Nerve Agents. *ACS Appl. Nano Mater.* **2022**, *5*, 11984–11990.
16. Cheong, I. T.; Mock, J.; Kallergi, M.; Groß, E.; Meldrum, A.; Rieger, B.; Becherer, M.; Veinot, J. G. C. Colloidal Silicon Quantum Dot-Based Cavity Light-Emitting Diodes with Narrowed and Tunable Electroluminescence. *Adv. Opt. Mater.* **2023**, *11*, 2201834.
17. Thiessen, A. N.; Zhang, L.; Oliynyk, A. O.; Yu, H.; O'Connor, K. M.; Meldrum, A.; Veinot, J. G. C. A Tale of Seemingly “Identical” Silicon Quantum Dot Families: Structural Insight into Silicon Quantum Dot Photoluminescence. *Chem. Mater.* **2020**, *32*, 6838–6846.

18. Milliken, S.; Cheong, I. T.; Cui, K.; Veinot, J. G. C. Boron Doping of Silicon Quantum Dots via Hydrogen Silsesquioxane-Capped Diffusion for Photovoltaics and Medical Imaging. *ACS Appl. Nano Mater.* **2022**, *5*, 15785–15796.
19. Hessel, C. M.; Reid, D.; Panthani, M. G.; Rasch, M. R.; Goodfellow, B. W.; Wei, J.; Fujii H.; Akhavan, V.; Korgel, B. A. Synthesis of Ligand-Stabilized Silicon Nanocrystals with Size-Dependent Photoluminescence Spanning Visible to Near-Infrared Wavelengths. *Chem. Mater.* **2012**, *24*, 393–401.
20. Thiessen, A. N.; Ha, M.; Hooper, R. W.; Yu, H.; Oliynyk, A. O.; Veinot, J. G. C.; Michaelis, V. K. Silicon Nanoparticles: Are They Crystalline from the Core to the Surface? *Chem. Mater.* **2019**, *31*, 678–688.
21. Hom, T.; Kiszenick, W.; Post, B. Accurate lattice constants from multiple reflection mesurements II. Lattice constants of germanium, silicon and diamond. *J. Appl. Crystallogr.* **1975**, *8*, 457–458.
22. Downs, R. T.; Palmer, D. C. The pressure behavior of alpha cristobalite. *Am. Mineral*. **1994**, *79*, 9–14.
23. Pan, Z. W., Dai, Z. R.; Xu, L..; Lee, S. T.; Wang, Z. L. Temperature-Controlled Growth of Silicon-Based Nanostructures by Thermal Evaporation of SiO Powders. *J. Phys. Chem. B* **2001**, *105*, 2507–2514.
24. Zhou, J.; Huang, J.; Chen, H.; Samanta, A.; Linnros, J.; Yang, Z.; Sychugov, I. Low-Cost Synthesis of Silicon Quantum Dots with Near-Unity Internal Quantum Efficiency. *J. Phys. Chem. Lett.* **2021**, *12*, 8909–8916.
25. Terada, S.; Xin, Y.; Saitow, K. I. Cost-Effective Synthesis of Silicon Quantum Dots. *Chem. Mater*. **2020**, *32*, 8382–8392.
26. Mamiyaa, M.; Takeia, H.; Kikuchib, M.; Uyedaa, C. Preparation of fine silicon particles from amorphous silicon monoxide by the disproportionation reaction. *J. Cryst. Growth* **2001**, *229*, 457–461.
27. Sun, W.; Qian, C.; Cui, X. S.; Wang, L.; Wei, M.; Casillas, G.; Helmyb, A. S.; Ozin, G. A. Silicon monoxide – a convenient precursor for large scale synthesis of near infrared emitting monodisperse silicon nanocrystals. *Nanoscale* **2016**, *8*, 3678–3684.

28. Valenta, J.; Greben, M.; Dyakov, S. A.; Gippius, N. A.; Hiller, D.; Gutsch, S.; Zacharias, M. Nearly perfect near-infrared luminescence efficiency of Si nanocrystals: A comprehensive quantum yield study employing the Purcell effect. *Sci. Rep*. **2019**, *9*, 11214.
29. Chlouba, T.; Trojánek, F.; Kopecký Jr., V.; López-Vidrier, J.; Hernandéz, S.; Hiller, D.; Gutsch, S.; Zacharias, M.; Malý, P. Pathways of carrier recombination in Si/SiO_2 nanocrystal superlattices. *J. Appl. Phys.* **2019**, *126*, 163101.
30. Hiller, D.; König, D.; Nagel, P.; Merz, M.; Schuppler, S.; Smith, S. C. On the Location of Boron in SiO_2-Embedded Si Nanocrystals—An X-ray Absorption Spectroscopy and Density Functional Theory Study. *Phys. Status Solidi B* **2021**, *258*, 2000623.
31. Guha, S.; Pace, M. D.; Dunn, D. N.; Singer, I. L. Visible light emission from Si nanocrystals grown by ion implantation and subsequent annealing. *Appl. Phys. Lett*. **1997**, *70*, 1207–1209.
32. Zhang, R.; Yuan, Y.; Zhang, J.; Zuo, W.; Zhou, Y.; Gao, X.; Wang, W.; Qin, Z.; Zhang, Q.; Chen, F.; Du, Z.; Li, J. A light-influenced memristor based on Si nanocrystals by ion implantation technique. *J. Mater. Sci.* **2021**, *56*, 2323–2331.
33. Beyer, V.; von Borany, J.; Heinig, K. H. Dissociation of Si^+ ion implanted and as-grown thin SiO_2 layers during annealing in ultra-pure neutral ambient by emanation of SiO. *J. Appl. Phys.* **2007**, *101*, 053516.
34. Wang, N.; Tang, Y.H.; Zhang, Y.F.; Lee, C.S.; Bello, I.; Lee, S.T. Si Nanowires grown from silicon oxide. *Chem. Phys. Lett.* **1999**, *299*, 237–242.
35. Shi, W. S.; Peng, H. Y..; Zheng, Y. F.; Wang, N.; Shang, N. G.; Pan, Z. W.; Lee, C. S.; Lee, S. T. Synthesis of large areas of highly oriented, very long silicon nanowires. *Adv. Mater*. **2000**, *12*, 1343–1345.
36. Zhang, B. C.; Wang, H.; He, L.; Zheng, C. J.; Jie, J. S.; Lifshitz, Y.; Lee, S. T.; Zhang, X. H. Centimeter-Long Single-Crystalline Si Nanowires. *Nano Lett*. **2017**, *17*, 7323–7329.
37. Srivastava, S.K.; Singh, P.K.; Singh, V.N.; Sood, K.N.; Haranath, D.; Kumar, V. Large-scale synthesis, characterization and photoluminescence properties of amorphous silica nanowires by thermal evaporation of silicon monoxide. *Physica E* **2009**, *41*, 1545–1549.
38. Winkler, C. Ueber die Reduction von Sauerstoffverbindungen durch Magnesium. *Ber*. **1890**, *23*, 2642–2668.
39. Potter, H. N. Silicon monoxide. *Trans. Am. Electrochem. Soc*. **1908**, *12*, 191–214.

40. Roeber, E. F.; Parmelee, H. C. *Electrochemical and Metallurgical Industry*, Electrochemical Publishing Company, London, 1907.
41. Kubascheeski, O.; Chart, T. G. Silicon monoxide pressures due to the reaction between solid silicon and silica. *J. Chem. Thermodyn.* **1974**, *6,* 467–476.
42. Schnurre, S. M.; Grobner, J.; Schmid-Fetzer, R. Thermodynamics and phase stability in the Si–O system. *J. Non-Cryst. Solids* **2004**, *336*, 1–25.
43. Benyon, J. Silicon Monoxide: Fact or Fiction. *Vacuum* **1970**, *20*, 293–294.
44. Yasaitis, J. A.; Kaplow, R. Structure of amorphous silicon monoxide. *J. Appl. Phys.* **1972**, *43*, 995–1000.
45. Hohl, A.; Wieder, T.; van Aken, P.A.; Weirich, T.E.; Denninger, G.; Vidal, M.; Oswald, S.; Deneke, C.; Mayer, J.; Fuess, H. An interface clusters mixture model for the structure of amorphous silicon monoxide (SiO). *J. Non-Cryst. Solids* **2003**, *320*, 255–280.
46. Schulmeister, K.; Mader, W. TEM investigation on the structure of amorphous silicon monoxide. *J. Non-Cryst. Solids* **2003**, *320*, 143–150.
47. Hirata, A.; Kohara, S.; Asada, T.; Arao, M.; Yogi, C.; Imai, H.; Tan, Y.; Fujita, T.; Chen, M. Atomic-scale disproportionation in amorphous silicon monoxide. *Nat. Commun*. **2016**, *7*, 11591.
48. Li, F.; Huang, Y.; Wang, S.; Zhang, S. Critical review: Growth mechanisms of the self-assembling of silicon wires. *J. Vac. Sci. Technol. A* **2020**, *38*, 010802.
49. Li, F. J.; Zhang, S.; Lee, J. W. Rethinking on the silicon nanowire growth mechanism during thermal evaporation of Si-containing powders. *Thin Solid Films* **2014**, *558*, 75–85.
50. Vogli, E.; Mukerji, J.; Hoffman, C.; Kladny, R.; Sieber, H.; Greil, P. Conversion of oak to cellular silicon carbide ceramic by gas-phase reaction with silicon monoxide. *J. Am. Ceram. Soc*. **2001**, *84*, 1236–40.
51. Aarnæs, T.S., Ringdalen, E. & Tangstad, M. Silicon carbide formation from methane and silicon monoxide. *Sci. Rep.* **2020,** *10*, 21831.
52. Chen, X.; Zhang, D.; Zhang, X.; Liu, Y.; Li, X.; Xiang, G. Synthesis and growth mechanism of Mn-doped nanodot embedded silica nanowires. *Physica B* **2019**, *571*, 10–17.
53. AlKaabi, K.; Prasad, D. L. V. K.; Kroll, P. ; Ashcroft, N. W.; Hoffmann, R. Silicon Monoxide at 1 atm and Elevated Pressures: Crystalline or Amorphous? *J. Am. Chem. Soc.* **2014**, *136*, 3410–3423.

54. Neizvestny, I. G.; Shwartz, N. L. Monte Carlo Simulation of Semiconductor Nanostructure Growth. In *Advances in Semiconductor Nanostructures*. Latyshev, A. V.; Dvurechenskii, A. V.; Aseev, A. L., Eds.; Elsevier, 2017, ch. 14, pp. 345–364.
55. Ferguson, F. T.; Nuth, J. A. Vapor Pressure and Evaporation Coefficient of Silicon Monoxide over a Mixture of Silicon and Silica. *J. Chem. Eng. Data* **2012**, *57*, 721–728.
56. Broggi, A.; Tangstad, M.; Ringdalen, E. Characterization of a Si-SiO_2 Mixture Generated from SiO(g) and CO(g). *Metall. Mater. Trans. B* **2019**, *50*, 2667–2680.
57. Porter, R. F.; Chupka, W. A.; Ingiiram, M. G. Mass Spectrometric Study of Gaseous Species in the Si-SiO_2 System. *J. Chem. Phys*. **1955**, *23*, 216–217.
58. Chase, M. W. *NIST-JANAF Themochemical Tables,* 4th ed.; *J. Phys. Chem. Ref. Data*, 1998.
59. Nagamori, M.; Boivin, J. A.; Claveau, A. Gibbs free energies of formation of amorphous Si_2O_3, SiO and Si_2O. *J. Non-Cryst. Solids* **1995**, *189*, 270–276.
60. Sarikov, A.; Zacharias, M. Gibbs free energy and equilibrium states in the Si/Si oxide systems. *J. Phys. Condens. Matter* **2012**, *24*, 385403–385403.
61. Sarikova, A.; Zhigunov, D. Thermodynamic mechanism of the intermixing of multilayered structures in the SiO_X/SiO_2 superlattices with nanometer thick layers. *Mater. Today Commun.* **2017**, *13*, 163–169.
62. Pizzini, S. Physical Chemistry of Semiconductor Materials and Processes, Wiley, United Kingdom, 2015.
63. Yang, C. C.; Chen, W. C. The structures and properties of hydrogen silsesquioxane (HSQ) films produced by thermal curing. *J. Mater. Chem.* **2002**, *12*, 1138–1141.
64. O'Connor, K. M.; Rubletz, A.; Trach, J.; Butler, C.; Veinot, J. G. C. Understanding Silicon Monoxide Gas Evolution from Mixed Silicon and Silica Powders. *Nanoscale Horiz.* **2023**, *8,* 892–899.
65. Frye, C. L.; Collins, W. T. The Oligomeric Silsesquioxanes, $(HSiO_{3/2})_n$. *J. Am. Chem. Soc.* **1970**, *92*, 5586–5588.
66. Murphy, C. J.; Buriak, J. M. Best Practices for the Reporting of Colloidal Inorganic Nanomaterials. *Chem. Mater.* **2015**, *27*, 4911–4913.

Chapter 3

Synthesis of Silicon Nanocrystals in Air and the Impact of the Gas Environment on the Disproportionation of Hydrogen Silsesquioxane

Silicon nanocrystals, as well as other semiconductor nanomaterials, have been incorporated into a variety of optical and electronic applications, and the synthesis of these materials is critical for the continued development of emerging technologies. To prevent oxidation, silicon nanocrystals are exclusively synthesized using an inert or reducing atmosphere. This chapter describes the synthesis of silicon nanocrystals in air using the silicon-rich oxide hydrogen silsesquioxane. A comparison of the silicon nanocrystals produced in air to particles made in an inert atmosphere finds that the reaction in air results in a lower yield. In addition, a comparison of silicon nanocrystals prepared in argon to those prepared in forming gas (5% H_2 in Ar) finds no discernible benefit to the photoluminescence when hydrogen gas is used. In contrast, the presence of H_2 can affect the sample crystallinity at 1400°C and 1700°C. We anticipate that the trends observed in this work can be applied to other group 14 nanocrystal syntheses employing a solid-state disproportionation reaction.

3.1 Introduction

Silicon nanocrystals (SiNCs) can be prepared by employing syntheses in the liquid, solid, gas, plasma, or supercritical phases.[1-4] Among these, reactions in the solid-state offer many advantages. Solid-state syntheses avoid the use of dangerous reagents, such as silane (SiH_4) or lithium aluminum hydride ($LiAlH_4$), that are common in aerosol- and solution-based reactions.[5,6] In addition, solid-state reactions are performed at comparatively higher temperatures, resulting in SiNCs that are highly crystalline and exhibit better photoluminescence properties than silicon nanoparticles prepared using different techniques.[7]

The solid-state synthesis of SiNCs is accomplished by thermally-inducing a disproportionation reaction in a silicon-rich oxide (SRO).[8] SROs encompass any silicon-oxide containing a higher proportion of silicon atoms compared to stoichiometric silicon dioxide (i.e. SiO_x where $x < 2$).[9] When exposed to high temperatures (> 600°C), SROs decompose through a disproportionation reaction to form a matrix of silica [SiO_2, Si(IV)] encompassing nanoparticles of silicon [Si(0)].[9,10] In this way, SROs provide both the source of Si atoms for nanoparticle formation and a protective oxide matrix. As processing temperatures approach 1000°C, the silicon nanoparticles begin to crystallize.[11] The final size of the SiNCs is a function of the peak processing temperature, reaction time, and the stoichiometry of the SRO.[12] If standalone particles are desired, the protective silica matrix is chemically etched using hydrofluoric acid (HF), affording a colloidal solution of SiNCs.[11]

The thermal treatment of silicon-rich oxides is typically performed under a mixture of 5% H_2 in inert gas (i.e., N_2 or Ar).[10,11,13-16] This reducing atmosphere, also called forming gas, has been reported to improve the photoluminescence of oxide-embedded SiNC thin films by passivating defect sites at the Si–SiO_2 interface.[17-24] These findings were influential, and the thermal treatment

of SROs in forming gas became the routine procedure for solid-state SiNC synthesis. This included syntheses that either used bulk SRO precursors rather than thin films, targeted colloidal SiNCs rather than oxide-embedded SiNCs, or prepared SiNCs at sizes too large for quantum confinement ($d > 9$ nm).[10,11,13-15,25-30] It remains unclear to what extent, if any, the passivation of defects at the Si–SiO_2 interface benefits the photoluminescence of SiNCs liberated from the oxide matrix. Moreover, it is unknown if the reducing atmosphere has any additional impacts on the synthesis of SiNCs.

Previous investigations have interrogated the impact of temperature and time on the resulting structure of SiNCs, but limited attention has been given to the processing atmosphere and pre-etched matrix.[30] Using solid-state nuclear magnetic resonance (NMR), X-ray powder diffraction (XRD), X-ray photoelectron spectroscopy (XPS), and scanning electron microscopy (SEM), we investigate the effects of the gaseous environment during heating of the SRO, hydrogen silsesquioxane (HSQ). In addition, we analyze the morphology and photoluminescence of colloidal SiNCs after liberation from the oxide matrix.

3.2 Results and Discussion

Hydrogen silsesquioxane was selected for this study because it can be prepared with common wet-lab techniques, is solution processable, has a history of providing high quality silicon quantum dots, and can be used to prepare SiNCs spanning a wide size range.[7,31] While HSQ is molecularly distinct from other SROs, we anticipate that the findings illuminated by this work can be applied to other SRO materials.

A reaction overview is provided in Scheme 3-1. To evaluate the influence of the atmosphere during thermal treatment, HSQ is heated to 1100°C, 1400°C, and 1700°C in forming gas (95% Ar / 5% H_2), pure Ar, and air.

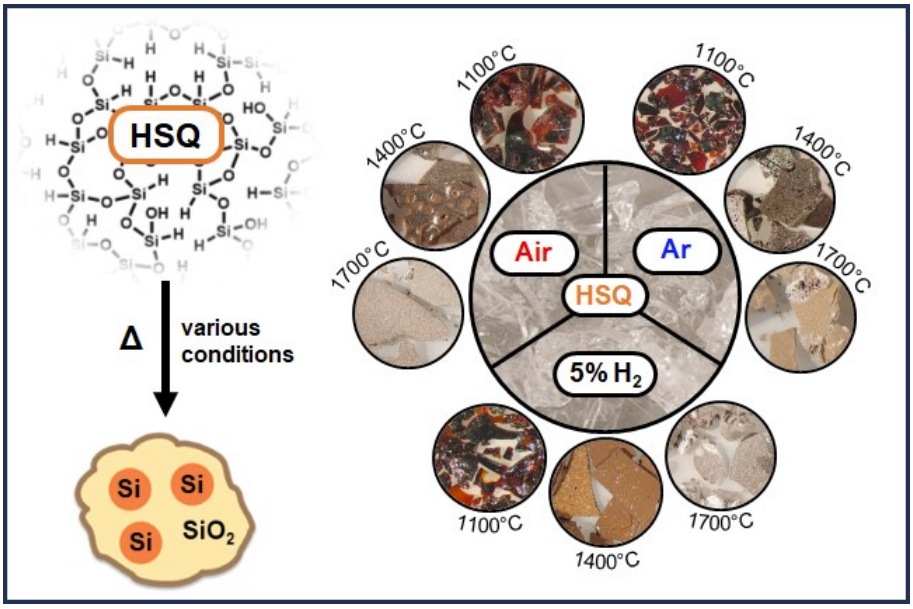

Scheme 3-1. Reaction overview of SiNC synthesis from HSQ. Three peak processing temperatures and three different atmospheric conditions are used to prepare nine different composites of oxide-embedded SiNCs. Photographs of the composites are shown in circles.

Solid HSQ is a white, amorphous extended structure containing Si–H groups along a polymeric network of Si–O bonds. The specific molecular configurations found within the polymer are numerous. The thermal decomposition of the HSQ affords a solid composite material of crystalline silicon nanoparticles and silicon dioxide ("*the composite*", Scheme 1). This material is ground into a powder by hand using a mortar and pestle and characterized using XRD, NMR, and XPS.

3.2.1 Characterization of the Composite Materials

X-Ray Diffraction

The crystallinity of the composite materials is evaluated using powder X-ray diffraction (XRD). These diffraction patterns are presented in Figure 3-1.

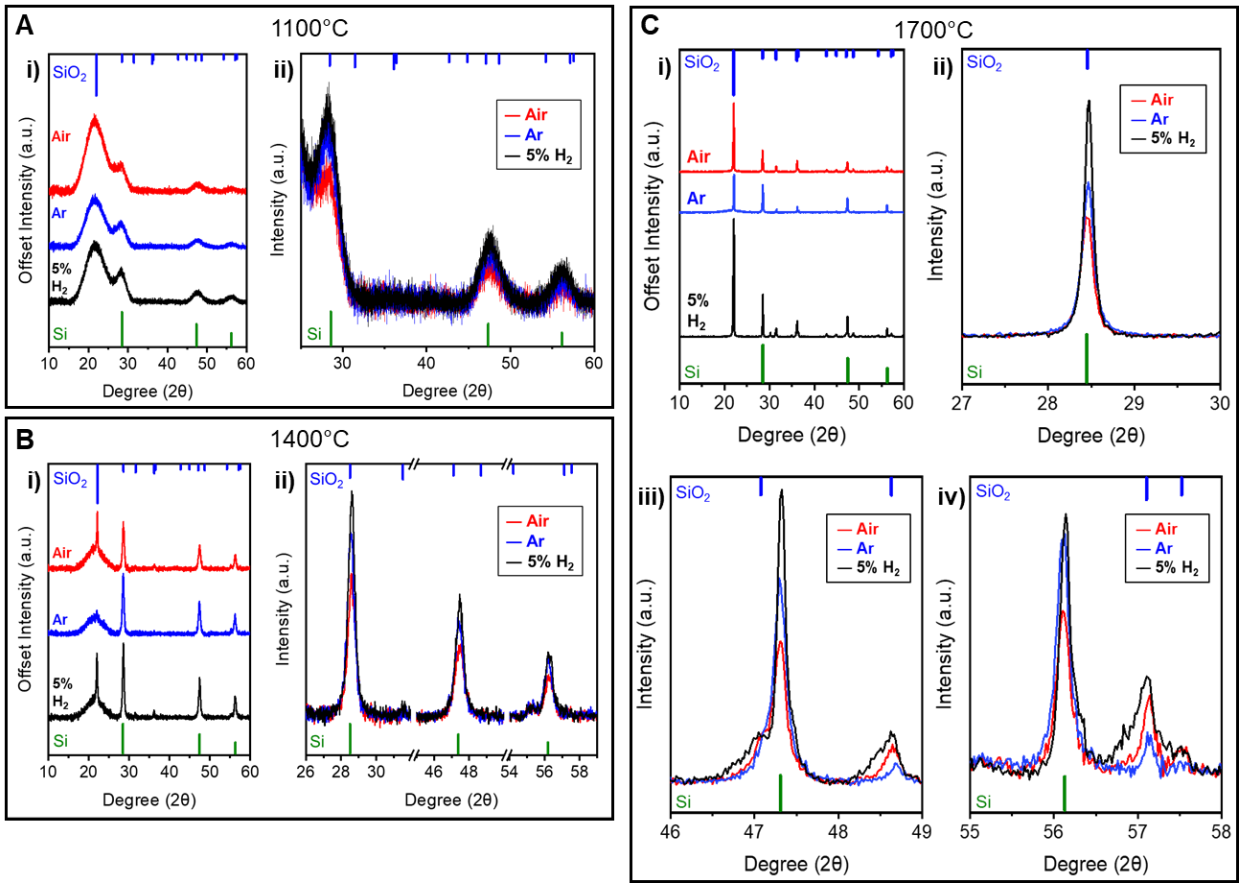

Figure 3-1. Powder X-ray diffraction patterns of the composite materials after heating to 1100°C (A), 1400°C (B), and 1700°C (C) in air (red), argon (blue), and 5% hydrogen / 95% argon (black). The full diffractograms (i) are presented alongside overlaid patterns (ii-iv) to better visualize the differences in reflection intensity. The calculated reflections for crystalline Si are provided below the patterns in green; the calculated reflections for cristobalite (SiO_2) are provided above the patterns in blue.[32,33]

Remarkably, the XRD data suggests that, across all temperatures, nanocrystalline domains of Si are afforded regardless of processing atmosphere. In agreement with previous studies, we observed an intensity increase and peak narrowing in the Si reflections when HSQ is heated to higher temperatures, suggesting that larger SiNCs are formed at higher temperatures (Figure 3-1A, B, C).[10,25,28,31] Also seen are reflections assigned to crystalline SiO_2 (cristobalite) which emerge at 1400°C and are prominent after heating to 1700°C. Across the three temperatures, the thermal treatment of HSQ in air produces Si reflections that are comparatively weaker and broader than HSQ heated in Ar or forming gas. An estimation of the Si crystallite sizes at 1100°C and 1400°C using the Scherrer analysis is summarized in Table 3-1.

Table 3-1. Nanocrystallite size determined by Scherrer analysis of XRD

	1100°C	**1400°C**
Air	3.4 nm	17.8 nm
Argon	3.6 nm	18.4 nm
5% H_2 in Ar	3.6 nm	18.5 nm

A comparison of the SiO_2 reflections between the three samples shows a greater degree of cristobalite SiO_2 in composites heated under air and 5% H_2 than composites heated in Ar. These results suggest that heating in air or hydrogen promotes the crystallization of the SiO_2 matrix. Hydrogen has been reported to crystallize amorphous Si, but it is not known to crystallize SiO_2.[34] The crystallization of the oxide matrix is important because it can encourage undesirable reactions between the SiNCs and their host material. In previous studies, we explored the temperatures at which SiO_2 begins to crystallize in HSQ and investigated the influence of its formation on SiNC synthesis.[31]

X-Ray Photoelectron Spectroscopy

X-ray photoelectron spectroscopy (XPS) provides information concerning elemental composition and oxidation state of a sample. Despite its surface selectivity, XPS can probe the composite materials far enough to provide insightful data on the Si atoms present in the SiNCs and the surrounding oxide matrix. These spectra are presented in Figure 3-2.

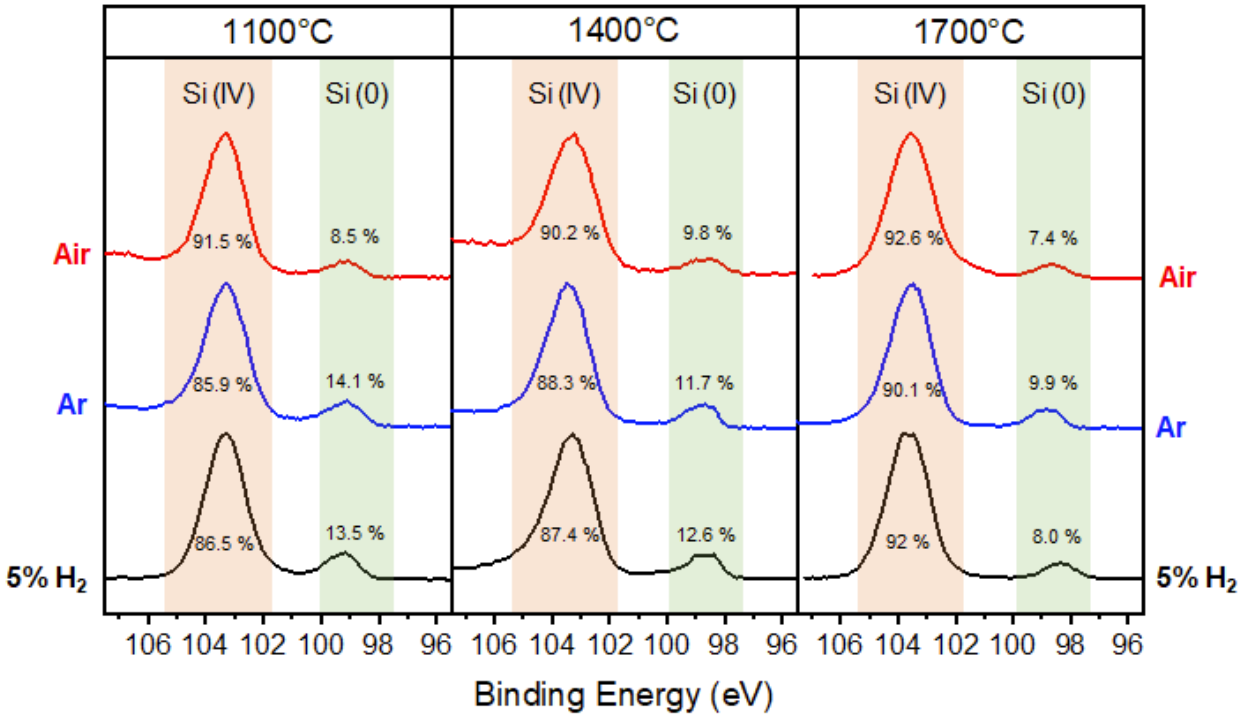

Figure 3-2. X-ray photoelectron spectra of the oxide-embedded SiNC composites produced by thermal treatment of HSQ. Composites are ground to a powder before analysis to probe the composite interior more effectively. Peaks assigned to Si(IV) and Si(0) are highlighted. The Si(0) signal originates from the SiNCs and the Si(IV) signal originates from the oxide matrix. Peak integration provides the relative atomic % of each oxidation state. Samples heated in air are shown in red; Ar in blue; and 5% H_2 / 95% Ar in black.

In agreement with the XRD data, the XP spectra show that all samples, regardless of atmospheric conditions, produce domains of reduced Si(0) and oxidized Si(IV) when heated to 1100°C, 1400°C, or 1700°C. The atomic percent of Si(0) atoms for samples heated in Ar and 5% H_2 are approximately 14% at 1100°C, 12% at 1400°C, and 9% at 1700°C. These values are in alignment with previous reports on the yield of SiNCs from the composite material.[7,26] The decrease in Si(0) content at higher processing temperatures is likely caused by the surface selectivity of XPS. As the embedded-SiNC becomes larger, a smaller fraction of the particles can be effectively probed. A comparison of composites heated in Ar and 5% H_2 to composites produced in air show a relatively lower atomic percent of Si(0) when HSQ is heated in air. This finding agrees with the XRD analysis and suggests that heating HSQ in air produces a comparatively lower yield of SiNCs.

Nuclear Magnetic Resonance

Nuclear magnetic resonance (NMR) spectroscopy is a valuable tool for investigating challenging chemical environments with an element-specific probe. Despite the low natural abundance of ^{29}Si (4.7%) and prohibitively long T_1 relaxation times, ^{29}Si NMR has been successfully applied to the study of freestanding SiNCs, mesoporous SiNPs, and silicon nanosheets (SiNS).[28,35–37] As such, NMR spectroscopy is useful for examining the different silicon, silica, and silicon suboxide environments present in the composite materials after thermal treatment under different processing atmospheres.

Figure 3-3 presents ^{29}Si MAS NMR for HSQ processed at a series of reaction temperatures (1100°C, 1400°C, 1700°C) and processing environments (5% H_2 in Ar, Ar, Air). Due to prohibitively long T_1 in these materials, experiments in Figure 3-3(a) were performed using a short recycle delay (D1) time of 150 s. This selects for faster relaxing (i.e., typically more disordered)

components within the samples. This is important because it has been shown previously that SiNCs exhibit a core-shell like structure.[28] Employing solid state NMR, Thiessen *et al.* found a radial gradient between the well-ordered, crystalline SiNC center and its disordered, amorphous surface.[28] In the present study, significant amounts of SiO_2/SiO_x (*ca.* −110 ppm) are present in all cases, but only samples prepared at 1400°C and 1700°C display substantial signals indicative of Si–Si (*ca.* −80 ppm). These are not visible in composite samples prepared at 1100°C within the detection limit of the method. The larger breadth and intensity of the Si–Si region for the 1400°C, 5% H_2 composite is noteworthy and suggests that the Si–Si species are in a state of greater complexity and higher disorder. This observation echoes those reported in a recent study by Drisko and coworkers.[38]

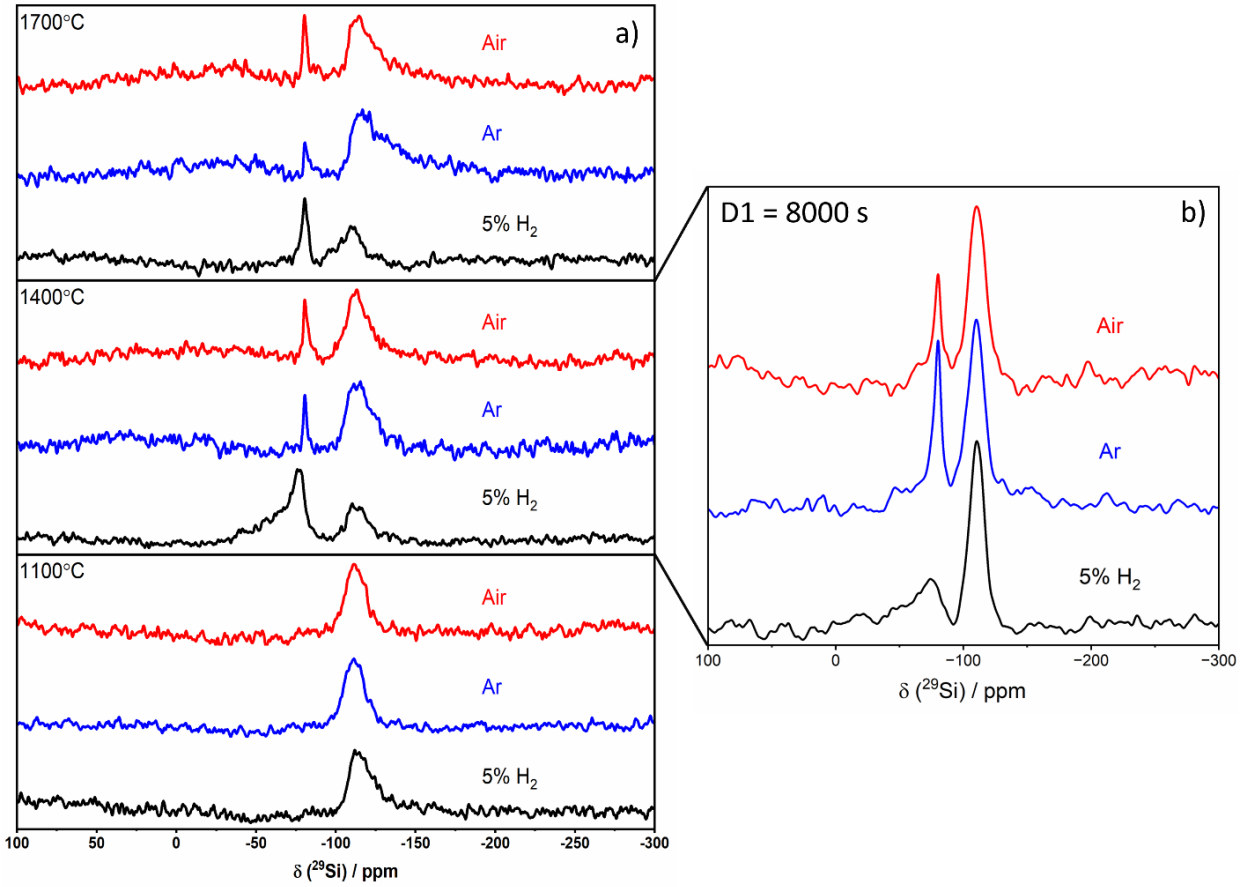

Figure 3-3. ^{29}Si MAS NMR for HSQ at various processing temperatures. Samples heated in air are shown in red; Ar in blue; and 5% H_2 / 95% Ar in black. (a) Short recycle delay (D1 = 150 s) NMR experiments select for quickly relaxing components of the composites. (b) Long recycle delay (*ca.* 1.3x $T_1 \approx 8000$ s) for 1400°C samples for full relaxation of ^{29}Si signals in the composite show large amounts of crystalline SiO_2 (*ca.* −110 ppm) for all samples with differing quantities and degree of crystallinity for Si–Si region (*ca.* −80 ppm).

To better understand the nature of the composites, ^{29}Si NMR was performed on samples processed at 1400°C using sufficiently long recycle delay times (Figure 3-3b). T_1 measurements have been performed previously for freestanding SiNCs produced at 1400°C, with T_1 relaxation times of ~230 s and >6000 s for SiNC particle surface and core regions, respectively.[28] In the present study, a saturation recovery experiment for the composite prepared at 1400°C (5% H_2 in

Ar) produced similar estimates for T_1 (data not shown), and thus a recycle delay of 8000 s was used to accommodate full relaxation of the longest-relaxing components within the composite. This data is shown in Figure 3-3(b). Unsurprisingly, the SiO_2/SiO_x region at these long relaxation times dominate the spectra regardless of processing environment. The Si–Si region is sharp and symmetric for composites prepared in air and Ar, indicative of crystalline Si. The relatively weaker signal from the composite heated in air suggests that fewer Si–Si domains are present and agrees with the XRD and XPS analysis. When hydrogen is used, the results are similar to those collected using a short recycle delay, exhibiting a broad Si–Si region. This is attributed to either an increase in amorphous Si environments, or a greater distribution of Si sites due to local disorder and strain.[38]

Taken together, these results suggest that the presence of hydrogen induces a greater fraction of amorphous and/or disordered Si to form. This is evidenced by the intensity discrepancies in the Si–Si and SiO_2/SiO_x regions for the 1400°C, 5% H_2 in Ar composite (Figure 3-2a, b). When biased towards shorter relaxing components in the composite, a greater proportion of signal arises from disordered/amorphous Si–Si, which would be expected to appear more quickly than crystalline Si possessing long T_1 values.

Scanning Electron Microscopy

The composites were imaged using scanning electron microscopy (SEM) to acquire information on surface morphology. Representative secondary electron images are presented in Figure 3-4.

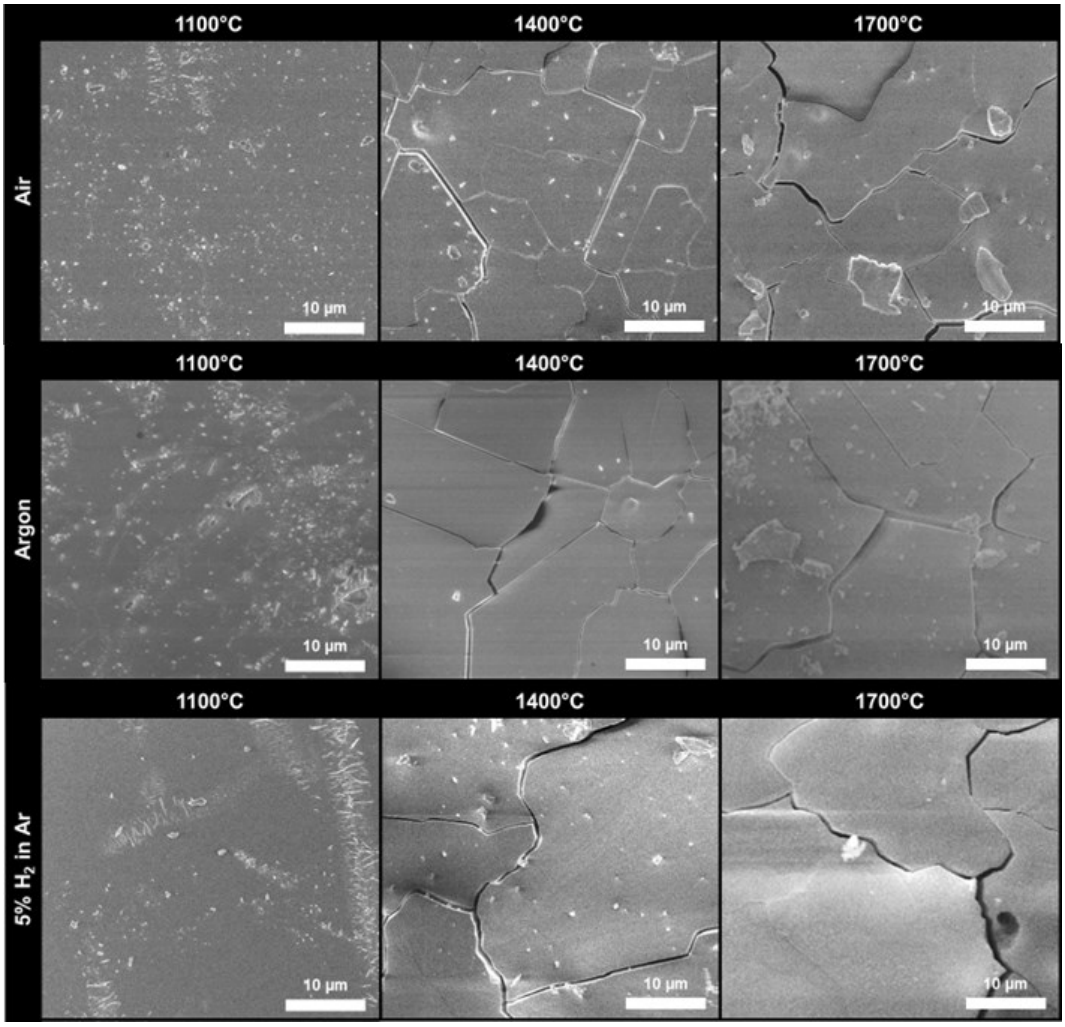

Figure 3-4. Secondary electron SEM images of the composite surfaces after thermal treatment in air, Ar, and 5% H_2 in Ar at 1100°C, 1400°C, and 1700°C.

Following thermal treatment at 1400°C and 1700°C, the surface of the composite materials fractured, forming cracked tiles (Figure 3-4). Notably, this is not observed on samples heated to 1100°C. The cracked surface is commonly observed in cristobalite crystals and is caused by strain during the transformation of high-temperature β-cristobalite to the low temperature α-cristobalite phase.[39] This observation aligns with the XRD patterns where crystalline SiO_2 reflections are observed in the composites heated to 1400°C and 1700°C but are not seen in composite heated to 1100°C. The SEM instrument is also equipped with an energy dispersive X-ray spectrometer

(EDX), but our attempts to obtain quantitative elemental analyses were fruitless due to the interference from oxygen in the sample holder.

The findings presented above, including XRD, XPS, NMR, and SEM, are consistent with previous studies employing the disproportionation reaction of HSQ for SiNC synthesis. Critically, analysis of the composite materials suggests that SiNCs can be grown from HSQ in a reducing atmosphere, an inert atmosphere, and in air. Heating in air appears to lower the SiNC yield and heating in the presence of hydrogen may introduce a greater degree of complexity and disorder to the Si–Si sites.

To better understand the nature of the SiNCs, removal of the oxide matrix with chemical etching is necessary. It is important, within the context of photoluminescence applications, to examine the effects of the annealing environment on SiNC luminescence. To this end, the remainder of this work characterizes freestanding SiNCs.

3.2.2 Characterization of the Liberated Silicon Nanocrystals

The liberation of colloidal SiNCs is accomplished by chemically etching the surrounding SiO_2 matrix with hydrofluoric acid (HF). This affords SiNCs possessing Si-H surface groups. After recovering the SiNCs from the acid mixture, the surface chemistry of the particles is modified with alkyl groups via hydrosilylation using 1-dodecene. This surface functionalization increases the SiNC solubility in non-polar organic solvents and helps limit surface oxidation. In addition, alkyl surface groups are known to improve the photoluminescence quantum yield (PLQY) of SiNCs without changing the wavelength of maximum emission (PL_{max}).

Transmission Electron Microscopy

Freestanding SiNCs formed at 1400°C and 1700°C were imaged using transmission electron microscopy (TEM) and scanning electron microscopy (SEM). This illustrates the nanoparticle morphology and provides a SiNP size analysis that is complimentary to the SiNC size estimates calculated by the Scherrer equation (Table 3-1).

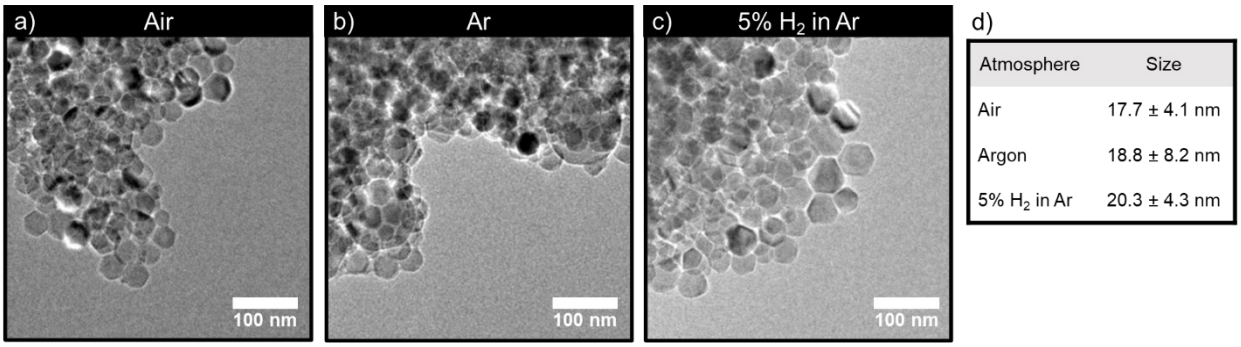

Atmosphere	Size
Air	17.7 ± 4.1 nm
Argon	18.8 ± 8.2 nm
5% H_2 in Ar	20.3 ± 4.3 nm

Figure 3-5. Transmission electron microscopy of freestanding silicon nanocrystals liberated from SiNC/SiO_2 composites by chemical etching. SiNCs were prepared by heating HSQ to 1400°C for 1 hour in air (a), Ar (b), and 5% H_2 in Ar (c). The average particle sizes are illustrated in a table (d).

At 1400°C, the measured SiNPs sizes generally align with the sizes predicted by Scherrer analysis (Table 3-1). In agreement with XRD, XPS, and NMR analysis of the composite materials, the SiNPs prepared in ambient air are smaller than those prepared in Ar and forming gas. Also seen is the larger average size of SiNPs prepared in 5% H_2 compared to those made under pure Ar. This size difference was not detected by XRD analysis; however, it is possible that the disordered Si–Si sites indicated by NMR analysis are not detectable by XRD. This suggests that SiNPs formed in 5% H_2, while larger in size, contain a greater degree of disordered/amorphous silicon such that their crystallite sizes are approximately equal to those formed in pure Ar. Given that these SiNPs

differ only by the addition of hydrogen into the annealing environment, one possible explanation for the increased disorder is the hydrogenation of the Si particles. Additionally, all SiNP samples produced at 1400°C contained particles possessing faceted edges. These morphologies have previously been reported by Yang *et al.* and their formation is driven by minimizing SiNP surface energy.[40,41] It is suggested that these morphologies are only possible when the silicon nanodomains are softened as they near the Si melting point (1414°C).[40,41]

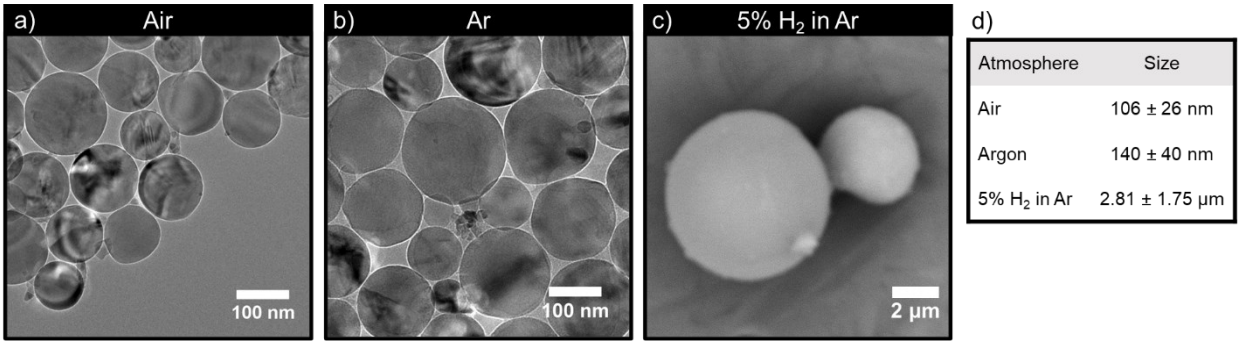

Atmosphere	Size
Air	106 ± 26 nm
Argon	140 ± 40 nm
5% H_2 in Ar	2.81 ± 1.75 µm

Figure 3-6. Transmission electron microscopy (a, b) and scanning electron microscopy (c) of freestanding silicon nanocrystals liberated from SiNC/SiO_2 composites by chemical etching. SiNCs were prepared by heating HSQ to 1700°C for 1 hour in air (a), Ar (b), and 5% H_2 in Ar (c). The average particle sizes are illustrated in a table (d).

The electron microscopy presented in Figure 3-6 compares Si particles prepared in air, Ar, and 5% H_2 in Ar at 1700°C. All three atmospheres afford spherical particles, but the difference in particle size is striking between the samples. The Si particles prepared in 5% H_2 are much larger than those prepared in Ar and air. Possessing an average size of 2.81 ± 1.75 µm, they occupy the micrometer size regime and SEM imaging was necessary to accurately capture their dimensions (Figure 3-6c). The stark size difference between Si particles prepared in the inert and reducing atmospheres at 1700°C stands in contrast to the nearly identical SiNCs prepared at 1100°C and 1400°C. This suggests that the effect of the reducing atmosphere becomes highly influential at

high temperatures. In a similar study, Cibaka-Ndaya *et al.* compared SiNCs grown in Ar and 5% H_2 in Ar using XRD, NMR, and Raman spectroscopy.[38] In agreement with the present results, the authors noted a greater degree of Si segregation in composites formed in the reducing atmosphere. Additionally, Cibaka-Ndaya and colleagues observed a novel mechanism for SiNPs involving a high mobility, high malleability nanoparticle phase.[38] Interestingly, this behavior was only observed when the nanoparticles were subject to a mixture of 5% H_2 in N_2. While these experiments were conducted at a relatively lower temperature (1200–1300°C), it is possible that the inclusion of hydrogen in the processing atmosphere encourages Si nanoparticle mobility within the composite matrix.

The sizes of SiNPs prepared in air and pure argon are 106 ± 26 nm and 140 ± 40 nm, respectively (Figure 3-6a, b). This finding aligns with the conclusions drawn from XRD, NMR, and XPS analyses of the composite materials; SiNCs prepared in air are smaller than those prepared in Ar. In addition, each sample heated to 1700°C possessed a wide size distribution, and a positive correlation was found between average particle size and size polydispersity. This observation is in agreement with previous reports on SiNC synthesis from HSQ.[28, 31]

Photoluminescence

The luminescent properties of the dodecyl-functionalized SiNCs are summarized and compared in Figure 3-7. All SiNCs exhibited characteristic, featureless UV-vis absorption spectra between 300 to 500 nm (Figure 3-7a, inset). SiNCs liberated from HSQ processed in Ar and forming gas exhibited characteristic photoluminescence (PL) from the nanoparticle core with similar emission maxima centered at 725 nm and PL lifetimes around 135 $\pm$ 7 μs. Both emissions tail into the longer wavelengths, possibly due to a wider distribution in SiNC sizes. In contrast, the PL emission from SiNCs liberated from composites heated under air has a PL maximum at 680 nm and an average

lifetime of 91 μs. Based on the XRD, XPS, and NMR analyses (Figures 3-1, 3-2, 3-3), we know that the silicon nanocrystallite sizes from composites produced in air are relatively smaller than those produced in Ar and 5% H_2. The smaller SiNC size can explain, in part, why the PL of SiNCs prepared in air is blue-shifted and exhibits a shorter lifetime.[26]

In contrast to the differing PL_{max}, the impact of the processing conditions on the photoluminescence quantum yield (PLQY) is minimal (Figure 3-7b). The SiNCs exhibit PLQYs ranging between 21–33%; all within a reasonable range of PLQY normally observed from SiNCs functionalized using thermally-induced hydrosilylation.[7] The slightly lower PLQY from the SiNCs prepared in air can be ascribed to the smaller size of the SiNCs.[26] Critically, the PLQY of SiNCs heated in pure Ar is slightly greater than those produced in 5% hydrogen. This observation disagrees with the literature concerning PL from oxide-embedded SiNCs; however, this is not surprising given the differences between SiNCs passivated by SiO_2 and those terminated in alkyl ligands.[17–24] The defects and trap states induced by the Si–SiO_2 interface are effectively eliminated when the SiNCs are freed from the oxide matrix and modified with surface ligands. The liberation and functionalization of SiNCs not only creates Si–C surface bonds, but can also inadvertently introduce a varying degree of surface oxidation and disorder.[42] This surface oxidation occurs during the surface modification and/or subsequent purification of the colloidal SiNCs and is not affected by the atmosphere used during heating of the HSQ. In summary, the PL data suggests that using a reducing atmosphere of 5% H_2 gives no benefits to the PL of colloidal SiNCs prepared from thermal treatment of HSQ. In fact, processing in air provides a narrower PL emission (smaller FWHM) and may be beneficial for photoluminescence applications.[43]

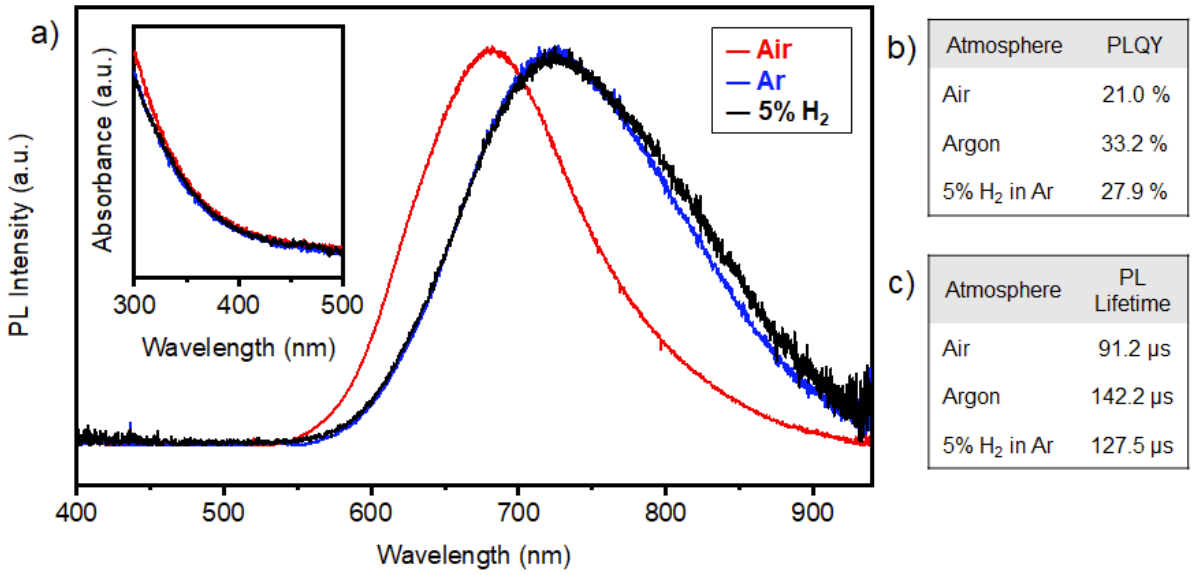

Atmosphere	PLQY
Air	21.0 %
Argon	33.2 %
5% H_2 in Ar	27.9 %

Atmosphere	PL Lifetime
Air	91.2 µs
Argon	142.2 µs
5% H_2 in Ar	127.5 µs

Figure 3-7. Photoluminescence (PL) of silicon nanocrystals formed in air (red), argon (blue), and 5% H_2 in Ar (black) at 1100°C. The PL emission spectrum (a) with accompanying absorption spectrum (a, inset). The photoluminescence quantum yield (PLQY) is presented in a table (b), alongside the photoluminescence lifetime measurements (c). All measurements are performed on SiNCs suspended in toluene.

X-Ray Photoelectron Spectroscopy

While interpreting the PL spectra of the SiNCs, is it useful to know the oxidation states of silicon within the colloidal SiNCs. In a similar manner as before, the oxidation states are measured using XPS (Figure 3-8). Although great care was taken to minimize any differences in the reaction and purification conditions of the three samples, we cannot fully eliminate the effects of the post-etching environments on SiNC surface oxidation. For this reason, differences in the oxidation state distribution of the colloidal SiNCs cannot be solely attributed to the heating environment. In fact, given the presumed elimination of all Si(IV) sites during HF etching, differences between the

samples are most likely due to small differences in particle surface modification and purification. Regardless, these spectra help explain the PL properties of the three SiNC samples.

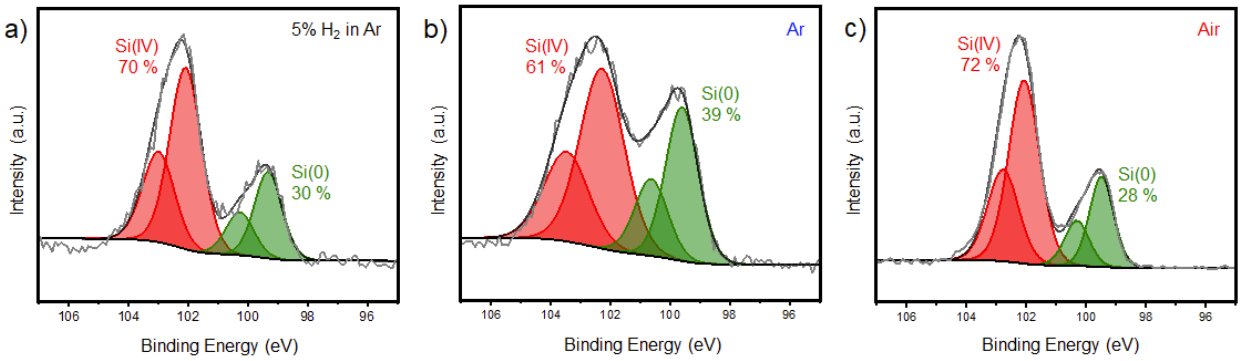

Figure 3-8. X-ray photoelectron spectroscopy of SiNCs formed at 1100°C. Particles were produced in a flow of 5% H_2 (a), Ar (b), and air (c). Red peaks fit the Si(IV) sites, green peaks fit the Si(0) sites. Multiple peaks are required due to spin orbit splitting from the Si 2p orbitals ($2p_{1/2}$, $2p_{3/2}$). Area integration of the peak fittings gives compositional information expressed in atomic percent.

A comparison of the SiNC samples shows a similar degree of oxidation in the SiNCs prepared in 5% H_2 and air while SiNCs prepared in Ar possess a relatively lower degree of oxidation (Figure 3-8). This is consistent with the lifetime measurements as the greater degree of oxide sites can provide faster exciton relaxation pathways through trap states (Figure 3-7c). This may also explain why the SiNCs prepared in Ar exhibit a relatively higher PLQY as surface oxidation can also introduce defects that promote non-radiative decay.[44–46] Given the similarity in SiNC size for particles prepared under Ar and 5% H_2, we stress that differences in the PL properties most likely arise from differing amounts of surface oxidation.

3.3 Conclusions

Using the thermally-induced disproportionation of HSQ, silicon nanocrystals were prepared in air, argon, and forming gas. Despite lowered Si(0) yield and SiNC size, the quantum dots synthesized in air exhibited a photoluminescence quantum yield of 21%. In addition, we found no benefit to the photoluminescence of colloidal SiNCs when a reducing atmosphere was used during thermal treatment. At 1700°C, the effect of the reducing atmosphere became prominent, producing micron-sized Si particles.

3.4 Experimental

Materials

Fuming sulfuric acid (reagent grade, 20% free SO_3 bases), trichlorosilane (99%), and toluene (HPLC grade), were purchased from MilliporeSigma. Hydrofluoric acid (electronic grade, 48−50%) and sulfuric acid (reagent grade, 95−98%) were purchased from Fisher Scientific. Dry toluene was obtained from a Pure-Solv purification system with N_2 as the operating gas. The remaining reagents and solvents were used as received.

Synthesis of Hydrogen Silsesquioxane (HSQ)

HSQ was synthesized using an adapted literature procedure.[47] On an Ar-charged Schlenk line, concentrated sulfuric acid (70 mL) and fuming sulfuric acid (32 mL) were mixed in a 2 L RBF. Dry toluene (200 mL) was added dropwise over 2 hours, followed by a solution of trichlorosilane (70 mL) in dry toluene (500 mL), added dropwise over 5 hours. Both additions occured with

vigorous stirring from a Teflon magnetic stirring bar. The mixture was decanted into a separatory funnel where the toluene layer was isolated and then washed three times with a solution of aqueous sulfuric acid (1.2 L H_2O, 0.4 L H_2SO_4). The washed organic layer was dried and neutralized over $MgSO_4$ and $CaCO_3$ for 24 hours. Solvent reduction using a rotary evaporator followed by a final evaporation in vacuo yielded a white solid that is stored under vacuum until use.

Synthesis of Oxide-embedded Silicon Nanocrystals (*"The Composite"*)

HSQ (2 g) was transferred into a yttria-stabilised zirconia boat and loaded into a Carbolite CTF 18/300 tube furnace equipped with an alumina tube. The ends of the tube were fitted with gas adaptors. When needed, argon (100% Ar) or forming gas (5% H_2 / 95 % Ar) was flowed through the tube and out of a bubbler. The furnace heated at a ramp rate of 5°C/min to the selected processing temperature (i.e., 1100°C, 1400°C, or 1700°C). This temperature held (dwelled) for 1 hour. The furnace then cooled at 10°C/min to room temperature. This yielded a silicon dioxide matrix containing crystalline Si nanoparticles (*"the composite"*). If powdered samples were required, this composite is ground by hand using an agate mortar and pestle.

Liberation of Colloidal Silicon Nanocrystals and Subsequent Surface Modification

In a plastic beaker, powdered composite (0.5 g) was stirred in a mixture of ethanol (5 mL), water (5 mL), and hydrofluoric acid (HF 50% in water, 5 mL) using a Teflon magnetic stirring bar. **Caution**: HF is a dangerous reagent and extreme care must be taken when handling. After 1 hour, the nanocrystals were removed from the beaker as a colloidal suspension using toluene in a liquid-liquid extraction. The nanocrystals were separated from the toluene using centrifugation (5 min at 5,000 rpm), then redispersed in toluene and centrifuged again. This process was repeated once more to remove any residual HF or impurities from the chemical etching procedure. On an Ar-

charged Schlenk line, the modification of the nanocrystal surface was accomplished by thermally-induced hydrosilylation using neat 1-dodecene (10 mL) at 160°C for 24 hours.

Powder X-ray Diffraction (XRD)

Powered composite was analyzed on a zero-background silicon substrate using a Bruker D8 Advance powder diffractometer. The instrument was equipped with a SSD160 detector and a Cu radiation source ($K_{\alpha 1}$ = 1.54056 Å; $K_{\alpha 2}$ removed) operating at 40 kV and 40 mA. The amount of powder loaded onto the diffraction plate was consistent between samples and the resulting diffraction patterns were not normalized unless otherwise specified (1100°C samples).

SiNC Size Determination

The sizes of oxide-embedded SiNCs within the composite were estimated using the Scherrer equation. Background-subtracted diffractograms were plotted using fityk v.1.3.1 and the characteristic silicon (111), (200), and (311) reflections were each matched with a Lorentz function.[48] The peak shapes were then refined using the Levenberg-Marquardt method to minimize the weighted sum of squared residuals. The resulting peak centers FWHM values from each reflection were used to determine the crystallite size via the Scherrer equation; the reported SiNC size is an average of these. A shape factor (K) of 0.9 and an X-ray wavelength of 1.54056 Å were used in all calculations.

Scherrer equation: $$\tau = \frac{K\lambda}{\beta \cos\theta}$$

X-ray Photoelectron Spectroscopy (XPS)

X-ray photoelectron spectra were collected using a Kratos Axis 165 Ultra X-ray Photoelectron Spectrometer equipped with a monochromatic Al K_{α} radiation source (1486.6 eV) operating at 210

W. High-resolution spectra were measured using an analyzer pass energy of 20 eV and a step of 0.1 eV. For survey spectra, a pass energy of 160 eV and a step of 0.5 eV were used. Spectra were calibrated to C 1s 284.8 eV using adventitious carbon. Composites were powdered before analysis, silicon nanocrystals were drop casted onto copper foil before analysis.

Solid-state Nuclear Magnetic Resonance (NMR)

^{29}Si NMR spectroscopy was carried out on a Bruker Avance III HD 400 NMR spectrometer (B_0 = 9.4 T) equipped with a 4 mm double-resonance (H/X) Bruker magic-angle spinning (MAS) probe. ~90-140 mg of sample were packed into a 4mm zirconia rotor and spun at 14 kHz about the magic angle for all experiments. MAS spectra were acquired at natural abundance using a ^{1}H TPPM-decoupled single-pulse experiment with 4 us $\pi/2$ pulse (ν_{rf} = 62.5 kHz). Experiments were performed using a short recycle delay (D1 = 150 s) with 256 scans and a long recycle delay (where D1 $\approx 1.3T_1$ = 8000 s for the longest estimated T_1 site via saturation recovery experiment) with 32 scans. ^{29}Si spectra were referenced to a secondary standard with respect to TMS ($\delta(^{29}Si) = 0.000$) by setting the high frequency peak of tetrakistrimethylsilylsilane to −9.843 ppm.[49] T_1 data were processed using the Dyanmics Centre application within TopSpin 4.2.0 using a monoexponential saturation recovery fitting model. NMR data were processed within Topspin 4.2.0 using 100 Hz (D1 = 150 s) or 400 Hz (8000s D1) Lorentizan broadening.

Scanning Electron Microscopy (SEM)

A Hitachi S4800 FESEM (Hitachi, Tokyo, Japan) equipped with a cold field emission gun and operated with an accelerating voltage of 5 kV was used to obtain images of the composite materials. Samples were mounted onto double-sided carbon tape on aluminum stubs. Gold sputtering (~10 nm) was used to avoid sample charging. All images were recorded using secondary electron (SE) imaging.

Photoluminescence Measurements

Optical characterization of all SiQD toluene suspensions (ca. 2.5 mL) was performed in a quartz cuvette (1 cm x 1 cm). Photoluminescence (PL) spectra were acquired by exciting samples using the combined 351 and 364 nm lines of an argon ion laser (40 mW) and collecting the emission using an optic fiber connected to an Ocean Optics USB 2000+ Spectrometer. A 475 nm long-pass filter (LPF) was used to eliminate scattered light from the excitation source. The spectral response was calibrated using a blackbody radiator. Time-resolved PL (PL lifetime) measurements were acquired using the same laser (80 mW) interfaced to an acoustic-optic modulator (50 ns response time, 203.621 μs) operated at a frequency of 200 Hz with a 8% duty cycle. The PL was captured by an optic fiber, sent through a 500 nm long-pass filter, and counted by a Hamamatsu H7422P-50 photomultiplier tube (PMT) interfaced with a Becker-Hickl PMS-400A gated photon counter. The data was collected without wavelength selection and used 1 μs time steps. The mean PL decay lifetimes were found by fitting the data using a log-normal lifetime distribution function.[42, 50] UV-vis absorption spectra were measured using the Ocean Optics USB 2000+ spectrometer with a MINI-D2T Deuterium Tungsten light source (λ_{ex} = 200 – 1000 nm).

Absolute PL quantum yield (PLQY) measurements were performed using an integrating sphere with a 365 nm light-emitting diode excitation source. Solutions were diluted to have an absorbance ca. 0.096 at 365 nm. The PL and excitation intensities were measured through an optical fiber and analyzed with an Ocean Optics 2000+ spectrometer using a NIST-calibrated light source for absolute irradiance measurements. The measurements were done in triplicate.

Transmission Electron Microscopy (TEM)

Transmission electron microscopy bright field images were acquired using a JEOL JEM-ARM200CF S/TEM electron microscope at an accelerating voltage of 200 kV. TEM samples were prepared by depositing a drop of a dilute toluene suspension of the desired dodecyl-SiNPs onto an ultra-thin carbon coated copper grid (Electron Microscopy Inc.). The grid bearing the sample was kept in a vacuum chamber at 0.2 bar for at least 12 h prior to data collection. Images were analysed using ImageJ. A population of at least 300 particles were counted when calculating average nanoparticle size and standard deviation.[51]

3.5 References

1. Baldwin, R. K.; Pettigrew, K. A.; Ratai, E.; Augustine, M. P.; Kauzlarich, S. M. Solution Reduction Synthesis of Surface Stabilized Silicon Nanoparticles. *Chem. Commun.* **2002**, *17*, 1822–1823.
2. Adachi, M.; Sugimoto, H.; Nishimura, Y.; Morita, K.; Ogino, C.; Fujii, M. Fluorophore-Decorated Mie Resonant Silicon Nanosphere for Scattering/Fluorescence Dual-Mode Imaging. *Small* **2023**, *19*, 2207318.
3. Slootman, F.; Parent, J.-C. Homogeneous Gas-Phase Nucleation in Silane Pyrolysis. *J. Aerosol Sci.* **1994**, *25*, 15–21.
4. Eslamisaray, M. A.; Wray, P.; Lee, Y.; Nelson, G. M.; Ilic, O.; Atwater, H. A.; Kortshagen, U. R. A Single-Step Bottom-up Approach for Synthesis of Highly Uniform Mie-Resonant Crystalline Semiconductor Particles at Visible Wavelengths. *Nano Lett.* **2023**, *23*, 1930–1937.
5. McVey, B. F. P.; Butkus, J.; Halpert, J. E.; Hodgkiss, J. M.; Tilley, R. D. Solution Synthesis and Optical Properties of Transition-Metal-Doped Silicon Nanocrystals. *J. Phys. Chem. Lett.* **2015**, *6*, 1573–1576.

6. Zhang, P.; Duan, J.; Chen, G.; Li, J.; Wang, W. Production of Polycrystalline Silicon from Silane Pyrolysis: A Review of Fines Formation. *Sol. Energy* **2018**, *175*, 44–53.
7. Milliken, S.; Thiessen, A. N.; Cheong, I. T.; O'Connor, K. M.; Li, Z.; Hooper, R. W.; Robidillo, C. J. T.; Veinot, J. G. C. "Turning the Dials": Controlling Synthesis, Structure, Composition, and Surface Chemistry to Tailor Silicon Nanoparticle Properties. *Nanoscale* **2021**, *13*, 16379–16404.
8. Rodríguez Núñez, J. R. Commentary: Silicon Nanocrystals and Their Role in Photonics. *J. Nanophotonics* **2012**, *6*, 060302.
9. Sun, W.; Qian, C.; Cui, X. S.; Wang, L.; Wei, M.; Casillas, G.; Helmy, A. S.; Ozin, G. A. Silicon Monoxide – a Convenient Precursor for Large Scale Synthesis of near Infrared Emitting Monodisperse Silicon Nanocrystals. *Nanoscale* **2016**, *8*, 3678–3684.
10. Hessel, C. M.; Henderson, E.; Veinot, J. G. C.. Hydrogen Silsesquioxane: A Molecular Precursor for Nanocrystalline Si−SiO_2 Composites and Freestanding Hydride-Surface-Terminated Silicon Nanoparticles. *Chem. Mater.* **2006**, *18*, 6139–6146.
11. Hessel, C. M.; Henderson, E. J.; Veinot, J. G. C. An Investigation of the Formation and Growth of Oxide-Embedded Silicon Nanocrystals in Hydrogen Silsesquioxane-Derived Nanocomposites. *J. Phys. Chem. C* **2007**, *111*, 6956–6961.
12. Meldrum, A.; Hryciw, A. C.; A. Nicole MacDonald; Blois, C.; Marsh, K. L.; Wang, J.; Li, Q. Photoluminescence in the Silicon-Oxygen System. *J. Vac. Sci. Technol., A* **2006**, *24*, 713–717.
13. Kelly, J. A.; Henderson, E. J.; Clark, R. J.; Hessel, C. M.; Cavell, R. G.; Veinot, J. G. C. X-Ray Absorption Spectroscopy of Functionalized Silicon Nanocrystals. *J. Phys. Chem. C* **2010**, *114*, 22519–22525.
14. Rodríguez Núñez, J. R.; Kelly, J. A.; Henderson, E. J.; Veinot, J. G. C. Wavelength-Controlled Etching of Silicon Nanocrystals. *Chem. Mater.* **2012**, *24*, 346–352.
15. Terada, S.; Xin, Y.; Saitow, K. Cost-Effective Synthesis of Silicon Quantum Dots. *Chem. Mater.* **2020**, *32*, 8382–8392.
16. Zhang, M.; Poumirol, J.-M.; Chery, N.; Rinnert, H.; Giba, A. E.; Demoulin, R.; Talbot, E.; Cristiano, F.; Hungria, T.; Paillard, V.; Gourbilleau, F.; Bonafos, C. Hyperdoped Si Nanocrystals Embedded in Silica for Infrared Plasmonics. *Nanoscale* **2023**, *15*, 7438–7449.

17. Neufeld, E.; Wang, S.; Apetz, R.; Buchal, C.; Carius, R.; White, C. W.; Thomas, D. K. Effect of Annealing and H_2 Passivation on the Photoluminescence of Si Nanocrystals in SiO_2. *Thin Solid Films* **1997**, *294*, 238–241.
18. Withrow, S. P.; White, C. W.; Meldrum, A.; Budai, J. D.; Hembree, D. M.; Barbour, J. C. Effects of Hydrogen in the Annealing Environment on Photoluminescence from Si Nanoparticles in SiO2. *J. Appl. Phys.* **1999**, *86*, 396–401.
19. Wilkinson, A. R.; Elliman, R. G. The Effect of Annealing Environment on the Luminescence of Silicon Nanocrystals in Silica. *J. Appl. Phys* **2004**, *96*, 4018–4020.
20. S. Cheylan; Elliman, R. G. Effect of Hydrogen on the Photoluminescence of Si Nanocrystals Embedded in a SiO2 Matrix. *Appl. Phys. Lett.* **2001**, *78*, 1225–1227.
21. Ikeda, M.; Nakagawa, M.; Mitsusue, R.; Kondo, S.; N. Imanishi. Hydrogen Behavior in SiO2 with High Density of Defects and Locally Concentrated Silicon. *J. Appl. Phys.* **2004**, *95*, 4655–4661.
22. Godefroo, S.; Hayne, M.; Mihaela Jivanescu; Stesmans, A.; Zacharias, M.; Lebedev, O. I.; van Tendeloo, G.; Moshchalkov, V. Classification and Control of the Origin of Photoluminescence from Si Nanocrystals. *Nat. Nanotechnol.* **2008**, *3*, 174–178.
23. Borrero-González, L. J.; Nunes, L. A.; Marcello; Wójcik, J.; Mascher, P.; Pusep, Y. A.; Comedi, D.; Eduardo, F. The Role of Quantum Confinement and Crystalline Structure on Excitonic Lifetimes in Silicon Nanoclusters. *J. Appl. Phys.* **2010**, *108*, 013105.
24. Li, Y.; Liang, P.; Hu, Z.; Guo, S.; You, Q.; Sun, J.; Xu, N.; Wu, J. Enhancement and Stability of Photoluminescence from Si Nanocrystals Embedded in a SiO2 Matrix by H2-Passivation. *Appl. Surf. Sci.* **2014**, *300*, 178–183.
25. Thiessen, A.; Zhang, L.; Oliynyk, A. O.; Yu, H.; O'Connor, K.; Meldrum, A.; Veinot, J. G. C. A Tale of Seemingly "Identical" Silicon Quantum Dot Families: Structural Insight into Silicon Quantum Dot Photoluminescence. *Chem. Mater.* **2020**, *32*, 6838–6846.
26. Yu, Y.; Fan, G.; Fermi, A.; Mazzaro, R.; Morandi, V.; Ceroni, P.; Detlef-M. Smilgies; Korgel, B. A. Size-Dependent Photoluminescence Efficiency of Silicon Nanocrystal Quantum Dots. *J. Phys. Chem. C* **2017**, *121*, 23240–23248.
27. Aghajamali, M.; Xie, H.; Javadi, M.; W.; Kalisvaart, P.; Buriak, J. M.; Veinot, J. G. C. Size and Surface Effects of Silicon Nanocrystals in Graphene Aerogel Composite Anodes for Lithium Ion Batteries. *Chem. Mater.* **2018**, *30*, 7782–7792.

28. Thiessen, A. N.; Ha, M.; Hooper, R. W.; Yu, H.; Oliynyk, A. O.; Veinot, J. G. C.; Michaelis, V. K. Silicon Nanoparticles: Are They Crystalline from the Core to the Surface? *Chem. Mater.* **2019**, *31*, 678–688.
29. Tsai, H.-Y.; Robidillo, C. J. T.; Matharu, G. K.; O'Connor, K.; Cheong, I. T.; Ni, C.; Veinot, J. G. C.; Algar, W. R. Spectrotemporal Characterization of Photoluminescent Silicon Nanocrystals and Their Energy Transfer to Dyes. *Nanoscale* **2023**, *15*, 12492–12505.
30. Hessel, C. M.; Reid, D. K.; Panthani, M. G.; Rasch, M.; Goodfellow, B. W.; Wei, J.; Fujii, H.; Akhavan, V. A.; Korgel, B. A. Synthesis of Ligand-Stabilized Silicon Nanocrystals with Size-Dependent Photoluminescence Spanning Visible to Near-Infrared Wavelengths. *Chem. Mater.* **2011**, *24*, 393–401.
31. O'Connor, K.; Rubletz, A.; Ni, C.; He, Y.; Butler, C.; Veinot, J. G. C. High-Temperature Anomaly in the Synthesis of Large (D > 100 nm) Silicon Nanoparticles from Hydrogen Silsesquioxane. *Chem. Mater.* **2023**, *35*, 7967–7973.
32. Hom, T.; Kiszenik, W.; Post, B. Accurate lattice constants from multiple reflection mesurements II. Lattice constants of germanium, silicon and diamond. *J. Appl. Crystallogr*. **1975**, *8*, 457–458.
33. Downs, R. T.; Palmer, D. C. The pressure behavior of alpha cristobalite. *Am. Mineral*. **1994**, *79*, 9–14.
34. Heya, A.; Masuda, A.; Matsumura, H. Mechanism of Low-Temperature Crystallization of Amorphous Silicon by Atomic Hydrogen Anneal. *J. Non-Cryst. Solids* **2000**, *266–269*, 619–623.
35. Hanrahan, M. P.; Fought, E. L.; Windus, T. L.; Wheeler, L. M.; Anderson, N. C.; Neale, N. R.; Rossini, A. J. Characterization of Silicon Nanocrystal Surfaces by Multidimensional Solid-State NMR Spectroscopy. *Chem. Mater.* **2017**, *29*, 10339–10351.
36. Dorn, R. W.; Ryan, B. J.; Lamahewage, S. N. S.; Dodson, M. V.; Essner, J. B.; Biswas, R.; Panthani, M. G.; Rossini, A. J. Chlorination of Hydrogenated Silicon Nanosheets Revealed by Solid-State Nuclear Magnetic Resonance Spectroscopy. *Chem. Mater.* **2023**, *35*, 539–548.
37. Ha, M.; Thiessen, A. N.; Sergeyev, I. V.; Veinot, J. G. C.; Michaelis, V. K. Endogenous Dynamic Nuclear Polarization NMR of Hydride-Terminated Silicon Nanoparticles. *Solid State Nucl. Magn. Reson.* **2019**, *100*, 77–84.

38. Cibaka-Ndaya, C.; O'Connor, K.; Idowu, E. O.; Parker, M. A.; Lebraud, É.; Lacomme, S.; Montero, D.; Camacho, P. S.; Veinot, J. G. C.; Roiban, I. L.; Drisko, G. L. Understanding the Formation Mechanisms of Silicon Particles from the Thermal Disproportionation of Hydrogen Silsesquioxane. *Chem Mater.* **2023**, *35*, 8551–8560.
39. Deer, W. A. *Rock-Forming Minerals, Vol. 4B: Framework Silicates - Silica Minerals, Feldspathoids and Zeolites*, 2nd edition.; Howie, R. A., Wise, W. S., Zussman, J., Eds.; Geological Society of London: London, 2006.
40. Yang, Z.; Dobbie, A. R.; Cui, K.; Veinot, J. G. C. A Convenient Method for Preparing Alkyl-Functionalized Silicon Nanocubes. *J. Am. Chem. Soc.* **2012**, *134*, 13958–13961.
41. Yang, Z.; Dobbie, A. R.; Veinot, J. G. C. Shape Evolution of Faceted Silicon Nanocrystals upon Thermal Annealing in an Oxide Matrix. *MRS Online Proc. Lib.* **2013**, *1536*, 207–212.
42. Sinelnikov, R.; Dasog, M.; Beamish, J.; Meldrum, A.; Veinot, J. G. C. Revisiting an Ongoing Debate: What Role Do Surface Groups Play in Silicon Nanocrystal Photoluminescence? *ACS Photonics* **2017**, *4*, 1920–1929.
43. Cheong, I. T.; Mock, J.; Kallergi, M.; Groß, E.; Meldrum, A.; Rieger, B.; Becherer, M.; Veinot, J. G. C. Colloidal Silicon Quantum Dot-Based Cavity Light-Emitting Diodes with Narrowed and Tunable Electroluminescence. *Adv. Opt. Mater.* **2023**, *11*, 2201834.
44. Mastronardi, M. L.; Chen, K. K.; Liao, K.; Casillas, G.; Ozin, G. A. Size-Dependent Chemical Reactivity of Silicon Nanocrystals with Water and Oxygen. *J. Phys. Chem. C* **2014**, *119*, 826–834.
45. Pereira, R. N.; Rowe, D. J.; Anthony, R. J.; Kortshagen, U. Oxidation of Freestanding Silicon Nanocrystals Probed with Electron Spin Resonance of Interfacial Dangling Bonds. *Phys. Rev. B* **2011**, *83*, 155327.
46. Rinck, J.; Schray, D.; Kübel, C.; Powell, A. K.; Ozin, G. A. Silicon Nanocrystals: Size-Dependent Oxidation of Monodisperse Silicon Nanocrystals with Allylphenylsulfide Surfaces. *Small* **2015**, *11*, 262–262.
47. Frye, C. L.; Collins, W. T. Oligomeric Silsesquioxanes, $(HSiO_{3/2})n$. *J. Am. Chem. Soc.* **1970**, *92*, 5586–5588.
48. Wojdyr, M. Fityk: A General-Purpose Peak Fitting Program. *J. Appl. Crystallogr.* **2010**, *43*, 1126–1128.

49. Hayashi, S.; Hayamizu, K. Chemical Shift Standards in High-Resolution Solid-State NMR ^{13}C, ^{29}Si, and ^{1}H Nuclei. *Bull. Chem. Soc. Jpn.* **1991**, *64*, 685– 687.

50. Driel, A. F.; Nikolaev, I. S.; Vergeer, P.; Lodahl, P.; Vanmaekelbergh, D.; Vos, W. L. Statistical Analysis of Time-Resolved Emission from Ensembles of Semiconductor Quantum Dots: Interpretation of Exponential Decay Models. *Phys. Rev. B* **2007**, *75*, 035329.

51. Murphy, C. J.; Buriak, J. M. Best Practices for the Reporting of Colloidal Inorganic Nanomaterials. *Chem. Mater.* **2015**, *27*, 4911–4913.

Chapter 4

Conclusions and Future Directions

4.1 Conclusions

From lithography to the preparation of nanomaterials, hydrogen silsesquioxane (HSQ) is a useful polymer for academia and industry alike. This work highlights the continued utility of HSQ by pushing the boundaries of silicon nanocrystal synthesis from thermal decomposition of HSQ. Chapter 2 explored new territory by thermally disproportionating HSQ at record-high temperatures. Along the way, new insights into the effects of silicon monoxide were gained. In Chapter 3, the established procedures for silicon-rich oxide annealing were questioned, and the influence of various reaction parameters was analyzed.

Since the discovery of photoluminescence from oxide-embedded Si nanocrystals, the number of applications incorporating silicon nanoparticles has grown substantially. The unique properties of nanoscale silicon, combined with its biocompatibility and natural abundance, has fueled countless academic and commercial endeavours to explore new avenues of opportunity for the material. Among these, metamaterials stand out because they require particles spanning hundreds of nanometers in diameter. This stands in contrast to the sub-10 nm silicon nanocrystals used for photoluminescence. While HSQ is known to provide high-quality sub-10 nm silicon nanocrystals, it was unknown if it could provide particles spanning the 75 to 200 nm range. Chapter 3 documents our efforts to produce these relatively large silicon nanocrystals.

For decades, researchers have prepared silicon nanoparticles by subjecting silicon-rich oxides to high temperatures. This thermal treatment encourages the nucleation, growth, and/or annealing of crystalline Si nano-domains embedded within a matrix of SiO_2. While it is often assumed that the resulting Si–SiO_2 interface is unreactive, sufficiently high temperatures can promote the reduction of SiO_2 by Si to produce SiO gas. Silicon monoxide prepared in this way has been used as a precursor for silicon nanowires synthesis, but there was no systematic examination of the reaction parameters necessary to evolve $SiO_{(g)}$. After discovering Si-based nanowires in the furnace tube, we explored $SiO_{(g)}$ evolution using predefined mixtures of elemental silicon and silica powders as a model system for HSQ annealing. Using crystalline SiO_2, this system demonstrated the onset of detectable Si transport occurred at temperatures as low as 1200°C. When systems containing amorphous SiO_2 were heated they resisted substantial $SiO_{(g)}$ evolution until the silica crystallized. These trends recurred when HSQ was heated to similar temperatures. Additionally, the synthesis of *large* (d > 100 nm) silicon nanoparticles was achieved using a processing temperature of 1700°C. While this reaction temperature was more than sufficient to promote $SiO_{(g)}$ formation, the loss of crystalline SiO_2 suppressed its evolution.

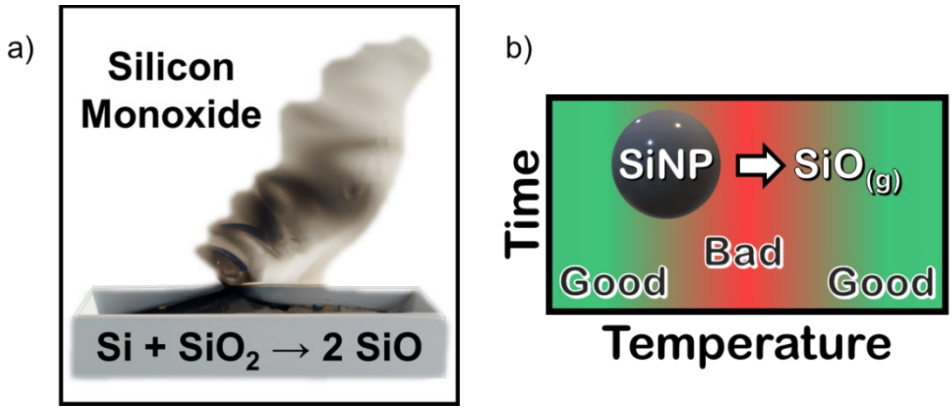

Figure 4-1. The silicon monoxide evolution reaction and its role during HSQ thermal treatment. The HSQ system was modeled using a mixture of Si and SiO_2 powders to study $SiO_{(g)}$ (a). The evolution of SiO from HSQ tracked as a function of reaction temperature and time (b).

The first researchers to produce colloidal silicon nanocrystals (SiNCs) from silicon-rich oxides based many of their experimental procedures on literature established using thin-films. Following this precedent, subsequent publications employing Si-rich oxide disproportionation for the synthesis of colloidal SiNC continue to use the reaction conditions established nearly two decades ago. In Chapter 3, the role of the processing atmosphere was examined using solid-state NMR, XRD, and XPS of the oxide-embedded SiNC composites. In addition, the SiNCs were liberated and their surface was modified with alkane groups for photoluminescence measurements and morphology characterization. An analysis of the photoluminescence found no benefit from the use of hydrogen in the processing atmosphere. Indeed, the use of hydrogen may increase the disorder of low valent Si sites. In addition, the study demonstrated the possibility of SiNC synthesis in ambient air. Despite a reduction in yield, the silicon nanoparticles retained their crystallinity and displayed a photoluminescence quantum yield over 20%.

4.2 Future Directions

4.2.1 Silicon Nanocrystal Growth Mechanisms in HSQ

We recently published a study in collaboration with the Drisko team (University of Bordeaux) on the growth mechanisms of silicon nanoparticles during thermal disproportionation of HSQ.[1] Using an environmental transmission electron microscope (ETEM), *in situ* imaging of the HSQ and silicon nanoparticles was performed at temperatures up to 1300°C. The study revealed a new displacement growth mechanism reminiscent of a liquid droplet moving through a confined space. A trace was observed in the wake of these highly malleable Si nanoparticles suggesting that an interfacial chemical reaction occurs between the particle surface and surrounding matrix,

possibly adding Si(0) atoms to the nanoparticle.[1] Rapid coalescence of neighboring nanoparticles was also observed. These results suggest that the growth of Si nanoparticles in HSQ might differ depending on the phase (solid or liquid) of the silicon particles. This is consistent with the trend in SiNC sizes prepared below the melting point of silicon (< 10 nm) compared to those prepared above the melting point (> 100 nm). The bulk melting point of Si is ~1410°C but nanomaterials are known to melt at temperatures lower than bulk domains.[2]

To investigate this liquid-like growth mechanism we introduced germanium nanoparticles (GeNPs) into HSQ. While thermal treatment of HSQ at 1100°C normally yields SiNCs ~3 nm in diameter, heating the GeNP/HSQ mixture to 1100°C produced particles ~80 nm wide (Figure 4-2a). At this temperature, the GeNPs melted (bulk Ge mp ~937°C), and likely moved through the HSQ network in a liquid-like manner, acting as a nucleation point for Si atoms in the SRO. Elemental mapping of the particles using EDX shows overlapping Si and Ge atoms, suggesting the formation of an alloy (Figure 4-2b). Si–Ge alloy nanoparticles have previously been synthesized using SROs co-sputtered with Ge.[3]

While the shape yield is poor, this seeding technique could be used to grow Si–Ge alloy nanoparticles to sizes appropriate for Mie scattering at lower temperatures than those required to grow large SiNCs from pure HSQ. ETEM experiments, similar to the *in situ* experiments performed on HSQ, would capture the movement and growth of liquid GeNP seeds as they traveled through the matrix.

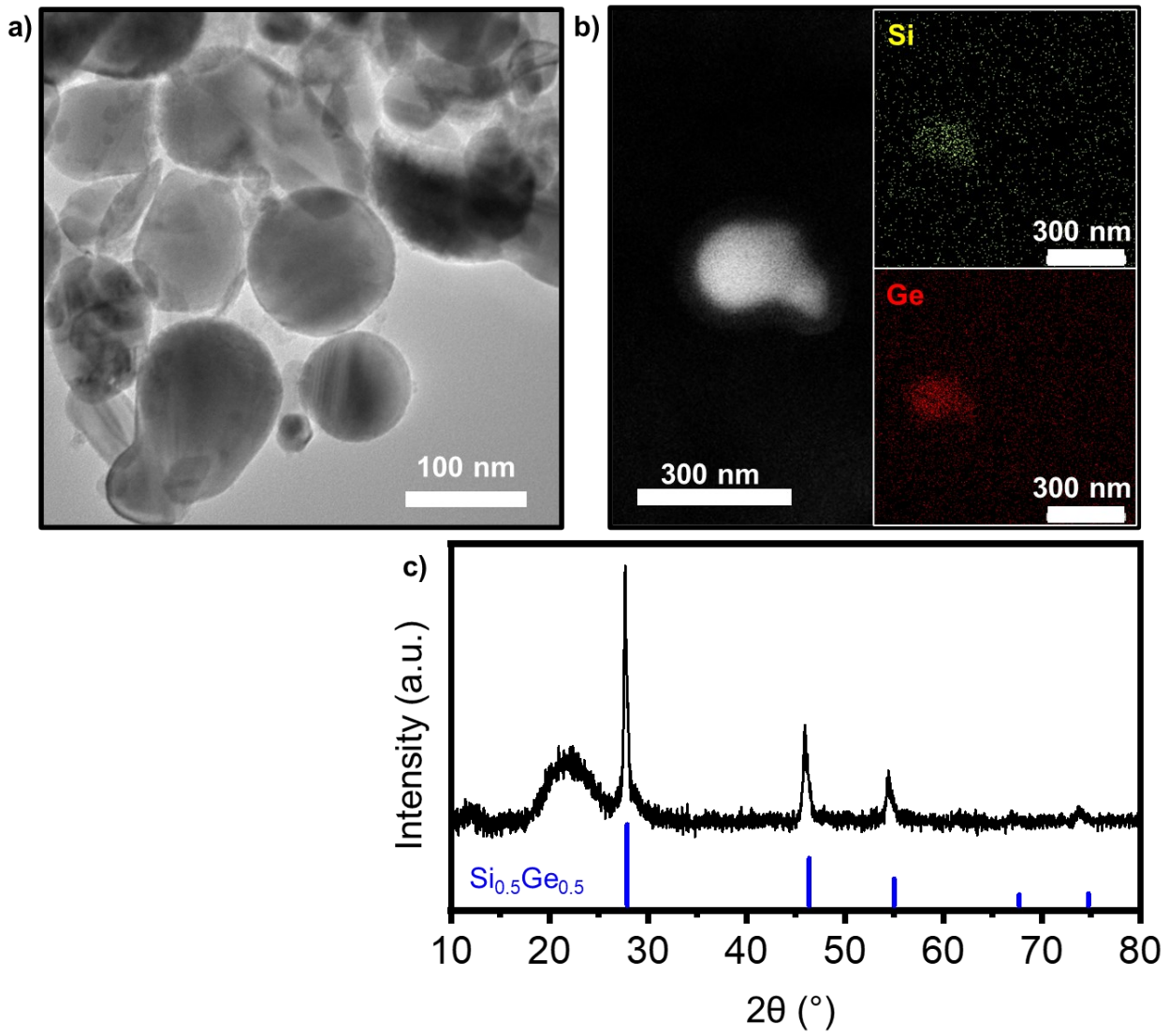

Figure 4-2. Si–Ge alloy nanoparticles grown from a mixture of HSQ and germanium nanoparticles heated to 1100°C for 1 hour. The alloy particles were liberated from the composite material with HF etching. The TEM image (a) shows polydisperse particle morphology; SEM with EDX elemental mapping (b) shows overlapping localization of Si and Ge at the particle. XRD of the composite (c) shows reflections in alignment with calculated $Ge_{0.5}Si_{0.5}$ reflections provided below the diffraction pattern.[4]

4.2.2 Applying Principles from Si-Rich Oxides to Ge-Rich Oxides

As a group 14 element, many characteristics of germanium (Ge) are similar to silicon. Like Si, elemental Ge typically forms covalent bonds in a tetrahedral geometry and crystallizes in a diamond structure. Its oxides are also alike, forming GeO_4 tetrahedra at normal atmospheric pressure.[5] The reactivity of these atoms is similar too. Germanium monoxide ($GeO_{(g)}$), for example, can become a problematic side reaction between Ge and GeO_2.[6] Given these similarities, it is likely that the insights gained from SiNC syntheses could apply to analogous germanium nanocrystal (GeNC) syntheses.

Many of the synthetic routes to germanium nanocrystals resemble those of SiNC syntheses discussed in Chapter 1. Examples include the reduction of Ge(II) and Ge(IV) compounds, or the decomposition of germane (GeH_4).[7–12] Drawing inspiration from the well-established preparation of SiNCs via thermal processing of silsesquioxanes and SROs, parallel reports from the Veinot and Ozin labs appeared in 2017 that described GeNC preparation via disproportionation of germanium hydroxide.[13, 14] The exact composition of germanium hydroxide is poorly understood, and the material remains inadequately characterized. Infrared spectroscopy of germanium hydroxide reveals Ge–O–Ge bonds and water present within the solid (Figure 4-3a), and XPS suggests that the material is a mixture Ge(IV), Ge(II), and Ge(0) sites (Figure 4-3b). The brown appearance of the solid also supports the presence of Ge-suboxides (Figure 4-3b, inset). Germanium hydroxide is often represented as $Ge(OH)_2 \cdot xH_2O$, $GeO \cdot xH_2O$, or $Ge(OH)_2$.[15]

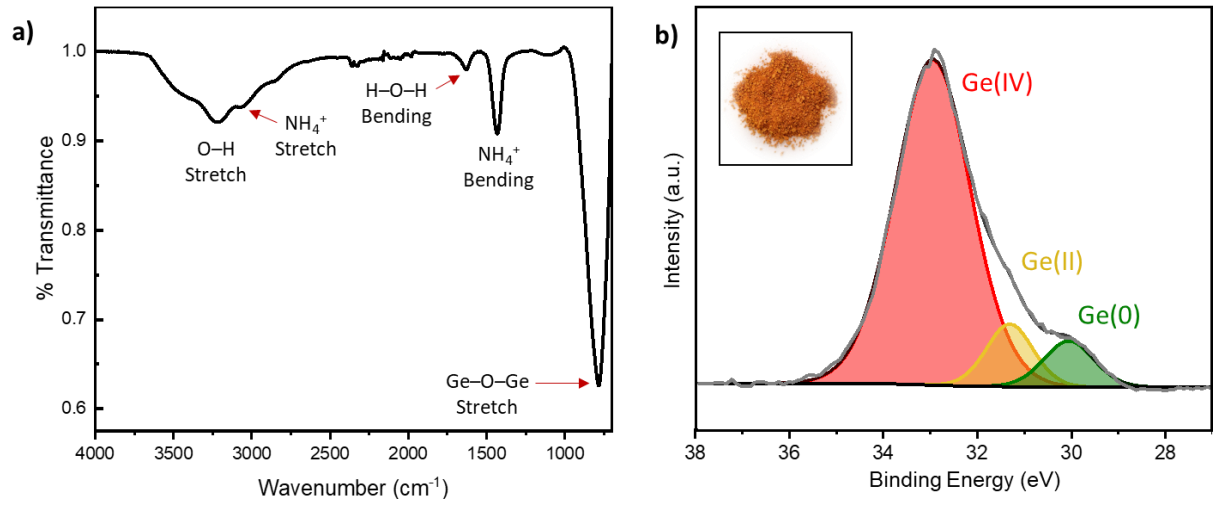

Figure 4-3. Germanium hydroxide analyzed by FTIR (a) and XPS (b). A photograph of the brown "$Ge(OH)_2$" powder is included with the XP spectrum (b, inset). Trapped ammonium cations present in the FTIR originate from the "$Ge(OH)_2$" synthesis. The spin-orbital components from the Ge3d spectrum are omitted for clarity.

Regardless of the precise stoichiometry, thermally treating "$Ge(OH)_2$" induces a disproportionation reaction affording domains of Ge(0) embedded in Ge(IV) oxide. Nanodomains of Ge begin to crystallize around 350°C and the resulting GeNC size increases with processing temperature.[13, 14] The germanium oxide matrix can also crystallize at similar temperatures but is highly dependent on the humidity of the environment during heating.[16] The oxide-embedded GeNCs can later be liberated with chemical etching.[13]

One notable parallel between $Ge(OH)_2$ and HSQ is the ability to produce nanoparticles in air. The powder X-ray diffraction pattern illustrated in Figure 4-4 compares GeNC/GeO_2 composites prepared in argon and air. The results resemble those of the SiNC/SiO_2 composites from Chapter 3; a comparison of the intensity and breadth of the diffraction peaks suggest that the size and yield of GeNCs produced in air is reduced.

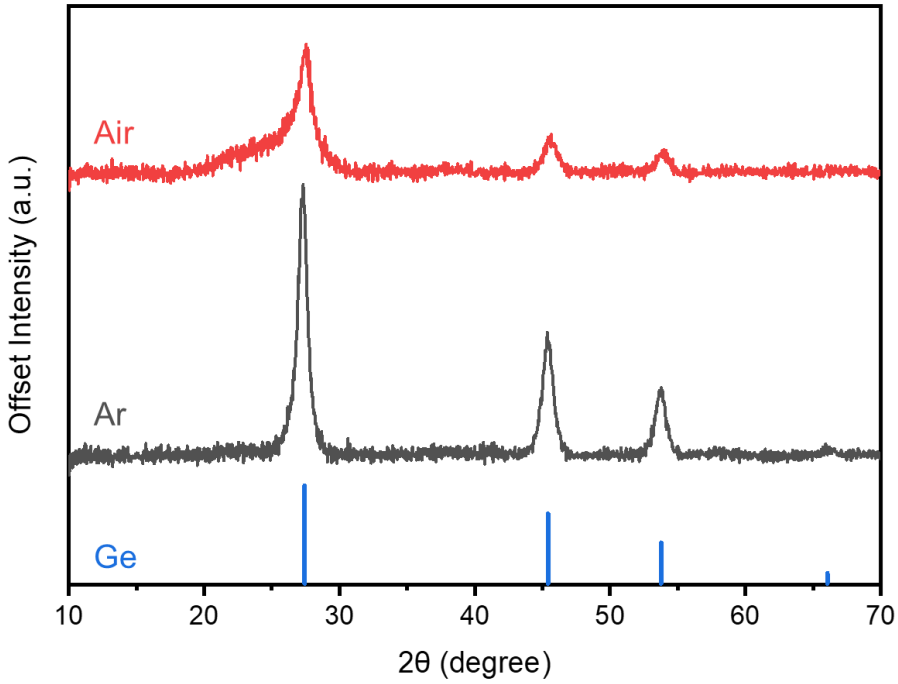

Figure 4-4. Powder XRD patterns of GeNC/GeO_2 composites heated under Ar (black) and air (red). The expected reflections from crystalline Ge are presented in blue. The "$Ge(OH)_2$" precursor was heated using an induction furnace. The heating time totaled 30 seconds and the peak processing temperature was 425°C.

These results are promising but many aspects of germanium hydroxide disproportionation to GeNCs and GeO_2 remain unclear. Firstly, a systematic comparison of GeNCs prepared in air to those prepared in Ar would illuminate the role of the processing atmosphere. This would be impactful because the current literature concerning GeNC synthesis exclusively uses inert conditions. Secondly, *in situ* heating TEM and XRD would improve our understanding of the germanium nanoparticle nucleation, growth, and crystallization mechanisms. Unlike SiNCs grown from SROs, the shape yield of GeNCs grown from germanium-rich oxides (GROs) is polydisperse and it is unclear why the nanoparticles assume non-uniform morphologies. Imaging from an electron microscope during heating and cooling of the germanium hydroxide might explain this behaviour. Lastly, a more comprehensive understanding of the local bonding environments within

germanium hydroxide may eventually solve the mysterious stoichiometry of the material. Such experiments would benefit from the newly installed low frequency NMR probe in the Michaelis research group.

4.3 References

1. Cibaka-Ndaya, C.; O'Connor, K.; Idowu, E. O.; Parker, M. A.; Lebraud, É.; Lacomme, S.; Montero, D.; Sanz Camacho, P.; Veinot, J. G. C.; Roiban, I.-L.; Drisko, G. L. Understanding the Formation Mechanisms of Silicon Particles from the Thermal Disproportionation of Hydrogen Silsesquioxane. *Chem. Mater.* **2023**, *25*, 8551–8560.
2. Khanna, V. K. Nanomaterials and Their Properties. In *Integrated Nanoelectronics*; Springer: New Delhi, 2016; pp. 25–41.
3. Joshi, K. U.; Kabiraj, D.; Narsale, A. M.; Avasthi, D. K.; Warang, T. N.; Kothari, D. C. Embedded SiGe Nanoparticles Formed by Atom Beam Co-Sputtering of Si, Ge, SiO_2. *Surf. Coat. Technol.* **2009**, *203*, 2482–2485.
4. Prilepskii V. I. Distortions of the lattices of germanium, silicon, and their solid solutions within the interval from 88 to 500 K. *Inorg. Mater*. **1965**, *1*, 1163–1167.
5. Atkins, P.; Overton, T.; Rourke, J.; Weller, M.; Armstrong, F. *Inorganic Chemistry*, 4th ed.; Salvador, P., Hagerman, M., Spiro, T., Stiefel, E., Eds.; W. H. Freeman and Company: New York, 2006.
6. Pauleau, Y.; Remy, J. C. Kinetics of the Formation and Sublimation of Germanium Monoxide. *J. Less-Common Met.* **1975**, *42*, 199–208.
7. Muthuswamy, E.; Iskandar, A. S.; Amador, M. M.; Kauzlarich, S. M. Facile Synthesis of Germanium Nanoparticles with Size Control: Microwave versus Conventional Heating. *Chem. Mater.* **2013**, *25*, 1416–1422.
8. Warner, J. H.; Tilley, R. D. Synthesis of Water-Soluble Photoluminescent Germanium Nanocrystals. *Nanotechnology* **2006**, *17*, 3745–3749.
9. Chiu, H. W.; Kauzlarich, S. M. Investigation of Reaction Conditions for Optimal Germanium Nanoparticle Production by a Simple Reduction Route. *Chem. Mater*. **2006**, *18*, 1023–1028.

10. Lu, X.; Korgel, B. A.; Johnston, K. P. High Yield of Germanium Nanocrystals Synthesized from Germanium Diiodide in Solution. *Chem. Mater*. **2005**, *17*, 6479–6485.
11. Gorla, C. R.; Liang, S.; Tompa, G. S.; Mayo, W. E.; Lu, Y. Silicon and Germanium Nanoparticle Formation in an Inductively Coupled Plasma Reactor. *J. Vac. Sci. Technol., A* **1997**, *15*, 860–864.
12. Kim, S.; Walker, B.; Park, S. Y.; Choi, H.; Ko, S.-J.; Jeong, J.; Yun, M. H.; Lee, J. C.; Kim, D. S.; Kim, J. Y. Size Tailoring of Aqueous Germanium Nanoparticle Dispersions. *Nanoscale* **2014**, *6*, 10156–10160.
13. Javadi, M.; Picard, D.; Sinelnikov, R.; Narreto, M. A.; Hegmann, F. A.; Veinot, J. G. C. Synthesis and Surface Functionalization of Hydride-Terminated Ge Nanocrystals Obtained from the Thermal Treatment of $Ge(OH)_2$. *Langmuir* **2017**, *33*, 8757–8765.
14. Sun, W.; Zhong, G.; Kübel, C.; Jelle, A. A.; Qian, C.; Wang, L.; Ebrahimi, M.; Reyes, L. M.; Helmy, A. S.; Ozin, G. A. Size-Tunable Photothermal Germanium Nanocrystals. *Angew. Chem. Int. Ed.* **2017**, *56*, 6329–6334.
15. Yang, D. J.; Jolly, W. L.; O'Keefe, A. Conversion of Hydrous Germanium(II) Oxide to Germynyl Sesquioxide, $(HGe)_2O_3$. *Inorg. Chem.* **1977**, *16*, 2980–2982.
16. Wang, Y.; Ramesh, U.; Charles; Ryan, B. J.; Nelson, R. D.; Alebri, A. M.; Hamdeh, U. H.; Hadi, A.; Smith, E. A.; Panthani, M. G. Synthesis of Germanium Nanocrystals from Solid-State Disproportionation of a Chloride-Derived Germania Glass. *Chem. Commun.* **2019**, *55*, 6102–6105.

Bibliography

Chapter 1

1. Feldman, L. C. Introduction. In *Fundamental Aspects of Silicon Oxidation*; Chabal, Y. J., Ed.; Springer Series in Materials Science; Springer: Berlin, 2001; Vol. 46, pp 1–11.
2. Ameta S. C. Nanomaterials: An Introduction. In *The Science of Nanomaterials: Basics and Applications*; Ameta S. C.; Ameta, R., Ed.; Apple Academic Press: New York, 2022; pp 1–18.
3. Lehmann, V.; Gösele, U. Porous silicon: Quantum sponge structures grown via a self-adjusting etching process. *Adv. Mater*. **1992**, *4*, 114–116.
4. Canham, L. T. Silicon quantum wire array fabrication by electrochemical and chemical dissolution of wafers. *Appl. Phys. Lett*. **1990**, *57*, 1046–1048.
5. Sailor, M.J. Preparation of Micro-, Meso-, and Macro-Porous Silicon Layers. In *Porous Silicon in Practice: Preparation, Characterization and Applications*, Sailor, M. J., Ed.; Wiley: 2011; pp 43-76.
6. Faure, G. *Principles and Applications of Inorganic Geochemistry : A Comprehensive Textbook for Geology Students*. Macmillan Pub. Co.: New York, 1991.
7. Reiss, P.; Carrière, M.; Lincheneau, C.; Vaure, L.; Tamang, S. Synthesis of Semiconductor Nanocrystals, Focusing on Nontoxic and Earth-Abundant Materials. *Chem. Rev.* **2016**, *116*, 10731−10819.
8. Warner, J. H.; Hoshino, A.; Yamamoto, K.; Tilley, R. D. Water-Soluble Photoluminescent Silicon Quantum Dots. *Angew. Chem. Int. Ed*. **2005**, *44*, 4550−4554.
9. Park, J. H.; Gu, L.; Maltzahn, G.; Ruoslahti, E.; Bhatia, S. N.; Sailor, M. J. Biodegradable luminescent porous silicon nanoparticles for in vivo applications. *Nat. Mater*. **2009**, *8*, 331–336.
10. Cheong, I. T.; Mock, J.; Kallergi, M.; Groß, E.; Meldrum, A.; Rieger, B.; Becherer, M.; Veinot, J. G. C. Colloidal Silicon Quantum Dot-Based Cavity Light-Emitting Diodes with Narrowed and Tunable Electroluminescence. *Adv. Opt. Mater.* **2023**, *11*, 2201834.
11. Erogbogbo, F.; Yong, K. T.; Roy, I.; Hu, R.; Law, W. C.; Zhao, W.; Ding, H.; Wu, F.; Kumar, R.; Swihart, M. T.; Prasad, P. N. In Vivo Targeted Cancer Imaging, Sentinel Lymph Node

Mapping and Multi-Channel Imaging with Biocompatible Silicon Nanocrystals. *ACS Nano* **2011**, *5*, 413–423.

12. Cheong, I. T.; Morrish, W.; Sheard, W.; Yu, H.; Luppi, B. T.; Milburn, L.; Meldrum, A.; Veinot, J. G. C. Silicon Quantum Dot–Polymer Fabry–Pérot Resonators with Narrowed and Tunable Emissions. *ACS Appl. Mater. Interfaces* **2021**, *13*, 27149−27158.
13. Meinardi, F.; Ehrenberg, S.; Dhamo, L.; Carulli, F.; Mauri, M.; Bruni, F.; Simonutti, R.; Kortshagen, U.; Brovelli, S. Highly Efficient Luminescent Solar Concentrators Based on Earth-Abundant Indirect-Bandgap Silicon Quantum Dots. *Nat. Photonics* **2017**, *11*, 177–185.
14. Milburn, L.; Robidillo, C.J.; Dalangin, R.; Shen, Y.; Veinot, J. G. C. A Complementary Silicon Quantum Dot-Enzyme Platform for the Selective Detection of Nitroaromatic Compounds: Explosives versus Nerve Agents. *ACS Appl. Nano Mater.* **2022**, *5*, 11984−11990.
15. Canham, L. Introductory Lecture: Origins and Applications of Efficient Visible Photoluminescence from Silicon-Based Nanostructures. *Faraday Discuss.* **2020**, *222*, 10−81.
16. Sato, K.; Tsuji, H.; Hirakuri, K.; Fukata, N.; Yamauchi, Y. Controlled Chemical Etching for Silicon Nanocrystals with Wavelength-Tunable Photoluminescence. *Chem. Commun.* **2009**, 3759−3761.
17. Shirahata, N.; Nakamura, J.; Inoue, J. I.; Ghosh, B.; Nemoto, K.; Nemoto, Y.; Takeguchi, M.; Masuda, Y.; Tanaka, M.; Ozin, G. A. Emerging Atomic Energy Levels in Zero-Dimensional Silicon Quantum Dots. *Nano Lett.* **2020**, *20*, 1491–1498.
18. Beard, M. C.; Knutsen, K. P.; Yu, P.; Luther, J. M.; Song, Q.; Metzger, W. K.; Ellingson, R. J.; Nozik, A. J. Multiple Exciton Generation in Colloidal Silicon Nanocrystals. *Nano Lett.* **2007**, *7*, 2506–2512.
19. Lin, S. W.; Chen, D. H. Synthesis of Water-Soluble Blue Photoluminescent Silicon Nanocrystals with Oxide Surface Passivation. *Small* **2009**, *5*, 72–76.
20. Brus, L. E.; Szajowski, P. F.; Wilson, W. L.; Harris, T. D.; Schuppler, S.; Citrin, P. H. Electronic Spectroscopy and Photophysics of Si Nanocrystals: Relationship to Bulk c-Si and Porous Si. *J. Am. Chem. Soc.* **1995**, *117*, 2915–2922.

21. Yu, Y.; Fan, G.; Fermi, A.; Mazzaro, R.; Morandi, V.; Ceroni, P.; Smilgies, D. M.; Korgel, B. A. Size-Dependent Photoluminescence Efficiency of Silicon Nanocrystal Quantum Dots. *J. Phys. Chem. C* **2017**, *121*, 23240–23248.
22. Anthony, R.; Kortshagen, U. Photoluminescence Quantum Yields of Amorphous and Crystalline Silicon Nanoparticles. *Phys. Rev. B* **2009***, 80*, 115407.
23. Thiessen, A. N.; Ha, M.; Hooper, R. W.; Yu, H.; Oliynyk, A. O.; Veinot, J. G. C.; Michaelis. Silicon Nanoparticles: Are They Crystalline from the Core to the Surface? *Chem. Mater*. **2019**, *31*, 678−688.
24. Thiessen, A. N.; Zhang, L.; Oliynyk, A. O.; Yu, H.; O'Connor, K. M.; Meldrum, A.; Veinot, J. G. C. A Tale of Seemingly "Identical" Silicon Quantum Dot Families: Structural Insight into Silicon Quantum Dot Photoluminescence. *Chem. Mater.* **2020***, 32,* 6838−6846.
25. Milliken, S.; Thiessen, A. N.; Cheong, I. T.; O'Connor, K. M.; Li, Z.; Hooper, R. W.; Robidillo, C. J. T.; Veinot, J. G. C. "Turning the dials": Controlling Synthesis, Structure, Composition, and Surface Chemistry to Tailor Silicon Nanoparticle Properties. *Nanoscale,* **2021***, 13,* 16379–16404.
26. Dasog, M.; De, l. R.; Titova, L. V.; Hegmann, F. A.; Veinot, J. G. C. Size vs Surface: Tuning the Photoluminescence of Freestanding Silicon Nanocrystals Across the Visible Spectrum via Surface Groups. *ACS Nano* **2014***, 8*, 9636–9648.
27. Sinelnikov, R.; Dasog, M.; Beamish, J.; Meldrum, A.; Veinot, J. G. C. Revisiting an Ongoing Debate: What Role Do Surface Groups Play in Silicon Nanocrystal Photoluminescence? *ACS Photonics* **2017**, *4*, 1920–1929.
28. Manthiram, A. Material Aspects: An Overview. In *Lithium Batteries*; Nazri, G. A.; Pistoia, G., Ed.; Science and Technology; Springer: New York, 2003; pp 3–41.
29. Julien, C.; Mauger, A.; Vijh, A.; Zaghib, K. *Lithium Batteries*; Science and Technology; Springer: New York, 2015.
30. Entwistle, J.; Rennie, A.; Patwardhan, S. A Review of Magnesiothermic Reduction of Silica to Porous Silicon for Lithium-Ion Battery Applications and Beyond. *J. Mater. Chem. A* **2018**, *6*, 18344–18356.
31. Zamfir, M. R.; Nguyen, H. T.; Moyen, E.; Leeac, Y. H.; Pribat, D. Silicon Nanowires for Li-Based Battery Anodes: A Review. *J. Mater. Chem. A* **2013**, *1*, 9566–9586.

32. Aghajamali, M.; Xie, H.; Javadi, M.; Kalisvaart, W. P.; Buriak, J. M.; Veinot, J. G. C. Size and Surface Effects of Silicon Nanocrystals in Graphene Aerogel Composite Anodes for Lithium Ion Batteries. *Chem. Mater.* **2018**, *30*, 7782–7792.
33. Zhu, G.; Luo, W.; Wang, L.; Jiang, W.; Yang, J. Silicon: Toward Eco-friendly Reduction Techniques for Lithium-ion Battery Applications. *J. Mater. Chem. A* **2019**, *7*, 24715–24737.
34. Magasinski, A.; Dixon, P.; Hertzberg, B.; Kvit, A.; Ayala, J.; Yushin, G. High-Performance Lithium-ion Anodes Using a Hierarchical Bottom-up Approach. *Nat. Mater.* **2010**, *9*, 353–358.
35. Pendry, J. B.; Schurig, D.; Smith, D. R. Controlling Electromagnetic Fields. *Science* **2006**, *312*, 1780–1782.
36. Jahani, S.; Jacob, Z. All-Dielectric Metamaterials. *Nat. Nanotechnol.* **2016**, *11*, 23–36.
37. Zhang, C.; Xu, Y.; Liu, J.; Li, J.-T.; Xiang, J.; Li, H.; Li, J.-X.; Dai, Q.-F.; Lan, S.; Miroshnichenko, A. E. Lighting up Silicon Nanoparticles with Mie Resonances. *Nat. Commun.* **2018**, *9*, 2964.
38. Kuznetsov, A. I.; Miroshnichenko, A. E.; Brongersma, M. L.; Kivshar, Y. S.; Luk'yanchuk, B. Optically Resonant Dielectric Nanostructures. *Science* **2016**, *354*, aag2472.
39. De Marco, M. L.; Semlali, S.; Korgel, B. A.; Barois, P.; Drisko, G. L.; Aymonier, C. Silicon-Based Dielectric Metamaterials: Focus on the Current Synthetic Challenges. *Angew. Chem. Int. Ed.* **2018**, *57*, 4478–4498.
40. De Marco, M. L. Supercritical Synthesis of High Refractive Index Silicon Particles for Optical Metamaterials. Ph.D. Dissertation, Université de Bordeaux, 2019.
41. Hidemasa Negoro; Sugimoto, H.; Fujii, M. Helicity-Preserving Optical Metafluids. *Nano Lett.* **2023**, *23*, 5101–5107.
42. Wang, L.; Reipa, V.; Blasic, J. Silicon Nanoparticles as a Luminescent Label to DNA. *Bioconjugate Chem*. **2004**, *15*, 409−412.
43. Choi, J.; Wang, N. S.; Reipa, V. Photoassisted Tuning of Silicon Nanocrystal Photoluminescence. *Langmuir* **2007**, *23*, 3388−3394.
44. Jung, K. H.; Shih, S.; Hsieh, T. Y.; Kwong, D. L.; Lin, T. L. Intense Photoluminescence from Laterally Anodized Porous Si. *Appl. Phys. Lett.* **1991**, *59*, 3264–3266.

45. Hwang, J.; Jeong, Y.;Lee, K. H.; Seo, Y.; Kim, J.; Hong, J. W.; Kamaloo, E.; Camesano, T. A.; Choi, J. Simple Preparation of Fluorescent Silicon Nanoparticles from Used Si Wafers. *Ind. Eng. Chem. Res.* **2015**, *54*, 5982–5989.
46. Zhu, J.; Wu, Yd.; Li, Th.; Chen, H.; Fan, L.; Xiao, C. Silicon Nanocrystallites Produced Via a Chemical Etching Method and Photoluminescence Properties. *J. Mater. Sci.* **2014**, *49*, 4349–4353.
47. Zhang, D.; Gökce, B.; Barcikowski, S. Laser Synthesis and Processing of Colloids: Fundamentals and Applications. *Chem. Rev.* **2017**, *117*, 3990−4103.
48. Ishikawa, Y.; Tsuji, T.; Sakaki, S.; Koshizaki, N. Pulsed laser melting in liquid for crystalline spherical submicrometer particle fabrication– Mechanism, process control, and applications. *Prog. Mater Sci*. **2023**, *131*, 101004.
49. Shirahata, N.; Hirakawaa, D.; Sakka, Y. Interfacial-related Color Tuning of Colloidal Si Nanocrystals. *Green Chem.* **2010**, *12*, 2139–2141.
50. Yuan, Z.; Nakamura, T.; Adachi, S.; Matsuishi, K. Improvement of Laser Processing for Colloidal Silicon Nanocrystal Formation in a Reactive Solvent. *J. Phys. Chem. C* **2017**, *121*, 8623–8629.
51. Kim, M.; Osone, S.; Kim, T.; Higashi, H.; Seto, T. Synthesis of Nanoparticles by Laser Ablation: A Review. *Kona Powder Part. J.* **2017**, *34*, 80–90.
52. Švrček, V.; Rehspringer, J. -L.; Gaffet, E.; Slaoui, A.; Muller, J. -C. Unaggregated Silicon Nanocrystals Obtained by Ball Milling. *J. Cryst. Growth* **2005**, *275*, 589–597.
53. Lam, C.; Zhang, Y. F.; Tang, Y. H.; Lee, C. S.; Bello, I.; Lee, S. T. Large-scale Synthesis of Ultrafine Si Nanoparticles. *J. Cryst. Growth* **2000**, *220*, 466–470.
54. Chaudhary, A. -L.; Sheppard, D. A.; Paskevicius, M.; Saundersc, M.; Buckley, C. E. Mechanochemical Synthesis of Amorphous Silicon Nanoparticles by Ball Milling. *RSC Adv*. **2014**, *4*, 21979–21983.
55. Kuang, L.; Mitchell, B. S.; Fink, M. J. Silicon nanoparticles synthesised through reactive high-energy ball milling: enhancement of optical properties from the removal of iron impurities. *J. Exp. Nanosci.* **2015**, *10*, 1214–1222.
56. Chaâbani, W.; Proust, J.; Movsesyan, A.; Béal, J.; Baudrion, A. -L.; Adam, P. -M.; Chehaidar, A.; Plain, J. Large-Scale and Low-Cost Fabrication of Silicon Mie Resonators. *ACS Nano* **2019**, *13*, 4199−4208.

57. Tilley, R. D.; Warner, J. H.; Yamamoto, K.; Matsuib, I.; Fujimoric, H. Micro-emulsion Synthesis of Monodisperse Surface Stabilized Silicon Nanocrystals. *Chem. Commun*. **2005**, 1833−1835.

58. Shiohara, A.; Prabakar, S.; Faramus, A.; Hsu, C. -Y.; Lai, P. -S.; Northcotea, P. T.; Tilley, R. D. Sized controlled synthesis, purification, and cell studies with silicon quantum dots. *Nanoscale* **2011**, *3*, 3364–3370.

59. Baldwin, R. K.; Pettigrew, K. A.; Ratai, E.; Augustine, M. P.; Kauzlarich, S. M. Solution reduction synthesis of surface stabilized silicon nanoparticles. *Chem. Commun*. **2002**, 1822–1823.

60. Zou, J.; Sanelle, P.; Pettigrew, K. A.; Kauzlarich, S. M. Size and Spectroscopy of Silicon Nanoparticles Prepared via Reduction of $SiCl_4$. *J. Cluster Sci*. **2006**, *17*, 565–578.

61. Yang, C. -S.; Bley, R. A.; Kauzlarich, S. M.; H. Lee, H. W. H.; Delgado, G. R. Synthesis of Alkyl-Terminated Silicon Nanoclusters by a Solution Route. *J. Am. Chem. Soc*. **1999**, *121*, 5191–5195.

62. Dasog, M.; Yang, Z.; Regli, S.; Atkins, T. M.; Faramus, A.; Singh, M. P.; Muthuswamy, E.; Kauzlarich, S. M.; Tilley, R. D.; Veinot, J. G. C. Chemical Insight into the Origin of Red and Blue Photoluminescence Arising from Freestanding Silicon Nanocrystals. *ACS Nano* **2013***, 7*, 2676–2685.

63. Semlali, S.; Cormary, B.; De Marco, M. L.; Majimel, J.; Saquet, A.; Coppel, Y.; Gonidec, M.; Rosa, P.; Drisko, G. L. Effect of Solvent on Silicon Nanoparticle Formation and Size: A Mechanistic Study. *Nanoscale* **2019**, *11*, 4696–4700

64. Dasog, M.; Yang, Z.; Veinot, J. G. C. Size-controlled solid state synthesis of luminescent silicon nanocrystals using Stober silica particles. *CrystEngComm*. **2012**, *14*, 7576–7578.

65. Murthy, T. U. M. S.; Miyamoto, N.; Shimbo, M.; Nishizawa, J. Gas-phase nucleation during the thermal decomposition of silane in hydrogen. *J. Cryst. Growth* **1976**, *33*, 1–7.

66. Kakati, M.; Das, A. K. Chapter 1 – Thermal Plasma Assisted Techniques for Synthesis of High Temperature Meteraial Nanoparticles. In *New Nanotechniques*; Malik, A.; Rawat, R. J., Ed.; Nova Science Publishers: New York, 2009; pp 1–20.

67. Slootman, F.; Parent, J. -C. Homogeneous gas-phase nucleation in silane pyrolysis. *J. Aerosol Sci*. **1994**, 25, 15–21.

68. Littau, K. A.; Szajowski, P. J.; Muller, A. J.; Kortan, A. R.; Bins, L. E. A Luminescent Silicon Nanocrystal Colloid via a High-Temperature Aerosol Reaction. *J. Phys. Chem*. **1993**, *97*, 1224–1230.

69. Onischuk, A. A.; Strunin, V. P.; Ushakova, M. A.; Panfilov, V. N. On the pathways of aerosol formation by thermal decomposition of silane. *J. Aerosol Sci*. **1997**, *28*, 207–222.

70. Zhang, P.; Duan, J.; Chen, G.; Li, J.; Wang, W. Production of polycrystalline silicon from silane pyrolysis: A review of fines formation. *Sol. Energy* **2018**, *175*, 44–53.

71. Girshick, S. L.; Swihart, M. T.; Suh, S.-M.; Mahajan, M. R.; Nijhawan, S. Numerical Modeling of Gas-Phase Nucleation and Particle Growth during Chemical Vapor Deposition of Silicon. *J. Electrochem. Soc.* **2000**, *147*, 2303–2311.

72. Vazquez-Pufleau, M.; Wang, Y.; Biswas, P.; Thimsen, E. Measurement of sub-2 nm stable clusters during silane pyrolysis in a furnace aerosol reactor. *J. Chem. Phys*. **2020**, *152*, 024304.

73. Li, X.; He, Y.; Talukdar, S. S.; Swihart, M. T. Process for Preparing Macroscopic Quantities of Brightly Photoluminescent Silicon Nanoparticles with Emission Spanning the Visible Spectrum. *Langmuir* **2003**, *19*, 8490–8496.

74. Li, X.; He, Y.; Swihart, M. T. Surface Functionalization of Silicon Nanoparticles Produced by Laser-Driven Pyrolysis of Silane followed by HF–HNO_3 Etching. *Langmuir* **2004**, *20*, 4720–4727.

75. Hua, F.; Swihart, M. T.; Ruckenstein, E. Efficient Surface Grafting of Luminescent Silicon Quantum Dots by Photoinitiated Hydrosilylation. *Langmuir* **2005**, *21*, 6054–6062.

76. Pell, L. E.; Schricker, A. D.; Mikulec, F. V.; Korgel, B. A. Synthesis of Amorphous Silicon Colloids by Trisilane Thermolysis in High Temperature Supercritical Solvents. *Langmuir* **2004**, *20*, 6546–6548.

77. Harris, J. T.; Hueso, J. L.; Korgel, B. A. Hydrogenated Amorphous Silicon (a-Si:H) Colloids. *Chem. Mater*. **2010**, *22*, 6378–6383.

78. Shi, L.; Harris, J.; Fenollosa, R.; Rodriguez, I.; Lu, X.; Korgel, B. A.; Meseguer, F. Monodisperse silicon nanocavities and photonic crystals with magnetic response in the optical region. *Nat. Commun*. **2013**, *4*, 1904.

79. De Marco, M. L.; Jiang, T.; Fang, J.; Lacomme, S.; Zheng, Y.; Baron, A.; Korgel, B. A.; Barois, P.; Drisko, G. L.; Aymonier, C. Broadband Forward Light Scattering by

Architectural Design of Core–Shell Silicon Particles. *Adv. Funct. Mater*. **2021**, *31*, 2100915.

80. Holmes, J. D.; Ziegler, K. J.; Doty, R. C.; Pell, L. E.; Johnston, K. P.; Korgel, B. A. Highly Luminescent Silicon Nanocrystals with Discrete Optical Transitions. *J. Am. Chem. Soc*. **2001**, *123*, 3743–3748.
81. Heath, J. R. A Liquid-Solution-Phase Synthesis of Crystalline Silicon. *Science* **1992**, *258*, 1131–1133.
82. Kortshagen, U. R.; Sankaran, R. M.; Pereira, R. N.; Girshick, S. L.; Wu, J. J.; Aydil, E. S. Nonthermal Plasma Synthesis of Nanocrystals: Fundamental Principles, Materials, and Applications. *Chem. Rev.* **2016**, *116*, 11061–11127.
83. Bhandarkar, U. V.; Swihart, M. T.; Girshick, S. L.; Kortshagen, U. R. Modelling of silicon hydride clustering in a low-pressure silane plasma. *J. Phys. D: Appl. Phys.* **2000**, *33*, 2731–2746.
84. Loh, K. Q. Andaraarachchi, H. P.; Ferry, V. E.; Kortshagen, U. R. Photoluminescent Si/SiO_2 Core/Shell Quantum Dots Prepared by High-Pressure Water Vapor Annealing for Solar Concentrators, Light-Emitting Devices, and Bioimaging. *ACS Appl. Nano Mater.* **2023**, *6*, 6444−6453.
85. Li, Z.; Kortshagen, U. R. Aerosol-Phase Synthesis and Processing of Luminescent Silicon Nanocrystals. *Chem. Mater.* **2019**, *31*, 8451−8458.
86. Eslamisaray, M. A.; Wray, P. R.; Lee, Y.; Nelson, G. M.; Ilic, O.; Atwater, H. A.; Kortshagen, U. R. A Single-Step Bottom-up Approach for Synthesis of Highly Uniform Mie-Resonant Crystalline Semiconductor Particles at Visible Wavelengths. *Nano Lett.* **2023**, *23*, 1930−1937.
87. Guruvenket, S.; Hoey, J. M.; Anderson, K. J.; Frohlich, M. T.; Krishnan, R.; Sivaguru, J.; Sibi, M. P.; Boudjouk, P. Synthesis of Silicon Quantum Dots Using Cyclohexasilane (Si_6H_{12}). *J. Mater. Chem. C* **2016**, *4*, 8206–8213.
88. Yasar-Inceoglu, O.; Lopez, T.; Farshihagro, E.; Mangolini, L. Silicon Nanocrystal Production through Non-Thermal Plasma Synthesis: A Comparative Study between Silicon Tetrachloride and Silane Precursors, *Nanotechnology* **2012**, 23, 255604.
89. Kelly, J. A.; Henderson, E. J.; Veinot, J. G. C. Sol–gel precursors for group 14 nanocrystals. *Chem. Commun*. **2010**, *46*, 8704–8718.

90. Meldrum, A. Hryciw, A.; MacDonald, A. N.; Blois, C.; Marsh, K.; Wang, J.; Li, Q. Photoluminescence in the silicon-oxygen system. *J. Vac. Sci. Technol., A* **2006**, *24*, 713–717.

91. Ma, Z.; Liao, X.; He, J.; Cheng, W.; Yue, G.; Wang, Y.; Kong, G. Annealing behaviors of photoluminescence from SiO_x : H. *J. Appl. Phys.* **1998**, *83*, 7934–7939.

92. Sorarù, G. D.; Modena, S.; Bettotti, P.; Das, G.; Mariotto, G.; Pavesi, L. Si Nanocrystals Obtained Through Polymer Pyrolysis. *Appl. Phys. Lett.* **2003**, *83*, 749–751.

93. Hessel, C. M.; Henderson, E. J.; Veinot, J. G. C. Hydrogen Silsesquioxane: A Molecular Precursor for Nanocrystalline Si-SiO2 Composites and Freestanding Hydride Surface Terminated Silicon Nanoparticles. *Chem. Mat.* **2006**, 18, 6139–6146.

94. Shimizu-Iwayama, T.; Ohshima, M.; Niimi, T.; Nakao, S.; Kazuo, S.; Fujita, T.; Itoh, N. Visible Photoluminescence Related to Si Precipitates in Si^+-Implanted SiO_2. *J. Phys.: Condens. Matter* **1993**, *5*, L375–L380.

95. Withrow, S. P.; White, C. W.; Meldrum, A.; Budai, J. D.; Hembree, D. M.; Barbour, J. C. Effects of Hydrogen in the Annealing Environment on Photoluminescence from Si Nanoparticles in SiO_2. *J. Appl. Phys.* **1999**, *86*, 396–401.

96. Meldrum, A.; Haglund, R. F. Jr.; Boatner, L. A.; White, C. W. Nanocomposite Materials Formed by Ion Implantation. *Adv. Mater.* **2001**, *13*, 1431–1444.

97. Zhang, M.; Poumirol, J. -M.; Chery, N.; Majorel, C.; Demoulin, R.; Talbot, E.; Rinnert, H.; Girard, C.; Cristiano, F.; Wiecha, P. R.; Hungria, T.; Paillard, V.; Arbouet, A.; Pécassou, B.; Gourbilleau, F.; Bonafos, C. Infrared Nanoplasmonic Properties of Hyperdoped Embedded Si Nanocrystals in the Few Electrons Regime. *Nanophotonics* **2022**, *11*, 3485–3493.

98. Rimini, E. *Ion Implantation: Basics to Device Fabrication*; The Springer International Series in Engineering and Computer Science; Springer US: Boston, 1995.

99. Behrisch, R., Eckstein, W. *Sputtering by Particle Bombardment: Experiments and Computer Calculations from Theshold to MeV Energies*; Behrisch, R., Eckstein, W., Eds.; Topics in Applied Physics 110; Springer: Berlin, 2007.

100. Hayashi, S.; T. Nagareda; Yuchi Kanzawa; Yamamoto, K. Photoluminescence of Si-Rich SiO_2 Films: Si Clusters as Luminescent Centers. *Jpn. J. Appl. Phys.* **1993**, *32*, 3840–3840.

101. Bera, S.; Chaudhuri, S.; Bandyopadhyay, A. K.; Chakraborty, B.; Pal, A. K. Quantum Size Effect in Silicon Nanocrystals Prepared by Dc Magnetron Sputtering. *J. Phys. D: Appl. Phys.* **2001**, *34*, 273–278.

102. Iwamori, S.; Gotoh, Y.; Moorthi, K. Silicon Oxide Gas Barrier Films Deposited by Reactive Sputtering. *Surf. Coat. Technol.* **2003**, *166*, 24–30.

103. Mamiya, M.; Takei, H.; Kikuchi, M.; Uyeda, C. Preparation of Fine Silicon Particles from Amorphous Silicon Monoxide by the Disproportionation Reaction. *J. Cryst. Growth* **2001**, *229*, 457–461.

104. Sun, W.; Qian, C.; Cui, X. S.; Wang, L.; Wei, M.; Casillas, G.; Helmy, A. S.; Ozin, G. A. Silicon Monoxide – a Convenient Precursor for Large Scale Synthesis of near Infrared Emitting Monodisperse Silicon Nanocrystals. *Nanoscale* **2016**, *8*, 3678–3684.

105. Sugimoto, H.; Okazaki, T.; Fujii, M. Mie Resonator Color Inks of Monodispersed and Perfectly Spherical Crystalline Silicon Nanoparticles. *Adv. Opt. Mater.* **2020**, *8*, 2000033–2000033.

106. Kasai, H.; Sugimoto, H.; Fujii, M. Selective Enhancement of Crystal-Field-Split Narrow *F-F* Emission Lines of Europium Ions by Electric and Magnetic Purcell Effect of Mie Resonant Silicon Nanosphere. *Adv. Opt. Mater.* **2023**, 2301204.

107. Benyon, J. Silicon Monoxide: Fact or Fiction. *Vacuum* **1970**, *20*, 293–294.

108. J. Yasaitis; Kaplow, R. Structure of Amorphous Silicon Monoxide. *J. Appl. Phys.* **1972**, *43*, 995–1000.

109. Hohl, A.; Wieder, T.; van Aken, P. A.; Weirich, T. E.; Denninger, G.; Vidal, M.; Oswald, S.; Deneke, C.; Mayer, J.; Fuess, H. An Interface Clusters Mixture Model for the Structure of Amorphous Silicon Monoxide (SiO). *Non-Cryst. Solids* **2003**, *320*, 255–280.

110. Schulmeister, K.; Mader, W. TEM Investigation on the Structure of Amorphous Silicon Monoxide. *Non-Cryst. Solids* **2003**, *320*, 143–150.

111. Hirata, A.; Kohara, S.; Asada, T.; Arao, M.; Yogi, C.; Imai, H.; Tan, Y.; Fujita, T.; Chen, M. Atomic-Scale Disproportionation in Amorphous Silicon Monoxide. *Nat. Commun.* **2016**, *7*, 11591.

112. Tangstad, M. Chapter 6 - Ferrosilicon and Silicon Technology. In *Handbook of Ferroalloys: Theory and Technology*; Gasik, M., Ed.; Butterworth-Heinemann, 2013; pp 179–220.

113. Snyder, L. E.; Buhl, D. Detection of Possible Maser Emission near 3.48 Millimeters from an Unidentified Molecular Species in Orion. *Astrophys. J.* **1974**, *189*, L31–L33.

114. Yoon, D.-H.; Cho, S.-H.; Yun, Y.; Choi, Y. K.; Dodson, R.; Rioja, M.; Kim, J.; Imai, H.; Kim, D.; Yang, H.; Byun, D.-Y. Astrometrically Registered Maps of H_2O and SiO Masers toward VX Sagittarii. *Nat. Commun.* **2018**, *9*, 2534.

115. Kenyon, A. J.; P.F. Trwoga; Pitt, C.; Rehm, G. The Origin of Photoluminescence from Thin Films of Silicon-Rich Silica. *J. Appl. Phys.* **1996**, *79*, 9291–9300.

116. Ma, Z.; Liao, X.; He, J.; Cheng, W.; Yue, G.; Wang, Y.; Kong, G. Annealing Behaviors of Photoluminescence from SiOx:H. *J. Appl. Phys.* **1998**, *83*, 7934–7939.

117. Zacharias, M.; Heitmann, J.; Scholz, R.; Kahler, U.; Schmidt, M.; Bläsing, J. Size-Controlled Highly Luminescent Silicon Nanocrystals: A SiO/SiO2 Superlattice Approach. *Appl. Phys. Lett.* **2002**, *80*, 661–663.

118. Kickelbick, G. Silsesquioxanes. In *Functional Molecular Silicon Compounds I: Regular Oxidation States*. Scheschkewitz, D., Ed.; Structure and Bonding; Springer, 2014; Vol. 155, pp 1–28.

119. Frye, C. L.; Collins, W. T. The Oligomeric Silsesquioxanes, $(HSiO_{3/2})_n$. *J. Am. Chem. Soc.*, **1970**, *92*, 5586–5588.

120. Namatsu, H.; Yamaguchi, T.; Nagase, M.; Yamazaki, K.; Kurihara, K. Nano-Patterning of a Hydrogen Silsesquioxane Resist with Reduced Linewidth Fluctuations. *Microelectron. Eng.* **1998**, *41*, 331–334.

121. Grigorescu, A. E.; van der Krogt, M. C.; Hagen, C. W.; Kruit, P. 10 nm lines and spaces written in HSQ, using electron beam lithography. *Microelectron. Eng.* **2007**, *84*, 822– 824.

122. Baek, I.-B.; Yang, J.-H.; Cho, W.-J.; Ahn, C.-G.; Im, K.; Lee, S. Electron beam lithography patterning of sub-10nm line using hydrogen silsesquioxane for nanoscale device applications. *J. Vac. Sci. Technol., B* **2005**, *23*, 3120–3123.

123. Chen, H.; Tecklenburg, R. E. Characterization of Low and Intermediate Molecular Weight Hydrogen Silsesquioxanes by Mass Spectrometry. *J. Am. Soc. Mass Spectrom*. **2006**, *17*, 1438–1441.

124. Pauthe, M.; Bernstein, E.; Dumas, J,; Saviot, L.; Pradel, A.; Ribes, M. Preparation and characterisation of Si nanocrystallites embedded in a silica matrix. *J. Mater. Chem*. **1999**, *9*, 187–191.

125. Hessel, C. M.; Henderson, E. J.; Veinot, J. G. C. An Investigation of the Formation and Growth of Oxide Embedded Silicon Nanocrystals in Hydrogen Silsesquioxane Derived Nanocomposites. *J. Phys. Chem. C* **2007**, *111*, 6956–6961.

126. Yang, C.-C.; Chen, W.-C. The structures and properties of hydrogen silsesquioxane (HSQ) films produced by thermal curing. *J. Mater. Chem*. **2002**, *12*, 1138–1141.

127. Belot, V.; Corriu, R.; Leclercq, D.; Mutin, P. H.; Vioux, A. Thermal Reactivity of Hydrogenosilsesquioxane Gels. *Chem. Mater.* **1991**, *3*, 127–131.

128. Hessel, C. M.; Reid, D.; Panthani, M. G.; Rasch, M. R.; Goodfellow, B. W.; Wei, J. W.; Fujii, H.; Akhavan, V.; Korgel, B. A. Synthesis of Ligand-Stabilized Silicon Nanocrystals with Size-Dependent Photoluminescence Spanning Visible to Near-Infrared Wavelengths. *Chem. Mater.* **2012**, *24*, 393– 401.

129. Yang, Z.; Dobbie, A. R.; Cui, K.; Jonathan. A Convenient Method for Preparing Alkyl-Functionalized Silicon Nanocubes. *J. Am. Chem. Soc.* **2012**, *134*, 13958–13961.

130. Henderson, E. J.; Kelly, J. A.; Veinot, J. G. C. Influence of $HSiO_{1.5}$ Sol-Gel Polymer Structure and Composition on the Size and Luminescent Properties of Silicon Nanocrystals. *Chem. Mater*. **2009**, *21*, 5426–5434.

131. Henderson, E. J.; Veinot, J. G. C. From Phenylsiloxane Polymer Composition to Size-Controlled Silicon Carbide Nanocrystals. *J. Am. Chem. Soc*. **2009**, *131*, 809–815.

132. Dasog, M.; Rachinsky, C.; Veinot, J. G. C. From Si and C encapsulated SiO_2 to SiC: Exploring the influence of sol-gel polymer substitution on thermally induced nanocrystal formation. *J. Mater. Chem.* **2011**, *21*, 12422–12427.

133. Xin, Y.; Wakimoto, R.; Saitow, K. Synthesis of Size-controlled Luminescent Si Nanocrystals from $(HSiO_{1.5})_n$ Polymers. *Chem. Lett*. **2017**, *46*, 699−702.

134. Terada, S.; Xin, Y.; Saitow, K. Cost-Effective Synthesis of Silicon Quantum Dots. *Chem. Mater.* **2020**, *32*, 8382−8392.

135. Zhou, W. J.; Zheng, Y. X.; Zhang, C.; Ma, X. F.; Li, D. H.; Ma, L.; Hu, F.; Yang, S. D.; Yang, L.; Gao, M. Y.; Lu, M.; Zhang, R. J.; Wang, S. Y.; Chen, L. Y. Optical properties of high photoluminescence silicon nanocrystals embedded in SiO2 matrices obtained by annealing hydrogen silsesquioxane. *Opt. Mater.* **2018**, *84*, 874–878.

Chapter 2

1. Takagi, H.; Ogawa, H.; Yamazaki, Y.; Ishizaki, A.; Nakagiri, T. Quantum Size Effects on Photoluminescence in Ultrafine Si Particles, *Appl. Phys. Lett.* **1990**, *56*, 2379–2380.
2. Mangolini, L. Synthesis, properties, and applications of silicon nanocrystals. *J. Vac. Sci. Technol. B* **2013**, *31*, 020801.
3. Milliken, S.; Thiessen, A. N.; Cheong, I. T.; O'Connor, K. M.; Li, Z.; Hooper, R. W.; Robidillo, C. J. T.; Veinot, J. G. C. "Turning the dials": Controlling Synthesis, Structure, Composition, and Surface Chemistry to Tailor Silicon Nanoparticle Properties. *Nanoscale* **2021**, *13*, 16379–16404.
4. Fu, Y. H.; Kuznetsov, A. I.; Miroshnichenko, A. E.; Yu, Y. F.; Luk'yanchuk, B. Directional visible light scattering by silicon nanoparticles. *Nat. Commun.* **2013**, *4*, 1527.
5. Sugimoto, H.; Fujii, M. Colloidal Mie resonant silicon nanoparticles. *Nanotechnology* **2021**, *32*, 452001.
6. Jahani, S.; Jacob, Z. All-dielectric metamaterials. *Nat. Nanotechnol*. **2016**, *11*, 23–36.
7. De Marco, L. M.; Semlali, S.; Korgel, B. A; Barois, P.; Drisko, G. L.; Aymonier, C. Silicon-Based Dielectric Metamaterials: Focus on the Current Synthetic Challenges. *Angew. Chem. Int. Ed.* **2018**, *57*, 4478–4498.
8. Eslamisaray, M. A.; Wray, P. R.; Lee, Y.; Nelson, G. M.; Ilic, O.; Atwater, H. A.; Kortshagen, U. R. A Single-Step Bottom-up Approach for Synthesis of Highly Uniform Mie-Resonant Crystalline Semiconductor Particles at Visible Wavelengths. *Nano Lett.* **2023**, *23*, 1930–1937.
9. De Marco, L. M.; Jiang, T.; Fang, J.; Lacomme, S.; Zheng, Y.; Baron, A.;. Korgel, B. A.; Barois, P.; Drisko, G. L.; Aymonier, C. Broadband Forward Light Scattering by Architectural Design of Core–Shell Silicon Particles. *Adv. Funct. Mater.* **2021**, *31*, 2100915.
10. Sun, H.; Miyazaki, S.; Tamamitsu, H.; Saitow, K. One-Pot Facile Synthesis of a Concentrated Si Nanoparticle Solution. *Chem. Commun.* **2013**, *49*, 10302–10302.
11. Saitow, K.; Suemori, H.; Tamamitsu, H. Enhancement of Fluorescence Intensity by Silicon Particles and Its Size Effect. *Chem. Commun.* **2014**, *50*, 1137–1140.

12. Sakamoto, M.; Terada, S.; Mizutani, T.; Saitow, K. Large Field Enhancement of Nanocoral Structures on Porous Si Synthesized from Rice Husks. *ACS Appl. Mater. Interfaces* **2021**, *13*, 1105–1113.
13. Sugimoto, H.; Okazaki, T.; Fujii, M. Mie resonator color inks of monodispersed and perfectly spherical crystalline silicon nanoparticles. *Adv. Opt. Mater.* **2020**, *8*, 2000033.
14. Hessel, C. M.; Henderson, E. J.; Veinot J. G. C. Hydrogen Silsesquioxane: A Molecular Precursor for Nanocrystalline Si-SiO_2 Composites and Freestanding Hydride-Surface-Terminated Silicon Nanoparticles. *Chem. Mater.* **2006**, *18*, 6139–6146.
15. Milburn, L.; Robidillo, C. J.; Dalangin, R.; Shen, Y.; Veinot, J. G. C. A Complementary Silicon Quantum Dot-Enzyme Platform for the Selective Detection of Nitroaromatic Compounds: Explosives versus Nerve Agents. *ACS Appl. Nano Mater.* **2022**, *5*, 11984–11990.
16. Cheong, I. T.; Mock, J.; Kallergi, M.; Groß, E.; Meldrum, A.; Rieger, B.; Becherer, M.; Veinot, J. G. C. Colloidal Silicon Quantum Dot-Based Cavity Light-Emitting Diodes with Narrowed and Tunable Electroluminescence. *Adv. Opt. Mater.* **2023**, *11*, 2201834.
17. Thiessen, A. N.; Zhang, L.; Oliynyk, A. O.; Yu, H.; O'Connor, K. M.; Meldrum, A.; Veinot, J. G. C. A Tale of Seemingly "Identical" Silicon Quantum Dot Families: Structural Insight into Silicon Quantum Dot Photoluminescence. *Chem. Mater.* **2020**, *32*, 6838–6846.
18. Milliken, S.; Cheong, I. T.; Cui, K.; Veinot, J. G. C. Boron Doping of Silicon Quantum Dots via Hydrogen Silsesquioxane-Capped Diffusion for Photovoltaics and Medical Imaging. *ACS Appl. Nano Mater.* **2022**, *5*, 15785–15796.
19. Hessel, C. M.; Reid, D.; Panthani, M. G.; Rasch, M. R.; Goodfellow, B. W.; Wei, J.; Fujii H.; Akhavan, V.; Korgel, B. A. Synthesis of Ligand-Stabilized Silicon Nanocrystals with Size-Dependent Photoluminescence Spanning Visible to Near-Infrared Wavelengths. *Chem. Mater.* **2012**, *24*, 393–401.
20. Thiessen, A. N.; Ha, M.; Hooper, R. W.; Yu, H.; Oliynyk, A. O.; Veinot, J. G. C.; Michaelis, V. K. Silicon Nanoparticles: Are They Crystalline from the Core to the Surface? *Chem. Mater.* **2019**, *31*, 678–688.
21. Hom, T.; Kiszenick, W.; Post, B. Accurate lattice constants from multiple reflection mesurements II. Lattice constants of germanium, silicon and diamond. *J. Appl. Crystallogr.* **1975**, *8*, 457–458.

22. Downs, R. T.; Palmer, D. C. The pressure behavior of alpha cristobalite. *Am. Mineral*. **1994**, *79*, 9–14.
23. Pan, Z. W., Dai, Z. R.; Xu, L..; Lee, S. T.; Wang, Z. L. Temperature-Controlled Growth of Silicon-Based Nanostructures by Thermal Evaporation of SiO Powders. *J. Phys. Chem. B* **2001**, *105*, 2507–2514.
24. Zhou, J.; Huang, J.; Chen, H.; Samanta, A.; Linnros, J.; Yang, Z.; Sychugov, I. Low-Cost Synthesis of Silicon Quantum Dots with Near-Unity Internal Quantum Efficiency. *J. Phys. Chem. Lett.* **2021**, *12*, 8909–8916.
25. Terada, S.; Xin, Y.; Saitow, K. I. Cost-Effective Synthesis of Silicon Quantum Dots. *Chem. Mater*. **2020**, *32*, 8382–8392.
26. Mamiyaa, M.; Takeia, H.; Kikuchib, M.; Uyedaa, C. Preparation of fine silicon particles from amorphous silicon monoxide by the disproportionation reaction. *J. Cryst. Growth* **2001**, *229*, 457–461.
27. Sun, W.; Qian, C.; Cui, X. S.; Wang, L.; Wei, M.; Casillas, G.; Helmyb, A. S.; Ozin, G. A. Silicon monoxide – a convenient precursor for large scale synthesis of near infrared emitting monodisperse silicon nanocrystals. *Nanoscale* **2016**, *8*, 3678–3684.
28. Valenta, J.; Greben, M.; Dyakov, S. A.; Gippius, N. A.; Hiller, D.; Gutsch, S.; Zacharias, M. Nearly perfect near-infrared luminescence efficiency of Si nanocrystals: A comprehensive quantum yield study employing the Purcell effect. *Sci. Rep*. **2019**, *9*, 11214.
29. Chlouba, T.; Trojánek, F.; Kopecký Jr., V.; López-Vidrier, J.; Hernandéz, S.; Hiller, D.; Gutsch, S.; Zacharias, M.; Malý, P. Pathways of carrier recombination in Si/SiO_2 nanocrystal superlattices. *J. Appl. Phys.* **2019**, *126*, 163101.
30. Hiller, D.; König, D.; Nagel, P.; Merz, M.; Schuppler, S.; Smith, S. C. On the Location of Boron in SiO_2-Embedded Si Nanocrystals—An X-ray Absorption Spectroscopy and Density Functional Theory Study. *Phys. Status Solidi B* **2021**, *258*, 2000623.
31. Guha, S.; Pace, M. D.; Dunn, D. N.; Singer, I. L. Visible light emission from Si nanocrystals grown by ion implantation and subsequent annealing. *Appl. Phys. Lett*. **1997**, *70*, 1207–1209.
32. Zhang, R.; Yuan, Y.; Zhang, J.; Zuo, W.; Zhou, Y.; Gao, X.; Wang, W.; Qin, Z.; Zhang, Q.; Chen, F.; Du, Z.; Li, J. A light-influenced memristor based on Si nanocrystals by ion implantation technique. *J. Mater. Sci.* **2021**, *56*, 2323–2331.

33. Beyer, V.; von Borany, J.; Heinig, K. H. Dissociation of Si^+ ion implanted and as-grown thin SiO_2 layers during annealing in ultra-pure neutral ambient by emanation of SiO. *J. Appl. Phys.* **2007**, *101*, 053516.
34. Wang, N.; Tang, Y.H.; Zhang, Y.F.; Lee, C.S.; Bello, I.; Lee, S.T. Si Nanowires grown from silicon oxide. *Chem. Phys. Lett.* **1999**, *299*, 237–242.
35. Shi, W. S.; Peng, H. Y..; Zheng, Y. F.; Wang, N.; Shang, N. G.; Pan, Z. W.; Lee, C. S.; Lee, S. T. Synthesis of large areas of highly oriented, very long silicon nanowires. *Adv. Mater*. **2000**, *12*, 1343–1345.
36. Zhang, B. C.; Wang, H.; He, L.; Zheng, C. J.; Jie, J. S.; Lifshitz, Y.; Lee, S. T.; Zhang, X. H. Centimeter-Long Single-Crystalline Si Nanowires. *Nano Lett*. **2017**, *17*, 7323–7329.
37. Srivastava, S.K.; Singh, P.K.; Singh, V.N.; Sood, K.N.; Haranath, D.; Kumar, V. Large-scale synthesis, characterization and photoluminescence properties of amorphous silica nanowires by thermal evaporation of silicon monoxide. *Physica E* **2009**, *41*, 1545–1549.
38. Winkler, C. Ueber die Reduction von Sauerstoffverbindungen durch Magnesium. *Ber*. **1890**, *23*, 2642–2668.
39. Potter, H. N. Silicon monoxide. *Trans. Am. Electrochem. Soc*. **1908**, *12*, 191–214.
40. Roeber, E. F.; Parmelee, H. C. *Electrochemical and Metallurgical Industry*, Electrochemical Publishing Company, London, 1907.
41. Kubascheeski, O.; Chart, T. G. Silicon monoxide pressures due to the reaction between solid silicon and silica. *J. Chem. Thermodyn.* **1974**, *6,* 467–476.
42. Schnurre, S. M.; Grobner, J.; Schmid-Fetzer, R. Thermodynamics and phase stability in the Si–O system. *J. Non-Cryst. Solids* **2004**, *336*, 1–25.
43. Benyon, J. Silicon Monoxide: Fact or Fiction. *Vacuum* **1970**, *20*, 293–294.
44. Yasaitis, J. A.; Kaplow, R. Structure of amorphous silicon monoxide. *J. Appl. Phys.* **1972**, *43*, 995–1000.
45. Hohl, A.; Wieder, T.; van Aken, P.A.; Weirich, T.E.; Denninger, G.; Vidal, M.; Oswald, S.; Deneke, C.; Mayer, J.; Fuess, H. An interface clusters mixture model for the structure of amorphous silicon monoxide (SiO). *J. Non-Cryst. Solids* **2003**, *320*, 255–280.
46. Schulmeister, K.; Mader, W. TEM investigation on the structure of amorphous silicon monoxide. *J. Non-Cryst. Solids* **2003**, *320*, 143–150.

47. Hirata, A.; Kohara, S.; Asada, T.; Arao, M.; Yogi, C.; Imai, H.; Tan, Y.; Fujita, T.; Chen, M. Atomic-scale disproportionation in amorphous silicon monoxide. *Nat. Commun*. **2016**, *7*, 11591.

48. Li, F.; Huang, Y.; Wang, S.; Zhang, S. Critical review: Growth mechanisms of the self-assembling of silicon wires. *J. Vac. Sci. Technol. A* **2020**, *38*, 010802.

49. Li, F. J.; Zhang, S.; Lee, J. W. Rethinking on the silicon nanowire growth mechanism during thermal evaporation of Si-containing powders. *Thin Solid Films* **2014**, *558*, 75–85.

50. Vogli, E.; Mukerji, J.; Hoffman, C.; Kladny, R.; Sieber, H.; Greil, P. Conversion of oak to cellular silicon carbide ceramic by gas-phase reaction with silicon monoxide. *J. Am. Ceram. Soc*. **2001**, *84*, 1236–40.

51. Aarnæs, T.S., Ringdalen, E. & Tangstad, M. Silicon carbide formation from methane and silicon monoxide. *Sci. Rep.* **2020,** *10*, 21831.

52. Chen, X.; Zhang, D.; Zhang, X.; Liu, Y.; Li, X.; Xiang, G. Synthesis and growth mechanism of Mn-doped nanodot embedded silica nanowires. *Physica B* **2019**, *571*, 10–17.

53. AlKaabi, K.; Prasad, D. L. V. K.; Kroll, P. ; Ashcroft, N. W.; Hoffmann, R. Silicon Monoxide at 1 atm and Elevated Pressures: Crystalline or Amorphous? *J. Am. Chem. Soc.* **2014**, *136*, 3410–3423.

54. Neizvestny, I. G.; Shwartz, N. L. Monte Carlo Simulation of Semiconductor Nanostructure Growth. In *Advances in Semiconductor Nanostructures*. Latyshev, A. V.; Dvurechenskii, A. V.; Aseev, A. L., Eds.; Elsevier, 2017, ch. 14, pp. 345–364.

55. Ferguson, F. T.; Nuth, J. A. Vapor Pressure and Evaporation Coefficient of Silicon Monoxide over a Mixture of Silicon and Silica. *J. Chem. Eng. Data* **2012**, *57*, 721–728.

56. Broggi, A.; Tangstad, M.; Ringdalen, E. Characterization of a Si-SiO_2 Mixture Generated from SiO(g) and CO(g). *Metall. Mater. Trans. B* **2019**, *50*, 2667–2680.

57. Porter, R. F.; Chupka, W. A.; Ingiiram, M. G. Mass Spectrometric Study of Gaseous Species in the Si-SiO_2 System. *J. Chem. Phys*. **1955**, *23*, 216–217.

58. Chase, M. W. *NIST-JANAF Themochemical Tables,* 4th ed.; *J. Phys. Chem. Ref. Data*, 1998.

59. Nagamori, M.; Boivin, J. A.; Claveau, A. Gibbs free energies of formation of amorphous Si_2O_3, SiO and Si_2O. *J. Non-Cryst. Solids* **1995**, *189*, 270–276.

60. Sarikov, A.; Zacharias, M. Gibbs free energy and equilibrium states in the Si/Si oxide systems. *J. Phys. Condens. Matter* **2012**, *24*, 385403–385403.

61. Sarikova, A.; Zhigunov, D. Thermodynamic mechanism of the intermixing of multilayered structures in the SiO_X/SiO_2 superlattices with nanometer thick layers. *Mater. Today Commun.* **2017**, *13*, 163–169.
62. Pizzini, S. Physical Chemistry of Semiconductor Materials and Processes, Wiley, United Kingdom, 2015.
63. Yang, C. C.; Chen, W. C. The structures and properties of hydrogen silsesquioxane (HSQ) films produced by thermal curing. *J. Mater. Chem.* **2002**, *12*, 1138–1141.
64. O'Connor, K. M.; Rubletz, A.; Trach, J.; Butler, C.; Veinot, J. G. C. Understanding Silicon Monoxide Gas Evolution from Mixed Silicon and Silica Powders. *Nanoscale Horiz.* **2023**, *8,* 892–899.
65. Frye, C. L.; Collins, W. T. The Oligomeric Silsesquioxanes, $(HSiO_{3/2})_n$. *J. Am. Chem. Soc.* **1970**, *92*, 5586–5588.
66. Murphy, C. J.; Buriak, J. M. Best Practices for the Reporting of Colloidal Inorganic Nanomaterials. *Chem. Mater.* **2015**, *27*, 4911–4913.

Chapter 3

1. Baldwin, R. K.; Pettigrew, K. A.; Ratai, E.; Augustine, M. P.; Kauzlarich, S. M. Solution Reduction Synthesis of Surface Stabilized Silicon Nanoparticles. *Chem. Commun.* **2002**, *17*, 1822–1823.
2. Adachi, M.; Sugimoto, H.; Nishimura, Y.; Morita, K.; Ogino, C.; Fujii, M. Fluorophore-Decorated Mie Resonant Silicon Nanosphere for Scattering/Fluorescence Dual-Mode Imaging. *Small* **2023**, *19*, 2207318.
3. Slootman, F.; Parent, J.-C. Homogeneous Gas-Phase Nucleation in Silane Pyrolysis. *J. Aerosol Sci.* **1994**, *25*, 15–21.
4. Eslamisaray, M. A.; Wray, P.; Lee, Y.; Nelson, G. M.; Ilic, O.; Atwater, H. A.; Kortshagen, U. R. A Single-Step Bottom-up Approach for Synthesis of Highly Uniform Mie-Resonant Crystalline Semiconductor Particles at Visible Wavelengths. *Nano Lett.* **2023**, *23*, 1930–1937.

5. McVey, B. F. P.; Butkus, J.; Halpert, J. E.; Hodgkiss, J. M.; Tilley, R. D. Solution Synthesis and Optical Properties of Transition-Metal-Doped Silicon Nanocrystals. *J. Phys. Chem. Lett.* **2015**, *6*, 1573–1576.
6. Zhang, P.; Duan, J.; Chen, G.; Li, J.; Wang, W. Production of Polycrystalline Silicon from Silane Pyrolysis: A Review of Fines Formation. *Sol. Energy* **2018**, *175*, 44–53.
7. Milliken, S.; Thiessen, A. N.; Cheong, I. T.; O'Connor, K. M.; Li, Z.; Hooper, R. W.; Robidillo, C. J. T.; Veinot, J. G. C. "Turning the Dials": Controlling Synthesis, Structure, Composition, and Surface Chemistry to Tailor Silicon Nanoparticle Properties. *Nanoscale* **2021**, *13*, 16379–16404.
8. Rodríguez Núñez, J. R. Commentary: Silicon Nanocrystals and Their Role in Photonics. *J. Nanophotonics* **2012**, *6*, 060302.
9. Sun, W.; Qian, C.; Cui, X. S.; Wang, L.; Wei, M.; Casillas, G.; Helmy, A. S.; Ozin, G. A. Silicon Monoxide – a Convenient Precursor for Large Scale Synthesis of near Infrared Emitting Monodisperse Silicon Nanocrystals. *Nanoscale* **2016**, *8*, 3678–3684.
10. Hessel, C. M.; Henderson, E.; Veinot, J. G. C.. Hydrogen Silsesquioxane: A Molecular Precursor for Nanocrystalline Si−SiO_2 Composites and Freestanding Hydride-Surface-Terminated Silicon Nanoparticles. *Chem. Mater.* **2006**, *18*, 6139–6146.
11. Hessel, C. M.; Henderson, E. J.; Veinot, J. G. C. An Investigation of the Formation and Growth of Oxide-Embedded Silicon Nanocrystals in Hydrogen Silsesquioxane-Derived Nanocomposites. *J. Phys. Chem. C* **2007**, *111*, 6956–6961.
12. Meldrum, A.; Hryciw, A. C.; A. Nicole MacDonald; Blois, C.; Marsh, K. L.; Wang, J.; Li, Q. Photoluminescence in the Silicon-Oxygen System. *J. Vac. Sci. Technol., A* **2006**, *24*, 713–717.
13. Kelly, J. A.; Henderson, E. J.; Clark, R. J.; Hessel, C. M.; Cavell, R. G.; Veinot, J. G. C. X-Ray Absorption Spectroscopy of Functionalized Silicon Nanocrystals. *J. Phys. Chem. C* **2010**, *114*, 22519–22525.
14. Rodríguez Núñez, J. R.; Kelly, J. A.; Henderson, E. J.; Veinot, J. G. C. Wavelength-Controlled Etching of Silicon Nanocrystals. *Chem. Mater.* **2012**, *24*, 346–352.
15. Terada, S.; Xin, Y.; Saitow, K. Cost-Effective Synthesis of Silicon Quantum Dots. *Chem. Mater.* **2020**, *32*, 8382–8392.

16. Zhang, M.; Poumirol, J.-M.; Chery, N.; Rinnert, H.; Giba, A. E.; Demoulin, R.; Talbot, E.; Cristiano, F.; Hungria, T.; Paillard, V.; Gourbilleau, F.; Bonafos, C. Hyperdoped Si Nanocrystals Embedded in Silica for Infrared Plasmonics. *Nanoscale* **2023**, *15*, 7438–7449.
17. Neufeld, E.; Wang, S.; Apetz, R.; Buchal, C.; Carius, R.; White, C. W.; Thomas, D. K. Effect of Annealing and H_2 Passivation on the Photoluminescence of Si Nanocrystals in SiO_2. *Thin Solid Films* **1997**, *294*, 238–241.
18. Withrow, S. P.; White, C. W.; Meldrum, A.; Budai, J. D.; Hembree, D. M.; Barbour, J. C. Effects of Hydrogen in the Annealing Environment on Photoluminescence from Si Nanoparticles in SiO2. *J. Appl. Phys.* **1999**, *86*, 396–401.
19. Wilkinson, A. R.; Elliman, R. G. The Effect of Annealing Environment on the Luminescence of Silicon Nanocrystals in Silica. *J. Appl. Phys* **2004**, *96*, 4018–4020.
20. S. Cheylan; Elliman, R. G. Effect of Hydrogen on the Photoluminescence of Si Nanocrystals Embedded in a SiO2 Matrix. *Appl. Phys. Lett.* **2001**, *78*, 1225–1227.
21. Ikeda, M.; Nakagawa, M.; Mitsusue, R.; Kondo, S.; N. Imanishi. Hydrogen Behavior in SiO2 with High Density of Defects and Locally Concentrated Silicon. *J. Appl. Phys.* **2004**, *95*, 4655–4661.
22. Godefroo, S.; Hayne, M.; Mihaela Jivanescu; Stesmans, A.; Zacharias, M.; Lebedev, O. I.; van Tendeloo, G.; Moshchalkov, V. Classification and Control of the Origin of Photoluminescence from Si Nanocrystals. *Nat. Nanotechnol.* **2008**, *3*, 174–178.
23. Borrero-González, L. J.; Nunes, L. A.; Marcello; Wójcik, J.; Mascher, P.; Pusep, Y. A.; Comedi, D.; Eduardo, F. The Role of Quantum Confinement and Crystalline Structure on Excitonic Lifetimes in Silicon Nanoclusters. *J. Appl. Phys.* **2010**, *108*, 013105.
24. Li, Y.; Liang, P.; Hu, Z.; Guo, S.; You, Q.; Sun, J.; Xu, N.; Wu, J. Enhancement and Stability of Photoluminescence from Si Nanocrystals Embedded in a SiO2 Matrix by H2-Passivation. *Appl. Surf. Sci.* **2014**, *300*, 178–183.
25. Thiessen, A.; Zhang, L.; Oliynyk, A. O.; Yu, H.; O'Connor, K.; Meldrum, A.; Veinot, J. G. C. A Tale of Seemingly "Identical" Silicon Quantum Dot Families: Structural Insight into Silicon Quantum Dot Photoluminescence. *Chem. Mater.* **2020**, *32*, 6838–6846.

26. Yu, Y.; Fan, G.; Fermi, A.; Mazzaro, R.; Morandi, V.; Ceroni, P.; Detlef-M. Smilgies; Korgel, B. A. Size-Dependent Photoluminescence Efficiency of Silicon Nanocrystal Quantum Dots. *J. Phys. Chem. C* **2017**, *121*, 23240–23248.
27. Aghajamali, M.; Xie, H.; Javadi, M.; W.; Kalisvaart, P.; Buriak, J. M.; Veinot, J. G. C. Size and Surface Effects of Silicon Nanocrystals in Graphene Aerogel Composite Anodes for Lithium Ion Batteries. *Chem. Mater.* **2018**, *30*, 7782–7792.
28. Thiessen, A. N.; Ha, M.; Hooper, R. W.; Yu, H.; Oliynyk, A. O.; Veinot, J. G. C.; Michaelis, V. K. Silicon Nanoparticles: Are They Crystalline from the Core to the Surface? *Chem. Mater.* **2019**, *31*, 678–688.
29. Tsai, H.-Y.; Robidillo, C. J. T.; Matharu, G. K.; O'Connor, K.; Cheong, I. T.; Ni, C.; Veinot, J. G. C.; Algar, W. R. Spectrotemporal Characterization of Photoluminescent Silicon Nanocrystals and Their Energy Transfer to Dyes. *Nanoscale* **2023**, *15*, 12492–12505.
30. Hessel, C. M.; Reid, D. K.; Panthani, M. G.; Rasch, M.; Goodfellow, B. W.; Wei, J.; Fujii, H.; Akhavan, V. A.; Korgel, B. A. Synthesis of Ligand-Stabilized Silicon Nanocrystals with Size-Dependent Photoluminescence Spanning Visible to Near-Infrared Wavelengths. *Chem. Mater.* **2011**, *24*, 393–401.
31. O'Connor, K.; Rubletz, A.; Ni, C.; He, Y.; Butler, C.; Veinot, J. G. C. High-Temperature Anomaly in the Synthesis of Large (D > 100 nm) Silicon Nanoparticles from Hydrogen Silsesquioxane. *Chem. Mater.* **2023**, *35*, 7967–7973.
32. Hom, T.; Kiszenik, W.; Post, B. Accurate lattice constants from multiple reflection mesurements II. Lattice constants of germanium, silicon and diamond. *J. Appl. Crystallogr*. **1975**, *8*, 457–458.
33. Downs, R. T.; Palmer, D. C. The pressure behavior of alpha cristobalite. *Am. Mineral*. **1994**, *79*, 9–14.
34. Heya, A.; Masuda, A.; Matsumura, H. Mechanism of Low-Temperature Crystallization of Amorphous Silicon by Atomic Hydrogen Anneal. *J. Non-Cryst. Solids* **2000**, *266–269*, 619–623.
35. Hanrahan, M. P.; Fought, E. L.; Windus, T. L.; Wheeler, L. M.; Anderson, N. C.; Neale, N. R.; Rossini, A. J. Characterization of Silicon Nanocrystal Surfaces by Multidimensional Solid-State NMR Spectroscopy. *Chem. Mater.* **2017**, *29*, 10339–10351.

36. Dorn, R. W.; Ryan, B. J.; Lamahewage, S. N. S.; Dodson, M. V.; Essner, J. B.; Biswas, R.; Panthani, M. G.; Rossini, A. J. Chlorination of Hydrogenated Silicon Nanosheets Revealed by Solid-State Nuclear Magnetic Resonance Spectroscopy. *Chem. Mater.* **2023**, *35*, 539–548.
37. Ha, M.; Thiessen, A. N.; Sergeyev, I. V.; Veinot, J. G. C.; Michaelis, V. K. Endogenous Dynamic Nuclear Polarization NMR of Hydride-Terminated Silicon Nanoparticles. *Solid State Nucl. Magn. Reson.* **2019**, *100*, 77–84.
38. Cibaka-Ndaya, C.; O'Connor, K.; Idowu, E. O.; Parker, M. A.; Lebraud, É.; Lacomme, S.; Montero, D.; Camacho, P. S.; Veinot, J. G. C.; Roiban, I. L.; Drisko, G. L. Understanding the Formation Mechanisms of Silicon Particles from the Thermal Disproportionation of Hydrogen Silsesquioxane. *Chem Mater.* **2023**, *35*, 8551–8560.
39. Deer, W. A. *Rock-Forming Minerals, Vol. 4B: Framework Silicates - Silica Minerals, Feldspathoids and Zeolites*, 2nd edition.; Howie, R. A., Wise, W. S., Zussman, J., Eds.; Geological Society of London: London, 2006.
40. Yang, Z.; Dobbie, A. R.; Cui, K.; Veinot, J. G. C. A Convenient Method for Preparing Alkyl-Functionalized Silicon Nanocubes. *J. Am. Chem. Soc.* **2012**, *134*, 13958–13961.
41. Yang, Z.; Dobbie, A. R.; Veinot, J. G. C. Shape Evolution of Faceted Silicon Nanocrystals upon Thermal Annealing in an Oxide Matrix. *MRS Online Proc. Lib.* **2013**, *1536*, 207–212.
42. Sinelnikov, R.; Dasog, M.; Beamish, J.; Meldrum, A.; Veinot, J. G. C. Revisiting an Ongoing Debate: What Role Do Surface Groups Play in Silicon Nanocrystal Photoluminescence? *ACS Photonics* **2017**, *4*, 1920–1929.
43. Cheong, I. T.; Mock, J.; Kallergi, M.; Groß, E.; Meldrum, A.; Rieger, B.; Becherer, M.; Veinot, J. G. C. Colloidal Silicon Quantum Dot-Based Cavity Light-Emitting Diodes with Narrowed and Tunable Electroluminescence. *Adv. Opt. Mater.* **2023**, *11*, 2201834.
44. Mastronardi, M. L.; Chen, K. K.; Liao, K.; Casillas, G.; Ozin, G. A. Size-Dependent Chemical Reactivity of Silicon Nanocrystals with Water and Oxygen. *J. Phys. Chem. C* **2014**, *119*, 826–834.
45. Pereira, R. N.; Rowe, D. J.; Anthony, R. J.; Kortshagen, U. Oxidation of Freestanding Silicon Nanocrystals Probed with Electron Spin Resonance of Interfacial Dangling Bonds. *Phys. Rev. B* **2011**, *83*, 155327.

46. Rinck, J.; Schray, D.; Kübel, C.; Powell, A. K.; Ozin, G. A. Silicon Nanocrystals: Size-Dependent Oxidation of Monodisperse Silicon Nanocrystals with Allylphenylsulfide Surfaces. *Small* **2015**, *11*, 262–262.
47. Frye, C. L.; Collins, W. T. Oligomeric Silsesquioxanes, $(HSiO_{3/2})n$. *J. Am. Chem. Soc.* **1970**, *92*, 5586–5588.
48. Wojdyr, M. Fityk: A General-Purpose Peak Fitting Program. *J. Appl. Crystallogr.* **2010**, *43*, 1126–1128.
49. Hayashi, S.; Hayamizu, K. Chemical Shift Standards in High-Resolution Solid-State NMR ^{13}C, ^{29}Si, and ^{1}H Nuclei. *Bull. Chem. Soc. Jpn.* **1991**, *64*, 685– 687.
50. Driel, A. F.; Nikolaev, I. S.; Vergeer, P.; Lodahl, P.; Vanmaekelbergh, D.; Vos, W. L. Statistical Analysis of Time-Resolved Emission from Ensembles of Semiconductor Quantum Dots: Interpretation of Exponential Decay Models. *Phys. Rev. B* **2007**, *75*, 035329.
51. Murphy, C. J.; Buriak, J. M. Best Practices for the Reporting of Colloidal Inorganic Nanomaterials. *Chem. Mater.* **2015**, *27*, 4911–4913.

Chapter 4

1. Cibaka-Ndaya, C.; O'Connor, K.; Idowu, E. O.; Parker, M. A.; Lebraud, É.; Lacomme, S.; Montero, D.; Sanz Camacho, P.; Veinot, J. G. C.; Roiban, I.-L.; Drisko, G. L. Understanding the Formation Mechanisms of Silicon Particles from the Thermal Disproportionation of Hydrogen Silsesquioxane. *Chem. Mater.* **2023**, *25*, 8551–8560.
2. Khanna, V. K. Nanomaterials and Their Properties. In *Integrated Nanoelectronics*; Springer: New Delhi, 2016; pp. 25–41.
3. Joshi, K. U.; Kabiraj, D.; Narsale, A. M.; Avasthi, D. K.; Warang, T. N.; Kothari, D. C. Embedded SiGe Nanoparticles Formed by Atom Beam Co-Sputtering of Si, Ge, SiO_2. *Surf. Coat. Technol.* **2009**, *203*, 2482–2485.
4. Prilepskii V. I. Distortions of the lattices of germanium, silicon, and their solid solutions within the interval from 88 to 500 K. *Inorg. Mater*. **1965**, *1*, 1163–1167.
5. Atkins, P.; Overton, T.; Rourke, J.; Weller, M.; Armstrong, F. *Inorganic Chemistry*, 4th ed.; Salvador, P., Hagerman, M., Spiro, T., Stiefel, E., Eds.; W. H. Freeman and Company: New York, 2006.

6. Pauleau, Y.; Remy, J. C. Kinetics of the Formation and Sublimation of Germanium Monoxide. *J. Less-Common Met.* **1975**, *42*, 199–208.
7. Muthuswamy, E.; Iskandar, A. S.; Amador, M. M.; Kauzlarich, S. M. Facile Synthesis of Germanium Nanoparticles with Size Control: Microwave versus Conventional Heating. *Chem. Mater.* **2013**, *25*, 1416–1422.
8. Warner, J. H.; Tilley, R. D. Synthesis of Water-Soluble Photoluminescent Germanium Nanocrystals. *Nanotechnology* **2006**, *17*, 3745–3749.
9. Chiu, H. W.; Kauzlarich, S. M. Investigation of Reaction Conditions for Optimal Germanium Nanoparticle Production by a Simple Reduction Route. *Chem. Mater*. **2006**, *18*, 1023–1028.
10. Lu, X.; Korgel, B. A.; Johnston, K. P. High Yield of Germanium Nanocrystals Synthesized from Germanium Diiodide in Solution. *Chem. Mater*. **2005**, *17*, 6479–6485.
11. Gorla, C. R.; Liang, S.; Tompa, G. S.; Mayo, W. E.; Lu, Y. Silicon and Germanium Nanoparticle Formation in an Inductively Coupled Plasma Reactor. *J. Vac. Sci. Technol., A* **1997**, *15*, 860–864.
12. Kim, S.; Walker, B.; Park, S. Y.; Choi, H.; Ko, S.-J.; Jeong, J.; Yun, M. H.; Lee, J. C.; Kim, D. S.; Kim, J. Y. Size Tailoring of Aqueous Germanium Nanoparticle Dispersions. *Nanoscale* **2014**, *6*, 10156–10160.
13. Javadi, M.; Picard, D.; Sinelnikov, R.; Narreto, M. A.; Hegmann, F. A.; Veinot, J. G. C. Synthesis and Surface Functionalization of Hydride-Terminated Ge Nanocrystals Obtained from the Thermal Treatment of $Ge(OH)_2$. *Langmuir* **2017**, *33*, 8757–8765.
14. Sun, W.; Zhong, G.; Kübel, C.; Jelle, A. A.; Qian, C.; Wang, L.; Ebrahimi, M.; Reyes, L. M.; Helmy, A. S.; Ozin, G. A. Size-Tunable Photothermal Germanium Nanocrystals. *Angew. Chem. Int. Ed.* **2017**, *56*, 6329–6334.
15. Yang, D. J.; Jolly, W. L.; O'Keefe, A. Conversion of Hydrous Germanium(II) Oxide to Germynyl Sesquioxide, $(HGe)_2O_3$. *Inorg. Chem.* **1977**, *16*, 2980–2982.
16. Wang, Y.; Ramesh, U.; Charles; Ryan, B. J.; Nelson, R. D.; Alebri, A. M.; Hamdeh, U. H.; Hadi, A.; Smith, E. A.; Panthani, M. G. Synthesis of Germanium Nanocrystals from Solid-State Disproportionation of a Chloride-Derived Germania Glass. *Chem. Commun.* **2019**, *55*, 6102–6105.